



Contents lists available at SciVerse ScienceDirect

# Progress in Materials Science

journal homepage: [www.elsevier.com/locate/pmatsci](http://www.elsevier.com/locate/pmatsci)



## Zero-dimensional, one-dimensional, two-dimensional and three-dimensional nanostructured materials for advanced electrochemical energy devices

Jitendra N. Tiwari <sup>a,\*</sup>, Rajanish N. Tiwari <sup>b</sup>, Kwang S. Kim <sup>a</sup>

<sup>a</sup> Center for Superfunctional Materials, Dept. of Chemistry, Pohang University of Science and Technology, San 31, Hyojadong, Namgu, Pohang 790-784, Republic of Korea

<sup>b</sup> Surface Science Laboratory, Toyota Technological Institute, 2-12-1 Hisakata Tempaku, Nagoya 468-8511, Japan

### ARTICLE INFO

#### Article history:

Received 15 April 2011

Accepted 14 August 2011

Available online 24 August 2011

### ABSTRACT

One of the biggest challenges of 21st century is to develop powerful electrochemical energy devices (EEDs). The EEDs such as fuel cells, supercapacitors, and Li-ion batteries are among the most promising candidates in terms of power-densities and energy-densities. The nanostructured materials (NSMs) have drawn intense attention to develop highly efficient EEDs because of their high surface area, novel size effects, significantly enhanced kinetics, and so on. In this review article, we briefly introduce general synthesis, fabrication and their classification as zero-dimensional (0D), one dimensional (1D), two-dimensional (2D) and three-dimensional (3D) NSMs. Subsequently, we focus an attention on recent progress in advanced NSMs as building blocks for EEDs (such as fuel cells, supercapacitors, and Li-ion batteries) based on investigations at the 0D, 1D, 2D and 3D NSMs.

© 2011 Elsevier Ltd. All rights reserved.

### Contents

1. Introduction . . . . .	726
1.1. Overview . . . . .	726
1.2. The scope of this review . . . . .	726
2. Classification of nanostructured materials (NSMs) . . . . .	726
2.1. 0D NSMs . . . . .	727
2.2. 1D NSMs . . . . .	727

\* Corresponding author. Tel.: +82 54 279 2110; fax: +82 54 279 8137.

E-mail address: [jnt\\_tiw123@yahoo.co.in](mailto:jnt_tiw123@yahoo.co.in) (J.N. Tiwari).

2.3.	2D NSMs . . . . .	729
2.4.	3D NSMs . . . . .	729
3.	Synthesis of NSMs . . . . .	730
3.1.	Physical methods. . . . .	730
3.1.1.	Evaporation technique . . . . .	730
3.1.2.	Sputtering technique . . . . .	731
3.1.3.	Lithography processes . . . . .	731
3.1.4.	Hot and cold plasma. . . . .	731
3.1.5.	Spray pyrolysis . . . . .	732
3.1.6.	Inert gas phase condensation technique. . . . .	733
3.1.7.	Pulsed laser ablation . . . . .	733
3.1.8.	Sonochemical reduction . . . . .	734
3.2.	Chemical methods. . . . .	734
3.2.1.	Lyotropic liquid crystal templates. . . . .	735
3.2.2.	Electrochemical deposition . . . . .	735
3.2.3.	Electroless deposition. . . . .	736
3.2.4.	Hydrothermal and solvothermal techniques. . . . .	736
3.2.5.	Sol-gel technique . . . . .	736
3.2.6.	Chemical vapor deposition. . . . .	737
3.2.7.	Laser chemical vapor deposition technique . . . . .	738
3.2.8.	Laser pyrolysis . . . . .	739
4.	Synthesis of 0D, 1D, 2D and 3D NSMs . . . . .	740
4.1.	Synthesis of 0D NSMs. . . . .	740
4.1.1.	Synthesis of 0D NSMs by physical processes . . . . .	740
4.1.2.	Synthesis of 0D NSMs by chemical processes. . . . .	741
4.2.	Synthesis of 1D NSMs. . . . .	743
4.2.1.	Synthesis of 1D NSMs by physical processes . . . . .	743
4.2.2.	Synthesis of 1D NSMs by chemical processes. . . . .	749
4.3.	Synthesis of 2D NSMs. . . . .	756
4.3.1.	Synthesis of 2D NSMs by physical processes . . . . .	756
4.3.2.	Synthesis of 2D NSMs by chemical processes. . . . .	763
4.4.	Synthesis of 3D NSMs. . . . .	770
4.4.1.	Synthesis of 3D NSMs by physical processes . . . . .	770
4.4.2.	Synthesis of 3D NSMs by chemical processes. . . . .	777
5.	Applications of 0D, 1D, 2D and 3D NSMs. . . . .	782
5.1.	Fuel cells . . . . .	782
5.1.1.	Introduction . . . . .	782
5.1.2.	0D NSMs . . . . .	783
5.1.3.	1D NSMs . . . . .	783
5.1.4.	2D NSMs . . . . .	785
5.1.5.	3D NSMs . . . . .	786
5.2.	Supercapacitors . . . . .	787
5.2.1.	Introduction . . . . .	787
5.2.2.	0D and 1D NSMs. . . . .	788
5.2.3.	2D NSMs . . . . .	789
5.2.4.	3D NSMs . . . . .	791
5.3.	Li-ion batteries . . . . .	791
5.3.1.	Introduction . . . . .	791
5.3.2.	0D and 1D NSMs. . . . .	792
5.3.3.	2D NSMs . . . . .	793
5.3.4.	3D NSMs . . . . .	794
6.	Conclusions and future outlook. . . . .	796
	Acknowledgments . . . . .	797
	References . . . . .	797

---

## 1. Introduction

### 1.1. Overview

One of the most important applications of electrochemical energy devices (EEDs) is conversion and storage of energy. It remains a challenge for the EEDs in the 21st century to achieve high power density and long-term cycling life. In response to the needs of modern society and emerging ecological concerns, it is highly desirable to find new, low-cost and environmentally friendly electrochemical energy conversion and storage for powering an increasingly diverse range of applications, ranging from portable power for consumer electronics to potential transport applications [1–6]. This allowed for rapid research in electrochemical energy conversion and storage devices such as fuel cells, supercapacitors, and Li-ion batteries. As the performance of these EEDs depends intimately on the properties of their materials, considerable attention has been given to the research and development of key materials. Micrometer sized bulk materials are reaching their inherent limits in performance and cannot fully satisfy the increasing desires of consumer EEDs. Therefore, the development of new material with high performance is essential to obtain more efficient EEDs. The rapid advances in nanoscience and technology provides new opportunities in achieving highly efficient EEDs such as fuel cells, supercapacitors, and Li-ion batteries. Particularly, the physical properties such as a large surface area and novel size effects of nanostructured materials (NSMs) markedly improve the efficiency of such EEDs [6–11]. Therefore, NSMs are becoming increasingly important in the development of electrochemical conversion and storages devices and hence have attracted great interest in recent years. The development in past years has shown that NSMs have great potential for innovation of new technology for everlasting demand of energy. Toward this aim, the present review article is mainly focused on the recent developments in the synthesis and fabrication of zero-dimensional (0D), one-dimensional (1D), two-dimensional (2D) and three-dimensional (3D) NSMs and their application in EEDs such as fuel cells, supercapacitors, and Li-ion batteries [1–15].

### 1.2. The scope of this review

In this review article, we will briefly describe the classification of NSMs. Subsequently, experimental techniques involved in the synthesis and fabrication of processes of 0D, 1D, 2D and 3D NSMs will be described. This will be followed by an in-depth discussion of the experimental techniques (physical and chemical processes) employed by different researchers to fabricate NSMs. Section 5 addresses the applications of 0D, 1D, 2D and 3D NSMs in EEDs such as fuel cells, supercapacitors, and Li-ion batteries. In this section, we will first describe the working principle of fuel cells, supercapacitors, and Li-ion batteries in their introduction section. Further, recent work on development of 0D, 1D, 2D, and 3D NSMs in the applications of fuel cells, supercapacitors, and Li-ion batteries, will also be described, which will be followed by a discussion of 0D, 1D, 2D and 3D NSMs behavior. The final section will describe the conclusions. Lastly but not least, some issues that need to be clarified in the near future are proposed in final section.

## 2. Classification of nanostructured materials (NSMs)

In the past two decades, hundreds of novel NSMs have been obtained; therefore, the need in their classification is ripened. NSMs as a subject of nanotechnology are low dimensional materials comprising of building units of a submicron or nanoscale size at least in one direction and exhibiting size effects. The first classification idea of NSMs was given by Gleiter in 1995 [16] and further was explained by Skorokhod in 2000 [17]. However, Gleiter and Skorokhod scheme was not fully considered because of 0D, 1D, 2D, and 3D structures such as fullerenes, nanotubes, and nanoflowers were not taken into account. Therefore, Pokropivny and Skorokhod [18] reported a modified classification scheme for NSMs, in which 0D, 1D, 2D and 3D NSMs are included. Herein we classified the NSMs based on the scheme of Pokropivny et al. scheme.

## 2.1. 0D NSMs

A major feature that discriminates various types of nanostructures is their dimensionality. The word “nano” stems from the Greek word “nanos”, which means dwarf [19]. This word “nano” has been assigned to indicate the number  $10^{-9}$ , i.e., one billionth of any unit. In the past 10 years, significant progress has been made in the field of 0D NSMs. A rich variety of physical and chemical methods have been developed for fabricating 0D NMSs with well-controlled dimensions. Recently, 0D NSMs such as uniform particles arrays (quantum dots), heterogeneous particles arrays, core–shell quantum dots, onions, hollow spheres and nanolenses have been synthesized by several research groups [20–24]. Fig. 1 shows the images of different types of 0D NSMs. Moreover, 0D NSMs, such as quantum dots has been extensively studied in light emitting diodes (LEDs) [25], solar cells [26], single-electron transistors [27], and lasers [28].

## 2.2. 1D NSMs

In the last decade, 1D NSMs have stimulated an increasing interest due to their importance in research and developments and have a wide range of potential applications. It is generally accepted that 1D NSMs are ideal systems for exploring a large number of novel phenomena at the nanoscale and investigating the size and dimensionality dependence of functional properties. They are also expected to play an important role as both interconnects and the key units in fabricating electronic, optoelectronic, and EEDs with nanoscale dimensions. The field of 1D NSMs such as nanotubes has attained a significant attention after the pioneering work by Iijima [29]. 1D NSMs have a profound impact in nanoelectronics, nanodevices and systems, nanocomposite materials, alternative energy resources and national security [30]. In Fig. 2, we show the 1D NSMs, such as nanowires, nanorods, nanotubes, nanobelts, nanoribbons, and hierarchical nanostructures, which have been synthesized in our and other laboratories [31–46].

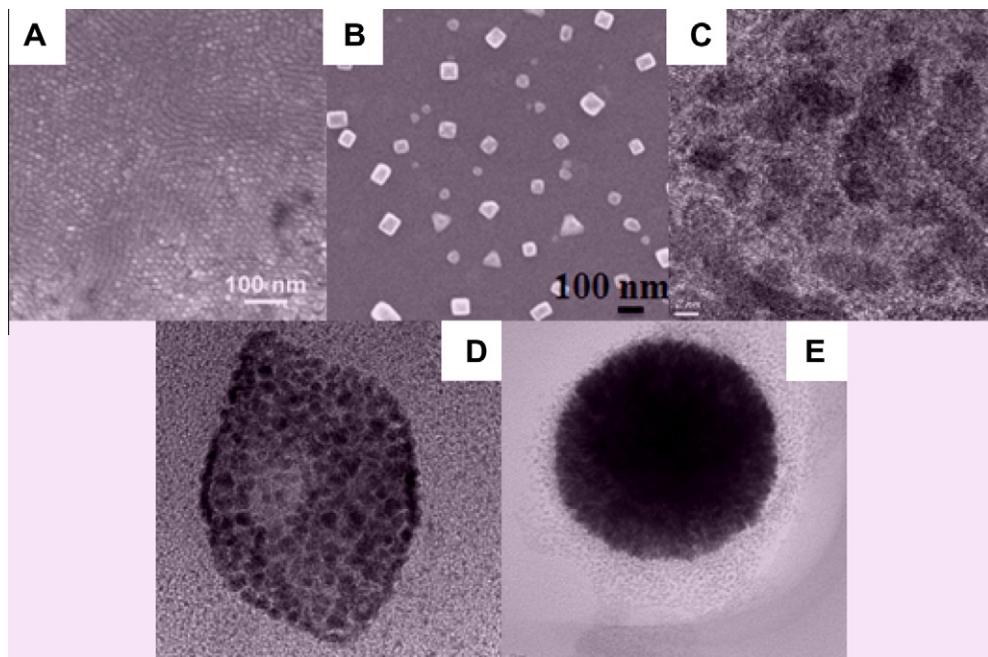


**Fig. 1.** Typical scanning electron microscope (SEM) and transmission electron microscope (TEM) image of different types of 0D NSMs, which is synthesized by several research groups. (A) Quantum dots [20], (B) nanoparticles arrays, (C) core–shell nanoparticles, (D) hollow cubes, and (E) nanospheres. Reprinted by permission of the Wiley-VCH Verlag GmbH & Co. KGaA.

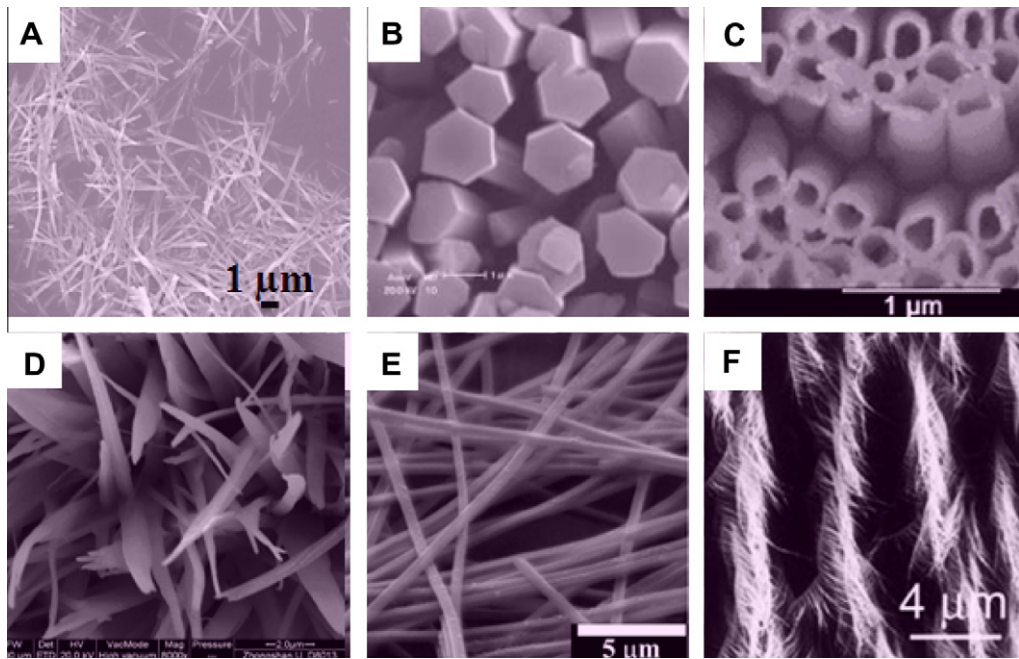


**Fig. 2.** Typical SEM image of different types of 1D NSMs, which is synthesized by several research groups. (A) Nanowires, (B) nanorods [32], (C) nanotubes [33], (D) nanobelts [34], (E) nanoribbons, [35] and (F) hierarchical nanostructures [36]. Reprinted by permission of the Japan Society of Applied Physics, Elsevier, IOP Publishing Ltd., and ACS publishers.

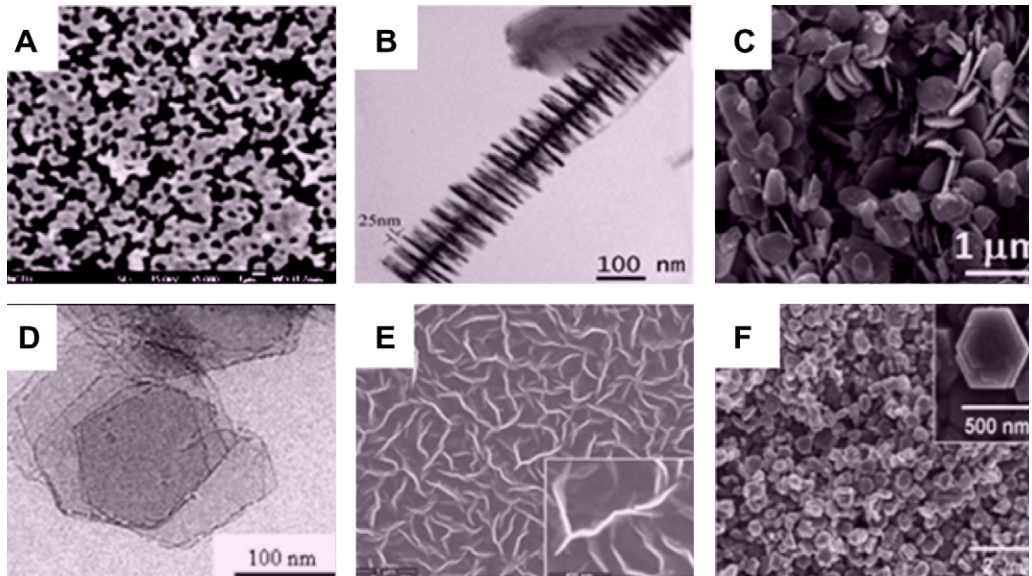


**Fig. 3.** Typical SEM and TEM image of different kinds of 2D NSMs, which is synthesized by our and several research groups. (A) Junctions (continuous islands), (B) branched structures [52], (C) nanoplates [54], (D) nanosheets [55], (E) nanowalls [56], and (F) nanodisks [57]. Reprinted by permission of IOP Publishing Ltd., The American Ceramic Society, and ACS Publishers.

### 2.3. 2D NSMs

2D nanostructures have two dimensions outside of the nanometric size range. In recent years, a synthesis 2D NSMs have become a focal area in materials research, owing to their many low dimensional characteristics different from the bulk properties. In the quest of 2D NSMs, considerable research attention has been focused over the past few years on the development of 2D NSMs. 2D NSMs with certain geometries exhibit unique shape-dependent characteristics and subsequent utilization as building blocks for the key components of nanodevices [47–49]. In addition, a 2D NSMs are particularly interesting not only for basic understanding of the mechanism of nanostructure growth, but also for investigation and developing novel applications in sensors, photocatalysts, nano-containers, nanoreactors, and templates for 2D structures of other materials [50]. In Fig. 3, we show the 2D NSMs, such as junctions (continuous islands), branched structures, nanoprisms, nanoplates, nanosheets, nanowalls, and nanodisks [51–57].

### 2.4. 3D NSMs

Owing to the large specific surface area and other superior properties over their bulk counterparts arising from quantum size effect, 3D NSMs have attracted considerable research interest and many 3D NSMs have been synthesized in the past 10 years [1–15]. It is well known that the behaviors of NSMs strongly depend on the sizes, shapes, dimensionality and morphologies, which are thus the key factors to their ultimate performance and applications. Therefore it is of great interest to synthesize 3D NSMs with a controlled structure and morphology. In addition, 3D nanostructures are an important material due to its wide range of applications in the area of catalysis, magnetic material and electrode material for batteries [1–15]. Moreover, the 3D NSMs have recently attracted intensive research interests because the nanostructures have higher surface area and supply enough absorption sites for all involved molecules in a small space [58]. On the other hand, such materials with porosity in three dimensions could lead to a better transport of the molecules [58–60]. In Fig. 4, we show the typical

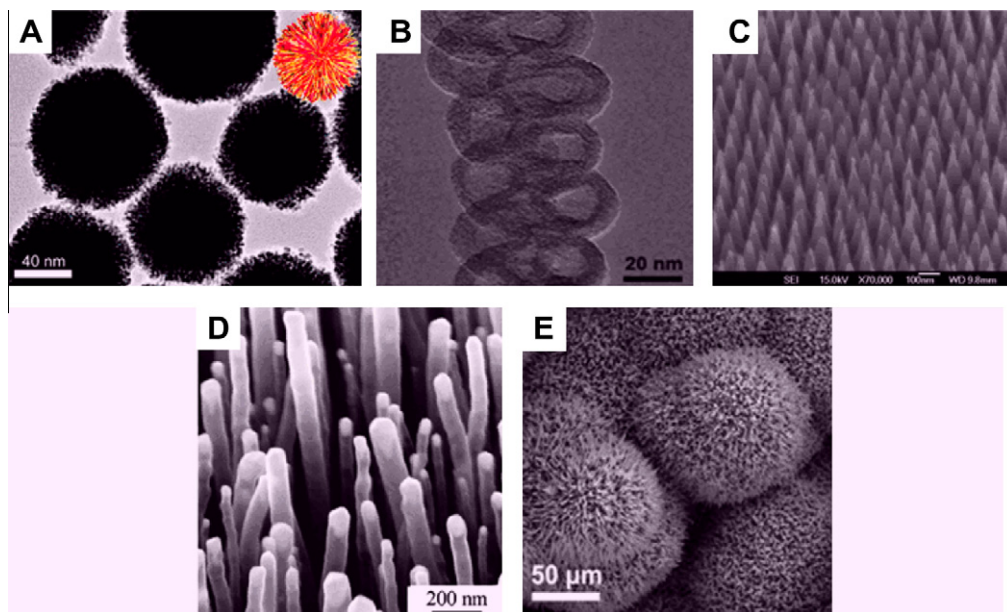


**Fig. 4.** Typical SEM and TEM image of different kinds of 3D NSMs, which is synthesized by our and several research groups. (A) Nanoballs (dendritic structures) [61], (B) nanocoils [62], (C) nanocones, (D) nanopillars [63], and (E) nanoflowers [64]. Reprinted by permission of ACS Publishers.

3D NMSs, such as nanoballs (dendritic structures), nanocoils, nanocones, nanopillars and nanoflowers [61–65].

### 3. Synthesis of NSMs

NSMs have attracted a great deal of interests from both fundamental science and technological application points of view because their physical, chemical, electronic and magnetic properties show dramatic difference from higher dimensional counterparts. And based on their dimension, NSMs can be divided into 0D, 1D, 2D and 3D NSMs, which generate a series of novel physical and chemical properties that differ much from those of conventional bulk materials. Many techniques have been developed to synthesize and fabricate 0D, 1D, 2D and 3D NSMs with controlled size, shape, dimensionality and structure. The physical or chemical methods are generally used for synthesizing and fabricating 0D, 1D, 2D and 3D NSMs. There are a variety of physical and chemical methods for synthesizing and fabricating 0D, 1D, 2D and 3D NSMs. Therefore, first we will give a brief description of these techniques for synthesizing and fabricating 0D, 1D, 2D and 3D NSMs. After the description of these techniques, we will discuss the details of the different types of NSMs such as 1D, 2D and 3D, which is synthesized or fabricated by either a physical or a chemical process.

#### 3.1. Physical methods

Physical method provides an eco-friendly path to fabricate surface clean 0D, 1D, 2D and 3D NSMs. Currently, there are various physical methods used for the synthesis and fabrication of 0D, 1D, 2D and 3D NSMs which will be described in more detail below.

##### 3.1.1. Evaporation technique

Evaporation (Fig. 5) is a common method of thin film deposition. Various evaporation techniques, such as thermal and ion assisted evaporation are used for the synthesis and production of 0D, 1D, 2D and 3D NSMs. One of the most common and most widely-used techniques involves the synthesis of single-phase metals and ceramic oxides by the inert-gas evaporation technique. The schematic diagram of thermal evaporation equipment is shown in Fig. 5. In this technique, the evaporated atoms or molecules loss energy via collisions with the gas atoms or molecules and undergo a homogeneous condensation to form atom clusters in the vicinity of a cold-powder collection surface. In order to prevent further aggregation or coalescence of the clusters, the formed clusters should be removed from the region of deposition [66,67].

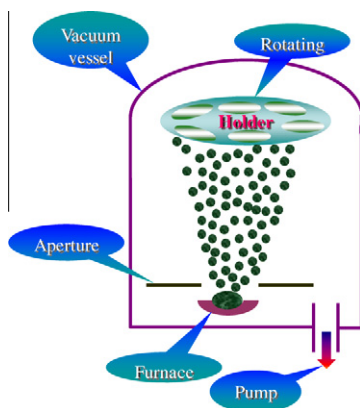


**Fig. 5.** A schematic drawing of thermal evaporation chamber setup.

### 3.1.2. Sputtering technique

Nowadays different kind of sputtering system such as ion-assisted deposition, ion beam, reactive, high-target utilization, high power impulse magnetron and gas flow sputtering used for synthesis of NSMs. A typical sputtering process, generally involves the ejection of atoms or clusters of designated materials by subjecting them to an accelerated and highly focused beam of inert gas such as helium or argon [66]. A schematic diagram of a typical sputtering system is shown in Fig. 6.

### 3.1.3. Lithography processes

Lithography is more versatile and easy to implement process for producing the self-assembled of 0D, 1D, 2D and 3D NSMs on different types of substrates. Lithography is also a rapid and effective method for surface patterning, which is compatible with a large variety of materials. Lithography includes many different kinds of surface preparation in which a design is transferred from a photomask or reticle onto a substrate surface that would allow multiple copies to be made from one exposure. Lithography techniques can be divided in two categories on the basis of the nanofabrication approaches:

- (1) Unconventional approaches such as soft nano-imprint lithography, [68,69] nanosphere lithography, [70,71] colloidal lithography, [72] nano-imprint lithography, [73] and solution-phase synthesis [74,75].
- (2) Conventional approaches like e-beam lithography and focused ion beam lithography.

Unconventional approaches are more preferable to conventional approaches. Lithographic patterning is achieved by various molding processes, for instance nanoimprint lithography, hot embossing, and elastomer molding. Lithography has become a widely used technique by many researchers in fields of physics, chemistry, and biology [76].

### 3.1.4. Hot and cold plasma

A plasma is sometimes referred to as being “hot” if it is nearly fully ionized, or “cold” if only a small fraction, (for instance 1%), of the gas molecules are ionized, but other definitions of the terms “hot plasma” and “cold plasma” are common. Even in cold plasma, the electron temperature is still typically several thousand degrees Celsius. Fig. 7 shows a schematic drawing of the hot plasma equipment for producing nanostructured material in powder form. Generally such equipment consists of an arc melting chamber and a collecting system. The thin films of alloys were prepared from highly pure metals by arc melting in an inert gas atmosphere. Each arc-melted ingot was flipped over and

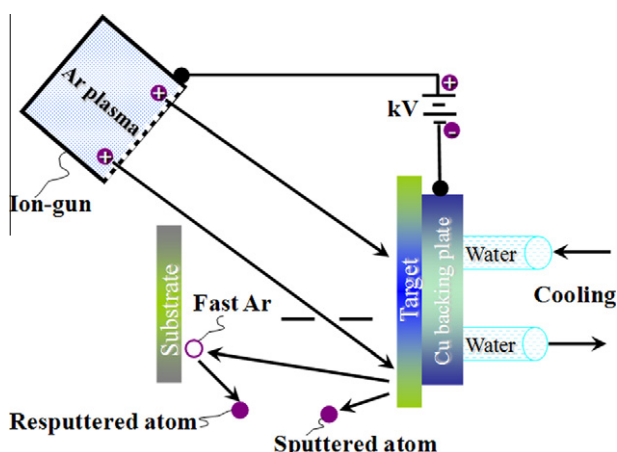
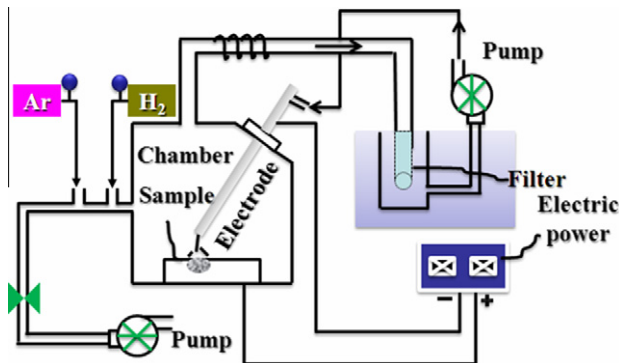


Fig. 6. A schematic drawing of a typical sputtering system.



**Fig. 7.** A schematic drawing of hot plasma.

remelted three times. Then, the thin films of alloy were produced by arc melting a piece of bulk materials in a mixing gas atmosphere at a low pressure. Before the ultrafine particles were taken out from the arc-melting chamber, they were passivated with a mixture of inert gas and air to prevent the particles from burning up.

Fig. 8 shows a schematic drawing of the cold plasma equipment for producing nanowires in large scale and bulk quantity. Generally such equipment consists of a conventional horizontal quartz tube furnace and an inductively coupled coil driven by a 13.56 MHz radio-frequency (rf) power supply. Recently, Zheng et al. used the cold plasma system to synthesize the silicon oxynitride nanowires [77]. In a typical synthesis of silicon oxynitride nanowires, they used nickel coated silicon wafers as a substrate. The more explanation on cold plasma methodology to fabricate the silicon oxynitride nanowires can be found in the article [77]. For that reason, we did not discuss in more detail here about the production of silicon oxynitride nanowires.

### 3.1.5. Spray pyrolysis

Spray pyrolysis (Fig. 9) is basically a solution process in which nanoparticles are direct deposited by spraying a solution on a heated substrate surface, where the constituent react to form a chemical compound. The chemical reactants are selected such that the products other than the desired compound are volatile at the temperature of deposition. The spray pyrolysis represents a very simple and relatively cost-effective processing method (particularly in regard to equipment costs) as compared to many other film deposition techniques [78,79]. Spray pyrolysis offers an extremely easy technique for preparing films of any composition and does not require high-quality substrates, chemicals, expen-

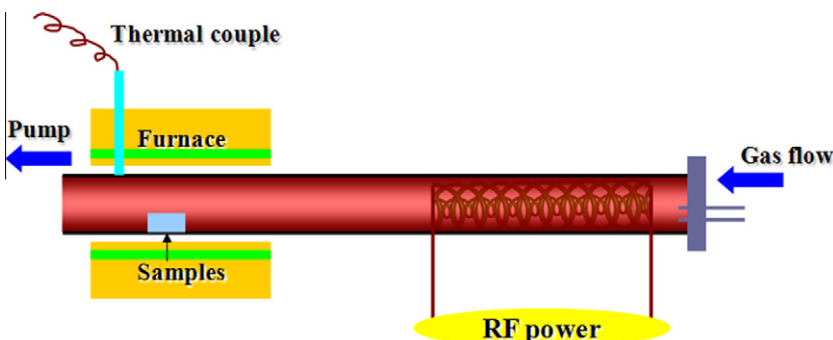


**Fig. 8.** A schematic drawing of cold plasma.

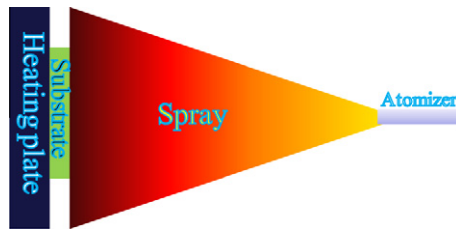


**Fig. 9.** Schematic diagram of a chemical spray pyrolysis.

sive vacuum apparatus and exotic gases. The spray pyrolysis system consists basically of an atomizer, precursor solution, substrate heater, and temperature controller. Various types of atomizers are usually used in spray pyrolysis technique, such as air blast (the liquid is exposed to a stream of air) [80], ultrasonic (ultrasonic frequencies produce the short wavelengths necessary for fine atomization) [80] and electrostatic (the liquid is exposed to a high electric field) [80].

### 3.1.6. Inert gas phase condensation technique

The inert gas phase condensation (IGC) method (Fig. 10) is one of the most promising methods for the production of low-cost NSMs. Generally, IGC method has been used to synthesize numerous single phase metals, semiconductors and metal oxide nanoparticles. It is based on nanoparticles generated by evaporation and condensation (nucleation and growth) in a sub-atmospheric inert-gas environment [81,82]. The generation of atoms clusters by IGC proceeds by evaporating a precursor material, either a single component or a compound, in a gas maintained at a low pressure. The evaporated atoms or molecules undergo a homogeneous condensation to form atom clusters (lose energy) via collisions with gas atoms or molecules in the vicinity of a cold surface to condense on it.

### 3.1.7. Pulsed laser ablation

As a physical gas-phase method for preparing nanosized particles, pulsed laser ablation has become a popular method to prepare high-purity and ultra-fine NSMs of any composition. In this method, the material is evaporated using pulsed laser in a chamber filled with a known amount of a reagent gas and by controlled condensation of nanoparticles onto the support. A schematic view of a pulsed laser ablation for the synthesis of nanoparticles is shown in Fig. 11. As the material atoms diffuse from the target to the substrate, they interact with the gas to form the desired compound (for example, oxide in the case of oxygen, nitride for nitrogen or ammonia, carbide for methane, etc.). The pulsed laser vaporization of metals in the chamber is a modification of the known method for the synthesis of metal compounds in a diffusion cloud chamber and makes it possible to prepare nanoparticles of mixed

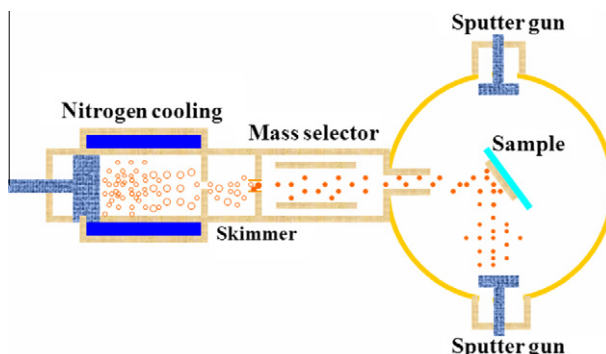


**Fig. 10.** Schematic diagram of IGC method.

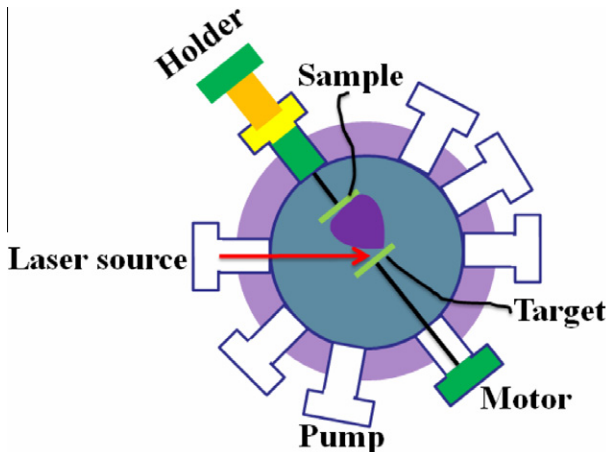


**Fig. 11.** Schematic view of the pulsed laser ablation.

molecular composition, such as mixed oxides/nitrides and carbides/nitrides or mixtures of oxides of various metals. The elemental composition and size distribution of nanoparticles can be altered by changing certain experimental parameters, including composition of the inert gas and the reagent gas in the chamber and varying the temperature gradient and laser pulse power.

### 3.1.8. Sonochemical reduction

Sonochemical reduction is a most widely used physical technique for generation of different kinds of NSMs. Fig. 12 shows the schematic diagram of the sonication system. In this equipment, a multiwave ultrasonic generator and a barium titanate oscillator of 65 mm diameter were used for the ultrasonic irradiation. During the microwave irradiation the vessel was closed. The multiwave ultrasonic generators were operated at 200 kHz frequency with an input power of 200 W. The sonication process was carried out in a temperature-controlled water bath.

### 3.2. Chemical methods

Chemical methods have played a major role in developing materials imparting technologically-important properties through structuring the materials on the nanoscale. However, the primary advantage of chemical processing is its versatility in designing and synthesizing new materials that can be refined into the final end products. The secondary most advantage that the chemical processes offer over physical methods is a good chemical homogeneity, as chemical method offers mixing at the

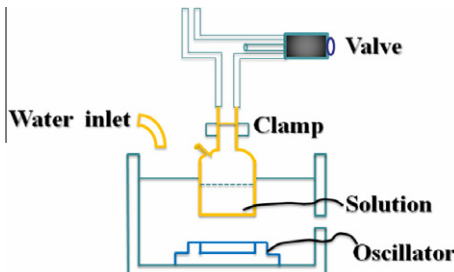


**Fig. 12.** Schematic view of the sonication system.

molecular level [83]. On the other hand, chemical methods frequently involve toxic reagents and solvents for the synthesis of NSMs [84]. In addition, another problem with the chemical methods is the inevitable introduction of byproducts which require subsequent purification steps after the synthesis (in other words, such a process is time consuming). Nevertheless, there are many chemical methods used for the synthesis of 0D, 1D, 2D and 3D NSMs which will be described in more detail below.

### 3.2.1. Lyotropic liquid crystal templates

Lyotropic liquid crystal (LLC) templates, including hexagonal, bicontinuous cubic and lamellar phases, have the potential advantage of producing materials with anisotropic morphologies and nanometer size dimensions with potential in applications, such as drug delivery, catalysis, and tissue engineering [85]. The cross-linked poly(butadiene)-b-poly(ethylene oxide) gels in cubic, hexagonal, and lamellar phases are mechanically and chemically stable [86]. LLC confines the reactants in the limited dimension; and the structures of long-chain order affect the nucleation and growth processes of the products, which could be applied to control the synthesis of the NSMs with the required porosity, morphology, size, and orientation.

Based on previous reports, it is clear that LLC can be used as the perfect template for growing 0D, 1D, 2D and 3D NSMs. The advantage of the synthesis in LLC systems is that it is possible to have very precise control over the nanostructure of the materials. It enables the synthesis of well-defined materials having a long range spatially and orientationally periodic distribution of uniformly sized, whose nanostructures are casts of structures of the LLC phases, by exploiting the rich lyotropic polymorphism. Mountzaris's group synthesized 0D, 1D and 2D semiconducting ZnSe nanostructures using cubic, hexagonal and lamellar LLC phases as templates, respectively [87]. The shape and size of the resulting nanostructures could be controlled by selecting the LLC phases as templates.

### 3.2.2. Electrochemical deposition

Electrodeposition is a process that uses electrical current to deposit a composite layer nanostructure-containing material onto a desired substrate. Basically this method involves the use of a two-electrode or three-electrode electrochemical system. Recently, the electrochemical deposition techniques vastly used by many researchers for the 0D, 1D, 2D and 3D NSMs [88–91]. Electrodeposition of the 0D, 1D, 2D and 3D NSMs were carried out by using pulse electrodeposition (PE) in a three electrode cell system. Fig. 13 shows the setup of an electrochemical deposition facility. As shown in Fig. 13, a thin Pt wire, saturated calomel electrode (SCE) and sample, as counter, reference and working electrodes, respectively, were used. In the PE, there are four operation parameters influencing the depositing of nanoparticles on the substrate: The higher potential, the lower potential, the potential on time, and the potential off time. By applying specific potential pulses with time interval for the total experimental time, 0D, 1D, 2D and 3D NSMs were deposited on the working electrode. On the other hand, in case of a two-electrode electrochemical system, we only used counter electrode and working electrode.

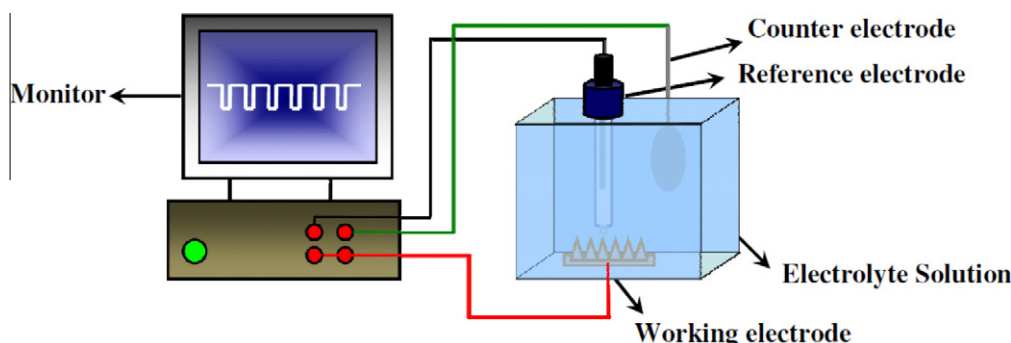
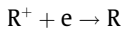


**Fig. 13.** Schematic drawing of an electrodeposition setup.

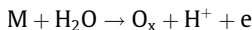
### 3.2.3. Electroless deposition

Electroless plating is a well-established low-cost, non-hazardous chemical process, and also known as a non-galvanic type of depositing technique that involves numerous simultaneous reactions in an aqueous system. The electroless plating is carried out in absence of external electrical power. The reaction is accomplished via released hydrogen, which acts as a reducing agent and is oxidized, thus producing a negative charge on the surface of the substrate (Fig. 14).

For metal deposition



For oxidation



### 3.2.4. Hydrothermal and solvothermal techniques

Conceptually, hydrothermal system can be defined as the use of water as reaction medium in a sealed reaction container when the temperature is raised above 100 °C. Basically, it is used in the synthesis of single crystals that depends on the solubility of minerals in hot water under high pressure. The crystal growth is carried out in an autoclave, in which a nutrient is supplied along with water. A temperature gradient is maintained at the opposite ends of the growth vessel so that the hotter end dissolves the nutrient and the cooler end causes seeds to take additional growth. The hydrothermal technique is more suitable for better-quality and growth of larger crystals, while maintaining a good control over their composition. A schematic diagram of a hydrothermal system is depicted in Fig. 15. The disadvantages of the hydrothermal technique include the need of expensive autoclaves, good quality seeds of a fair size and the impossibility of observing the crystal as it grows.

Solvothermal synthesis is a commonly used chemical method to prepare the different kinds of NSMs, an experimental sketch is shown in Fig. 16. Solvothermal synthesis route is very similar to the hydrothermal route (where the synthesis is conducted in a stainless steel autoclave), the only difference being that the precursor solution is usually not aqueous but this is not always. By changing certain experimental parameters, including reaction temperature, reaction time, solvent type, surfactant type, and precursor type, it is possible to precise control the size, shape distribution, and crystallinity of metal oxide nanoparticles or nanostructures that obtained.

### 3.2.5. Sol–gel technique

The sol–gel process (Fig. 17), also known as chemical solution deposition, is a wet chemical synthesis approach that can be used to generate nanoparticles by gelation, precipitation, and hydrothermal treatment [92]. The sol–gel method is widely used in the fields of materials and chemical science. Such methods are used primarily for the fabrication of materials starting from a chemical solution (or sol) that acts as the precursor for an integrated network (or gel) of either discrete particles or network polymers. By changing certain experimental parameters including dopant introduction [93], heat treatment [94] and properly choosing some other surfactants, including inverted micelles [95], polymer matrix architecture based on block copolymers [96] or polymer blends [97], porous glasses [98]

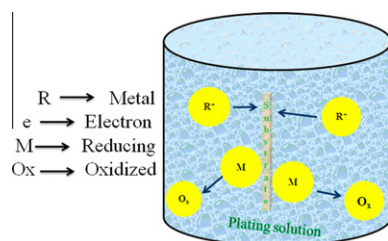


**Fig. 14.** Schematic drawing of an electroless plating setup.

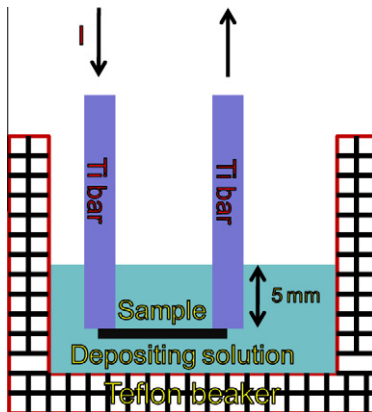


**Fig. 15.** Schematic experimental system for the hydrothermal fabrication of NSMs.

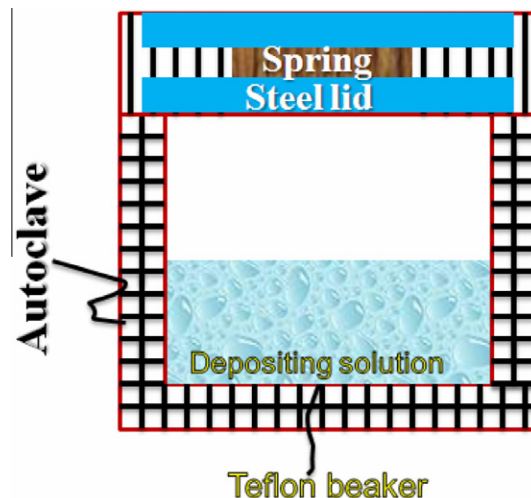


**Fig. 16.** Schematic drawing of solvothermal setup.

and ex situ particle capping [99], it is possible to control the better size distribution and stability control of quantum-confined semiconductors, metal, metal oxide nanoparticles. Despite the above, the basic chemistry of the sol–gel process is complex due to the different reactivities of the network forming and the network modifying components and the wide variety of reaction parameters [100].

### 3.2.6. Chemical vapor deposition

Chemical vapor deposition (CVD) is a chemical process in which gaseous molecules transform into a solid material, in the form of 0D, 1D, 2D and 3D NSMs, on the surface of a substrate. In a typical CVD process (Fig. 18), the substrate is exposed to one or more volatile precursors, which react and/or decompose on the substrate surface to produce the desired deposit. A basic CVD process consists of the following five steps:

- (1) A predefined mix of reactant gases and diluent inert gases are placed into the chamber by the mass flow controller at a specified flow rate.

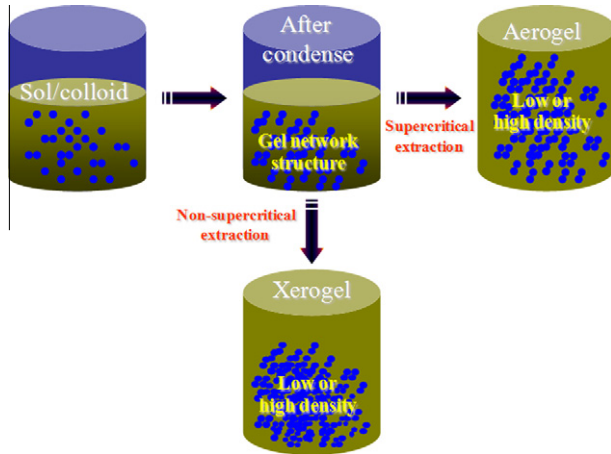


**Fig. 17.** Basic scheme for the sol-gel process.

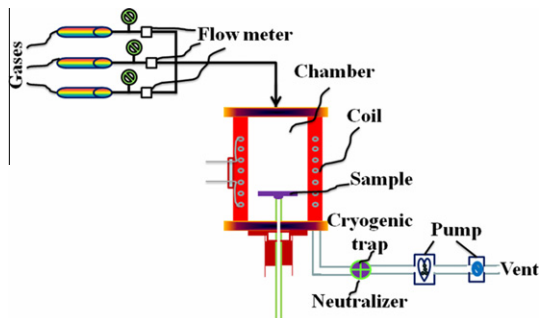


**Fig. 18.** Schematic diagram of the CVD experimental set-up.

- (2) The gas species move to the surface site.
- (3) The reactants get adsorbed on the surface site.
- (4) The reactants undergo chemical reactions with the substrate to form the NSMs.
- (5) The gaseous reaction products are desorbed and evacuated from the chamber.

### 3.2.7. Laser chemical vapor deposition technique

In this technique, photoinduced processes are used to initiate the chemical reaction. During LCVD, three kinds of activation should be considered. First, if the thermalization of the laser energy is faster than the chemical reaction, pyrolytic and/or photothermal activation is responsible for the activation. Secondly, if the first chemical reaction step is faster than the thermalization, photolytical (non-thermal) processes are responsible for the excitation energy. Thirdly, combinations of the different types of activation are often encountered.

In pyrolytic LCVD, the focused laser beam is used as a source of heat to induce the chemical reaction leading to CVD. Pyrolytic LCVD process slightly depends on the laser beam wavelength (i.e., many different sources can be used), and that high rates of deposition can be reached. In addition, localized and small deposits can be simply achieved. As shown in Fig. 19, photolytic LCVD is based on the photodecomposition of molecules near the substrate with subsequent deposition of the desired species (selective excitation of precursor molecules), and laser beam is usually aligned parallel to the substrate [101].

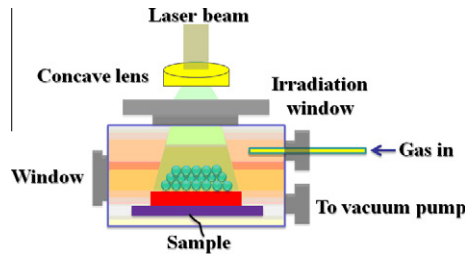


**Fig. 19.** Schematic of photolytic LCVD system.

A combination of both techniques (pyrolytic + photolytic LCVD) is generally referred to as photo-physical LCVD, and this type of activation make it possible to create the best of the advantages and disadvantages of pyrolytic and photolytic LCVD. In this system, a twin beam (UV + longer wavelength) or a single-beam (at intermediate wavelength) is used to activate the combined pyrolytic/photolytic process.

### 3.2.8. Laser pyrolysis

Laser pyrolysis technique (Fig. 20) requires the presence in the reactive medium of a molecule absorbing the CO<sub>2</sub> laser radiation. In most cases, the atoms of a molecule are rapidly heated via vibrational excitation and are dissociated. But in some cases, a sensitizer gas such as SF<sub>6</sub> can be directly used [102]. The heated gas molecules transfer their energy to the reactive medium by collisions leading to dissociation of the reactive medium without, in the ideal case, dissociation of this molecule. Rapid thermalization occurs after dissociation of the reactants due to transfer collision. Nucleation and growth of NSMs can take place in the as-formed supersaturated vapor. The nucleation and growth period is very short time (0.1–10 ms). Therefore, the growth is rapidly stopped as soon as the particles leave the reaction zone. The flame-excited luminescent is observed in the reaction region where the laser beam intersects the reactant gas stream. Since there is no interaction with any walls, the purity of the desired products is limited by the purity of the reactants. However, because of the very limited size of the reaction zone with a fast cooling rate, the powders obtained in this wallless reactor present a low degree of agglomeration. The particle size is small (~5–50 nm range) with a narrow size distribution. Moreover, the average size can be manipulated by optimizing the flow rate, and, therefore, the residence time in the reaction zone.

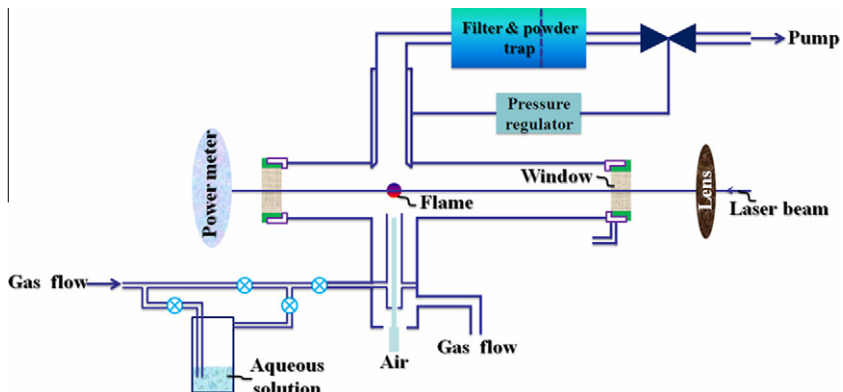


**Fig. 20.** Schematic diagram of a typical laser pyrolysis apparatus.

## 4. Synthesis of 0D, 1D, 2D and 3D NSMs

### 4.1. Synthesis of 0D NSMs

#### 4.1.1. Synthesis of 0D NSMs by physical processes

The thermal evaporation technique is the facile and most widely used technique for the synthesis of 0D NSMs. More recently, Chang et al. employed the facile solid evaporation route to prepare the tungsten trioxide nanoparticles in high yield [103]. Shen et al. used the thermal evaporation technique to synthesize both core/shell Ge/SiO<sub>2</sub> and Ge/CdS nanospheres [104]. These core/shell Ge/SiO<sub>2</sub> and Ge/CdS nanospheres were synthesized at 1250 °C. After the thermal evaporation technique, the sputtering method is another most widely used technique for the synthesis of 0D NSMs. Suzuki et al. reported a very clean method for synthesizing noble nanoparticles, such as Au, Ag, and Pt, in ionic liquids using a sputter deposition technique without any additives [105–108]. Suzuki et al. also employed this sputtering method to prepare metal and hollow indium oxide nanoparticles [109]. Balasubramanian et al. employed the magnetron plasma-sputtering and evaporation method to prepare TiO<sub>2</sub>-paraffin core-shell nanoparticles on Si substrate [110]. But it's difficult to control the size of nanoparticles by evaporation and sputtering method. Then, many researchers have focused on the lithographic technique [111–114]. The lithographic technique is an inexpensive, inherently parallel, and high-throughput technique capable of producing well-ordered nanoparticles. Hulteen et al. used the lithography process to synthesize the size-tunable Ag nanoparticles [112]. Hu et al. made the uniform worm-shaped polymeric nanoparticles by using the lithographic method [113]. Hung et al. used the lithographically confined DNA origami to prepare the large-area spatially ordered arrays of gold nanoparticles [114].

The hot and cold plasma have received more attention over the last decade for the generation of 0D NSMs such as nanospherical particles and quantum dots. Arc plasma is widely used hot plasma, which offers unique advantages for instance high chemical reactivity, high enthalpy to enhance reaction kinetics, oxidation and reduction atmospheres in accordance with required chemical reactions, and quick quenching to produce chemical non-equilibrium materials [115]. Moreover, the unique attributes of plasma provide a more promising solution. It is known that the arc plasma can reach a temperature higher than 10,000 °C and therefore can melt all substances. It is also quite attractive as a low-cost and semi-commercial-scale processing route when hydrogen is used to plasma [116–119]. Chen et al. used the arc plasma method to synthesize the tin oxide nanoparticles [120]. Ohno et al. made precursory research in hydrogen plasma metal reaction and found that pure elemental nanoparticles are produced for non-hydride formation elements, and hydride nanoparticles are usually obtained for hydride formation elements [121–123]. Li et al. systematically investigated the complex alloys and found that hydrogen plasma metal reaction is also available for alloy nanoparticles, but composition and phase constituents of the nanoparticles are often different from the starting alloys [124–127]. An arc-plasma method was used to synthesize Fe and composite Fe-TiN nanoparticles and to study their effects of CO coadsorption on the hydrogen desorption [128]. A large amount of hydrogen desorption was observed. On the other hand, rf cold plasma is a very convenient method to synthesize NSMs and it is more effective in particle size and morphology control compared with hot plasma. Addamo et al. employed the cold plasma such as microwave which was successfully used to prepare TiO<sub>2</sub> nanoparticles [129]. Irzh et al. reported a new method to synthesize ZnO and/or Zn nanoparticles on the glass quadratic slides by microwave plasma whose electrons are the reducing agents [130]. They observed that the ZnO and/or Zn particles have the size in the range of a few micrometers to ~20 nm. The size of the nanoparticles can be controlled by the type of the precursor and its concentration. The rf thermal plasmas supply conditions such as very high temperature, intensive heat and mass transfer conditions, and very rapid cooling of reaction products which are favorable for the synthesis of nanosized particles. Feczko et al. used the rf thermal plasmas to prepare the Ni-Zn ferrite nanoparticles and to purify histidine-tagged proteins [131]. More recently, Huang et al. [132] used the ultrasonic spray pyrolysis process to synthesize the porous Bi<sub>2</sub>WO<sub>6</sub> microsphere. In a typical synthesis of porous Bi<sub>2</sub>WO<sub>6</sub> microsphere, bismuth citrate and tungstic acid are used as precursors in an aqueous solution. The obtained porous microspheres have a higher crystallinity. The formation of the porous structure in the as-synthesized microspheres can be attributed to the presence of citrate

anions and in situ produced carbon residues that can work as capping agents and templates, respectively. However, the IGC technique is also used for the synthesis of 0D NSMs [133]. In 2006, Song et al. [134] prepared the pure rare-earth metals by an inert gas phase condensation technique. The production of the final products will depend on the evaporation parameters. For instance, in highly purified Ar gas at low pressure ( $10^{-1}$  Torr), the average size of the nanoparticles could be optimized in the range of 20–80 nm when the voltage is applied between 10 and 20 V. The input current and evaporation time are ranging between 80–200 A and 0.5–3 h, respectively. Pulsed laser ablation [135,136] is one of the most versatile techniques to grow 0D NSMs such as core/shell nanoparticles [137,138]. In addition, a pulsed laser ablation system can be facilely controlled. Zeng et al. [137] synthesized the Zn-ZnO core/shell nanoparticles by pulsed laser ablation in liquid medium. When the concentration of surfactant is higher than critical micelle concentration, the ZnO nanoparticles changed to a Zn-ZnO core/shell structure. Umezu et al. [138] fabricated the core-shell structured silicon nanoparticles via pulsed laser ablation. In a synthesis of core-shell structured silicon nanoparticles, first the vacuum chamber is evacuated to less than  $1.0 \times 10^{-5}$  Pa, and then high-purity nitrogen gas is flowed into a chamber. Next, a pulsed laser beam is focused onto a Si target. The gap between the target and the substrate is  $\sim 23$  mm. The diameter of core is  $\sim 8$  nm and thickness of shell is  $\sim 3$  nm. Sonochemical reduction has become an important process in chemical field in recent years. It causes the formation of particles with a much smaller size and higher surface area [139–142]. Kumar et al. [143] synthesized the Au–Ru bimetallic nanoparticles via co-reduction and sequential sonochemical reduction of Au(III) and Ru(III) ions. The average diameter of Au–Ru bimetallic nanoparticles increased with respect to the increase of the Ru molar ratio. In the same year, Atobe et al. [142] reported the synthesis of poly-pyrrole-encapsulated platinum nanoparticles (PPy/Pt-NPs) by an easy single-step sonochemical reduction. They also reported that the polypyrrole (PPy) covers on the nanoparticles were able to work as a filter for substrate molecules, and thus the substrate selectivity could be controlled in the catalytic processes. Based on the above literature review, we conclude that the sonochemical reduction technique has an advantage over other preparation methods due to the unusual experimental conditions generated during acoustic cavitation [143,144]. Thus, the physical method provides a convenient and universal way to obtain nanoparticles with controllable microstructure.

#### 4.1.2. Synthesis of 0D NSMs by chemical processes

The template based method is most widely used to synthesize the 0D NSMs such as core–shell, quantum dots, and hollow sphere nanoparticles [20,145–148]. Recently, Nash et al. reported a template method for synthesizing the temperature-responsive  $\gamma$ -Fe<sub>2</sub>O<sub>3</sub>-core/Au-shell nanoparticles [145]. For the synthesis of  $\gamma$ -Fe<sub>2</sub>O<sub>3</sub>-core/Au-shell nanoparticles, they were using the “smart” diblock copolymer micelles as template. The amphiphilic diblock copolymer chains were synthesized using reversible addition–fragmentation chain-transfer with a thermally responsive “smart” poly(*N*-isopropylacrylamide) block. An amine-containing poly(*N,N*-dimethylaminoethylacrylamide) block can act as a reducing agent during gold shell formation. Li et al. reported template-based synthesis of homogeneous hollow core–shell ferrite ( $MFe_2O_4$ , M = Zn, Co, Ni, Cd) [146]. In their report, they synthesized hollow core–shell nanoparticles of spinel ferrites ( $MFe_2O_4$ , M = Zn, Co, Ni, Cd) via carbonaceous saccharide microspheres as template. By adjusting the concentration of metal salts, it was possible to manipulate the core size and shell thickness of hollow spheres. Kim et al. applied the template method to prepare the CdSe quantum dots [20]. For the synthesis of CdSe quantum dots, they applied a mesoporous silica thin film template, whose pore structure is composed of  $\sim 8$  nm sized vertical channels in a hexagonal symmetry on the graphene surface, as a nanoporous mask. The nanochannels exert resistance against the diffusion of electrolytes and, thus, function as a potential-equalizer to suppress the preference for the edge and defect sites. They were able to form CdSe quantum dots into a hexagonal array structure by electrochemically deposited CdSe particles into the pores of the mesoporous silica film template.

Nowadays, the LLC template approach is one of the most popular techniques for the synthesis of the 0D NSMs. Ding and Gin [147] reported a new strategy for synthesizing Pd nanoparticles with both good stability and catalytic activity by using a cross-linked LLC assembly as an organic template. In addition, Yamauchi et al. [148] was using different reducing agents (in order to control both the formation of reaction nuclei and the subsequent deposition of the Ni metal) to synthesis the highly

ordered mesoporous Ni particles. During the preparation of nanoparticles, it is important to identify suitable reducing agents (or combinations of reducing agents) which can control both the formation of metal nuclei and the growth to preserve the well ordered LLC structures in deposited metal.

One-step electrodeposition synthesis of OD NSMs has attracted much attention over the past decade [149–151]. Saez et al. [149] use a three-electrode electrochemical cell to deposit the iron nanoparticles onto the boron-doped diamond substrate. 1 M NH<sub>4</sub>F aqueous solution is used for deposition of iron nanoparticles. They also reported that the deposition rate of iron nanoparticles is mainly affected by concentration, deposition time, and deposition potential. Day et al. [150] also deposit the metal (Pd and Pt) nanoparticles on networks of pristine single walled carbon nanotubes (SWNTs). In addition, they systematically investigated the effect of electrode potential and deposition time on the nanoparticle formation process. They found that the short deposition times and high driving forces favoring the formation of ultra-small particles. Tang et al. [151] prepared the silver nanoparticles on dielectric silica spheres via a facile and one-step electrodeposition method. Under optimized conditions, silver nanoparticles with sizes of 8–10 nm in diameter can be deposited onto the colloidal silica spheres. Electroless plating methods have also been employed to prepare the OD NSMs [152,153]. For instance, Dryfe et al. [152] used the electroless plating method to deposit the Pd nanoparticles at the bare water/1,2-dichloroethane interface, and for the “templated” deposition of Pd within the 100 nm diameter pores of  $\gamma$ -alumina membranes. Later, Chang et al. [153] used a low cost electroless nickel plating process to produce magnetic nickel–tungsten–phosphorus mesoparticles with diameters ranging between 100 and 500 nm on silica templates of ~102 nm and gold templates of ~3 nm. Nowadays, the hydrothermal process is one of the most convenient methods for fabricating NSMs [154–156]. For example, Vu et al. [154] fabricate the CuO, Al<sub>2</sub>O<sub>3</sub>, Ag<sub>2</sub>O and La<sub>2</sub>O<sub>3</sub> doped on SnO<sub>2</sub> nanoparticles by a hydrothermal route at 200 °C for 3 h. The particles obtained have a mean diameter ranging between 6 and 8 nm. More recently, Outokesh et al. [155] prepared the CuO nanoparticles by hydrothermal process. They also optimized the experimental conditions to achieve the high yields, high-purity, and small size of the nanoparticles, that is obtained at temperature = 500 °C, time = 2 h, [Cu(NO<sub>3</sub>)<sub>2</sub>] = 0.1 mol dm<sup>-3</sup>, and pH = 3. Hydrothermal chemical deposits can be classified as one of categories of the solvothermal chemical deposits. The solvothermal process is a simple, one-step method avoiding the use of expensive chemicals in which nanoparticles can be obtained without calcination [157–160]. Zawadzk [159] synthesized ceria nanoparticles by microwave-assisted solvothermal process under mild conditions of temperature and pressure. For the synthesis of ceria nanoparticles, a diethylene glycol solution containing metal nitrate and hexamine as precipitating agent was used. The obtained powder is sphere-like with an average particle size of ~3 nm. Hosokawa et al. [160] fabricated the rare earth iron-mixed oxide nanoparticles by solvothermal reactions of Yb(OAc)<sub>3</sub> and Fe(acac)<sub>3</sub>, Yb(OAc) and FeCl<sub>3</sub>, and YbCl<sub>3</sub> and FeCl<sub>3</sub>. They also found the starting materials, solvents, and amine additives which greatly affect the size of nanoparticles. The sizes of o-YbFeO<sub>3</sub> acquired by using reaction in 1,5-pentanediol and 1,6-hexanediol are ~59 nm and ~49 nm, respectively, which are smaller than that obtained in 1,4-butanediol (~76 nm). Very recently, Yamauchi et al. [161] prepared Ni–Co (core–shell) nanoparticles via sol–gel process. In a typical synthesis, first nickel(II) acetate and cobalt(II) formate complexes are used with a oleylamine in a one-pot reaction under microwave irradiation. The Ni–Co (core–shell) nanoparticles are obtained at ~498 K through the redox reaction between oleylamine and Ni<sup>2+</sup> in a mixture of nickel(II) acetate and cobalt(II) formate complexes with oleylamine. The Ni–Co (core–shell) nanoparticles with an average size of ~71.0 nm are consisted of a Ni core with a diameter of ~46.9 nm, and Co shell with thickness ~10.0 nm. Recently, researchers are using a modified CVD technique for the fabrication of OD NSMs [162–165]. Palgrave and Parkin [162] used aerosol assisted CVD technique to fabricate the Au nanoparticles on glass substrate. Toluene is used as a precursor to deposit gold nanoparticles onto glass. The sizes of Au nanoparticles are ~100 nm. Boyd et al. [165] developed a new CVD process that can be used to selectively deposit materials of many different types. In this technique, they used the plasmon resonance in nanoscale structures to create the local heating, which is crucial in order to initiate deposition when illuminated by a focused low-power laser [165]. Elihn et al. [166] synthesized the iron nanoparticles enclosed in carbon shells by laser-assisted chemical vapor decomposition (LCVD) of ferrocene (Fe(C<sub>5</sub>H<sub>5</sub>)<sub>2</sub>) vapor in the presence of the Ar gas. The inner part of a thin carbon shell on the iron core is indicated as a graphitic layer, whereas the outer part of the shell is composed of

amorphous carbon. Domingo et al. [167] fabricated the Au nanoparticles by LCVD on glass and  $\text{CaF}_2$  substrates and their potential for providing enhanced Raman and infrared spectra has been investigated by using one of the dithiocarbamate fungicides, thiram, as a test molecule. Au nanoparticles are prepared on chamber with pressure of  $\sim 5 \times 10^{-6}$  mbar, using an ArF excimer laser operating at 20 Hz. However, development of laser pyrolysis process will open up possibilities in terms of controlling particle-growth mechanisms, i.e. the possibility to optimize the experimental conditions (duration, temperature), in order to control the final shape and composition (grain size, crystalline phase, stoichiometry) of the 0D NSMs [162–171]. Dumitache et al. [168] synthesized the iron-based core-shell nanostructures via laser pyrolysis. In a typical synthesis of iron-based core–shell nanostructures, first by using a cross-flow configuration, the laser radiation is heating a gas phase mixture containing iron pentacarbonyl (vapors) entrained via an ethylene flow. Second, in situ passivation of the pyrophoric iron nanoparticles is done by controlled oxidation process. The diameter of iron-based core–shell nanoparticles is  $\sim 22$  nm. Pignon et al. [171] prepared the  $\text{TiO}_2$  nanoparticles by laser pyrolysis, with the use of an aerosol of TTIP (titanium tetraisopropoxide) as the main precursor sensitized by  $\text{C}_2\text{H}_4$ . The  $\text{TiO}_2$  nanoparticles had the average diameter in the range from 8 nm to 20 nm. Thus, laser pyrolysis is used to make the different type of 0D NSMs.

## 4.2. Synthesis of 1D NSMs

### 4.2.1. Synthesis of 1D NSMs by physical processes

Recently, 1D NSMs such as nanorods, nanowires, and nanotubes have been the focus of materials research because of their unique material properties and their potential applications in EEDs such as fuel cells, batteries and supercapacitors. Although many methods have been developed to fabricate 1D NSMs, the development of practical, facile, simple, low-cost and high-yield methods for fabricating large numbers of 1D NSMs is still a great challenge. Physical techniques, particularly thermal evaporation and sputtering techniques have been regarded as an effective way to fabricate high-quality 1D NSMs. For instance, Pan et al. [172] fabricated uniform Si–CdSSe core/shell nanowires on Au coated quartz using multisource thermal evaporation route. For the synthesis of Si–CdSSe core/shell nanowires, a piece of cleaned silicon wafer was placed at the center of a quartz tube chamber, which was inserted into a horizontal tube furnace. Then, some CdS and CdSe powders with a defined molar ratio were loaded into a ceramic boat. The distances from the CdS powder and the CdSe powder to the center of the furnace are  $\sim 8$  and  $\sim 6$  cm, respectively. Au coated quartz used as a substrate was put downstream in the gas flow. The tube chamber was evacuated and back-flushed with Ar gas until the desired pressure of 100 mbar was reached. A constant flow of argon of 50 sccm was used. The chamber temperature and heating rate were  $1080^\circ\text{C}$  and  $40^\circ\text{C min}^{-1}$ , and maintained for  $\sim 60$  min. After the growth, the furnace was allowed to ramp down to room temperature. Due to the temperature gradient, the temperature at the substrate was measured as  $\sim 600^\circ\text{C}$ , and the temperature at the CdS powder, the CdSe powder, and the silicon piece, are 650, 750, and  $1080^\circ\text{C}$ , respectively. The Si–CdSSe core/shell nanowires have diameters of about several tens of nanometers, and length of several tens of micrometers. The Si–CdSSe core/shell nanowires have uniform radial size with a diameter of  $\sim 50$  nm.

More recently, Sen et al. [173] used a sequential thermal evaporator to fabricate the  $\text{SnO}_2:\text{W}_{18}\text{O}_{49}$  heterostructure nanowires. In their experiment, the synthesis of  $\text{SnO}_2:\text{W}_{18}\text{O}_{49}$  hierarchical heterostructures was carried out using a simple two-step thermal evaporation process. In the first step,  $\text{SnO}_2$  nanowires were grown by thermal evaporation of Sn in a horizontal tubular furnace. In the second step, tungsten oxide nanowires were grown on  $\text{SnO}_2$  nanowires by thermal evaporation of tungsten in a vacuum deposition chamber (pressure of  $2.5 \times 10^{-4}$  mbar). A collection of  $\text{SnO}_2$  nanowires was placed at a distance of  $\sim 2$  cm from tungsten filament and the chamber was evacuated to  $2 \times 10^{-5}$  mbar. The depositions were carried out at temperature of  $\sim 1965^\circ\text{C}$  for 30 min. The pressure inside the chamber was maintained by flow of air through a needle valve. The deposition occurs by slow oxidation of tungsten filament followed by evaporation, as oxides of tungsten are volatile. They have also shown that the density of  $\text{W}_{18}\text{O}_{49}$  nanowires depend on partial pressure of  $\text{O}_2$  and temperature.

Cao et al. [36] used magnetron sputtering to fabricate the unilateral feather-like boron nanowires structured in multiple T- and/or Y-junctions which self-organize into well-ordered arrays. In a typical synthesis of T- or Y-junction boron nanofeathers/Si, a highly pure boron and boron oxide was used. Argon is also used as an inerting gas in the system. During sputtering, the temperature around the substrate was kept at 800–900 °C, and the pressure was kept constant at 2 Pa in an Ar gas flow. The rf sputtering power was 80 W. After 4–6 h deposition, the substrate surface was covered with a boron nanowire film. Fig. 21 shows the SEM images of the resulting products. The diameters of the boron nanowire arms range from 20 to 40 nm, whereas the stems are much thicker (60–100 nm).

Fan et al. [174] fabricated the well-ordered CuO nanowires by direct oxidation of sputter-deposited Cu<sub>3</sub>N film at 300 °C for 90 min. Cu<sub>3</sub>N film was prepared on glass substrates at room temperature. The CuO nanoarrays are vertical to the substrate with a diameter of ~20 nm and a length of ~0.6 μm. The vapor–solid (VS) growth mechanisms are involved in the formation of CuO nanoarrays. According to VS growth mechanisms, the combined action of the self-catalytic effect of the decomposed Cu, the strain effect, and the template effect provided by the columnar structure of the Cu<sub>3</sub>N film promote the growth of well-ordered CuO nanowires.

Yan et al. [175] fabricated Pt nanowire arrays on planar oxide surfaces by combining sub-lithographic nanofabrication and nanoimprint technology. The dimensions of the nanowire arrays were uniform and controllable with nanometer precision. The size of a single Pt nanowire was 12 μm × 20 nm × 5 nm. On a 5 × 5 cm<sup>2</sup> substrate this was equivalent to 8 × 10<sup>8</sup> nanowires. The resultant total exposed metal surface area was larger than 2 cm<sup>2</sup>. Recently, Park et al. [35] used a laser interference lithography and shadow lithography to fabricate the metallic nanowires and nanoribbons. In a typical fabrication of metallic nanowires and nanoribbons, first, a contact mask is fabricated with a photosensitive material, photoresist, by using two-beam laser holography. Then metal is coated by physical vapor deposition using shadow edge lithography either in single- or multi-stage depositions. Nanowires are defined in this paper as straight as-deposited, whereas nanoribbons are broken

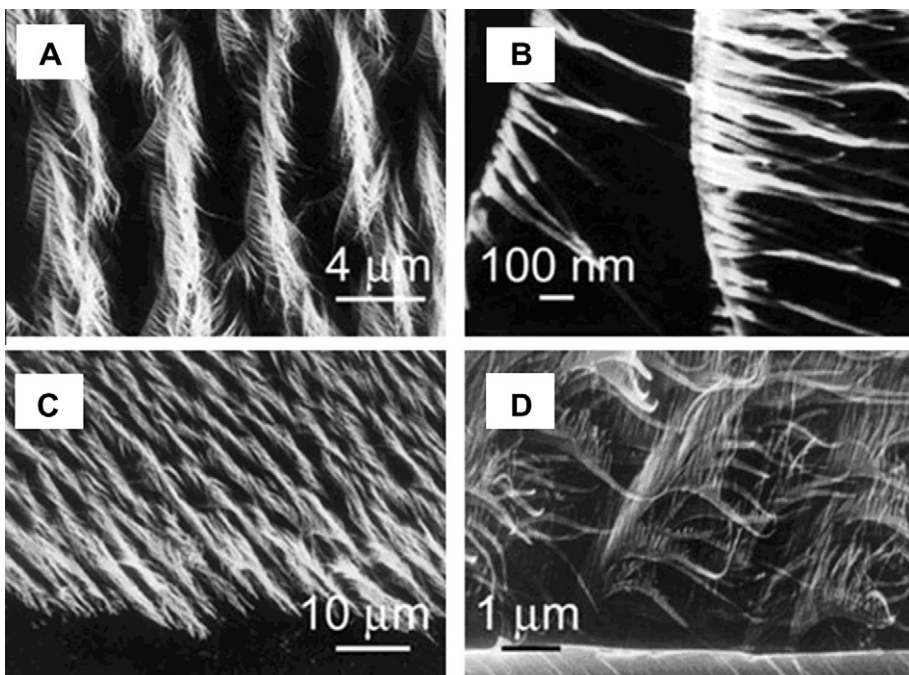


**Fig. 21.** Multiple Y- and/or T-junction boron nanofeather arrays. (A) Low- and (B) high-magnification SEM images. (C) Side-view SEM image. (D) Cross-sectional SEM image. Reprinted from Ref. [36] with permission of IOP Publishing Ltd.

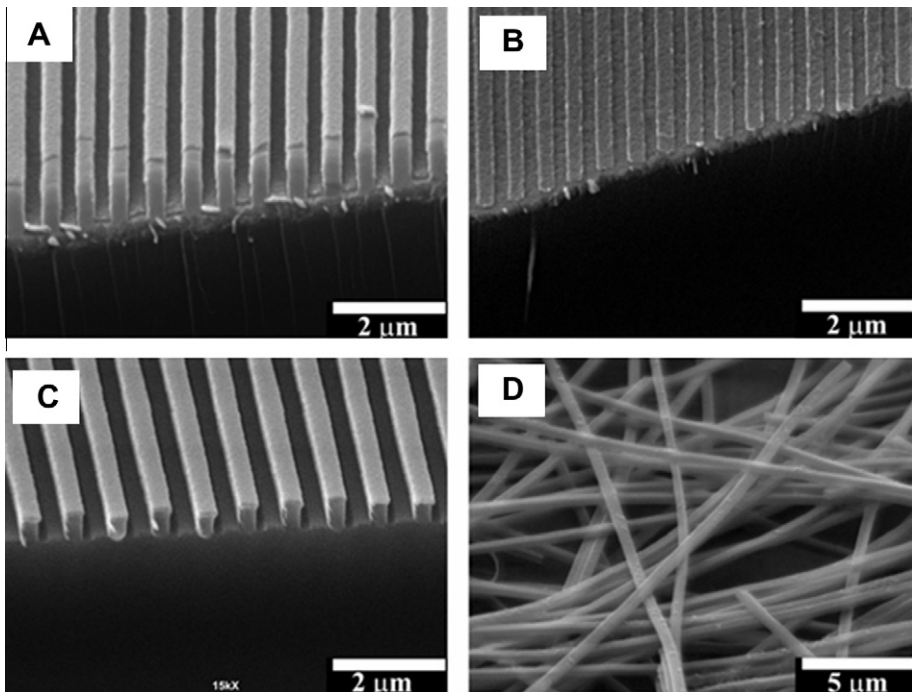


**Fig. 22.** (A) SEM image of 50 nm Al deposited at normal incidence on 250 nm wide, (B) Al wires of width 250 nm and 50 nm thick on indium tin oxide glass substrate, (C) 100 nm Ti deposited with 15° tilted angle from normal direction, and (D) Curled Ti nanoribbons collected by dispensing a few drops of IPA containing nanoribbons on a flat substrate. Reprinted from Ref. [35] with permission of IOP Publishing Ltd.

and curved as compared to their configuration during growth. Fig. 22A shows the SEM image of 50 nm Al deposited at normal incidence on 250 nm wide photoresist bars with 550 nm period. Fig. 22B shows the Al wires of width 250 nm and 50 nm thick on indium tin oxide glass substrate after removal of photoresist. Fig. 22C shows 100 nm Ti deposited with 15° tilted from the normal direction. Curled nanoribbons as shown in Fig. 22D are collected by dispensing a few drops of IPA containing nanoribbons on a flat substrate and vacuum-assisted drying. They also found that the dimensions of the nano-wires can be controlled by adjustment of deposition conditions and polymer templates. Long nanowires and nanoribbons were made with this method.

Liu et al. [176] used a hot plasma (such as hydrogen arc discharge) method to prepare the double-walled carbon nanotubes (DWNTs) with high thermal stability. In a synthesis of DWNTs, first a cylinder-shaped reactor chamber with a diameter of 600 mm and height of 400 mm was used. The anode and cathode were made of graphite rod and big rotatable graphite cylinder with eight holes. A rotatable graphite cylinder was filled with the mixture of catalyst precursors, sulfide and carbon feedstock. The distance between the two electrodes is ~4 mm. The electric arc was operated in a dc mode at 120–300 A and a hydrogen atmosphere of 32 kPa pressure. Their results indicated that the arc current and molar content of nickel formate dihydrate are influenced on the growth of DWNTs. Another feature of hydrogen arc discharge is that the diameter distribution (1.98–3.47 nm) of the DWNTs is much narrower than those (usually 1.5–5.5 nm) reported using conventional arc discharge technique.

Ha et al. [177] synthesized high-purity DWNTs by an arc-discharge method in hydrogen ambient gas. The DWNTs were synthesized using a mixture of Fe catalyst and FeS promoter in a stainless steel chamber. The experimental setup for the synthesis of DWNTs is the same as a Liu et al. apparatus [176]. A 1 mm gap is maintained between the two electrodes to create arc plasma. Hydrogen was used as a buffer gas. Pressure and discharge current was used at various ranges from 250 to 450 Torr and 30

to 70 Å, respectively. The time period of arc-discharge process was 20 min. Finally, the purified DWNTs were collected by filtration and washed with DI-water several times. They also showed that the purified DWNTs have very good field emission properties. The emission current density of DWNTs reaches  $\sim 10$  mA cm $^{-2}$  at an applied field of  $\sim 6.5$  V  $\mu\text{m}^{-1}$ .

Peng et al. [178] used cold plasma system (rf thermal plasma system) to synthesize large quantities of zinc oxide nanorods. For zinc oxide nanorods fabrication, the starting powders of zinc, zinc oxide and basic carbonate of zinc were supplied into the plasma flame by the carrying gas in a continuous way and then underwent vaporization, crystallization, and growth processes following the flowing gas in the reactor chamber; lastly, rodlike crystals were obtained. The following synthesis conditions are applied for fabrication of zinc oxide nanorods: center gas, argon 1.0 m $^3$  h $^{-1}$  sheath gas, nitrogen 5.0 m $^3$  h $^{-1}$  carrier gas, nitrogen 150 L h $^{-1}$  oxidative gas, oxygen 0.5–50 L min $^{-1}$  powder feeding rate 10–60 g min $^{-1}$ . The final products were collected at the bottom of the collector. Hence, hot and cold plasma is worthy noting that the productivity is higher than those prepared by other methods or routes.

The spray pyrolysis synthesis method is relatively “environmentally” friendly, scalable, inexpensive, and can be applied to a variety of different substrates. Kamalakaran et al. [179] synthesized the thick and crystalline carbon nanotube arrays by spray pyrolysis. In a typical procedure, the experimental setup consists of a Pyrex nozzle attached at one end to a container used for storing and releasing ferrocene/benzene solutions. During spraying, Ar gas was used to exert the pressure on the solution in order to regulate the liquid flow directed to the nozzle. Then, a reaction tube was placed in a preheated furnace. The spraying time lasted between 5 and 15 min, depending on the volume of the reacting solution and the Ar flow rate. Finally, in order to anneal the products, the furnace was maintained at the set temperature for additional 15 min. Diameter of synthesized nanotubes is  $\sim 100$ –250 nm. Recently, Breedon et al. [180] fabricated the interconnected ZnO nanostructured arrays onto glass substrates by using a spray pyrolysis deposited ZnO seed layers as a nucleation platform for subsequent hydrothermal growth. The two steps involved in a typical synthesis of interconnected ZnO nanostructured arrays. First, the deposition of a ZnO seed layers via spray pyrolysis for the formats an angular seed layer. Second, the subsequent hydrothermal growth step by Kamalakaran et al. [179] modified the method [181]. They also reported that the growth of interconnected ZnO nanowires was influenced by the physical and crystallographic orientations of the underlying seed crystallites. For instance, sputtered seed layers resulted in fairly vertical nanorods which were  $\sim 80$  nm in width, while seed layers deposited by spray pyrolysis resulted in arrays of interconnected ZnO nanowires measuring  $\sim 15$  nm in width (Fig. 23). From above results, we can say that the spray pyrolysis method provides a facile way to synthesize one-dimensional nanostructures of ZnO and other materials.

The IGC method has several advantages such as high quality and purity due to gas phase reaction in an inert gas, and high quality crystalline structure due to particle formation in a quasi-thermal equilibrium state. Therefore, the IGC is a useful technique for fabricating 1D NSMs. Recently, Al-Sharab et al. [182] synthesized the tungsten oxide (WO<sub>2.9</sub>) nanofibers via IGC process. In IGC, the powder is evaporated in a low-pressure vacuum chamber, and the vaporized species are collected on a water-cooled chill substrate. Nanofibers are deposited at different positions on the chill substrate, whereas elongated nanofibers are prevalent on sections of the chill substrate nearest to the evaporative source. The length and diameter of fibers are  $\sim 400$  nm and  $\sim 30$  nm, respectively. In some cases, small twins are observed in fibers with diameters  $>25$  nm. To summarize the results given, we can say that the IGC technique is an efficient method to fabricate the 1D NSMs. Pulse laser ablation is also a simple method and has been widely used for the synthesis of 1D NSMs such as nanowires and nanotubes. Hu et al. have used the simple laser ablation method to fabricate the 1D  $\beta$ -Ga<sub>2</sub>O<sub>3</sub> nanowires [183]. To fabricate  $\beta$ -Ga<sub>2</sub>O<sub>3</sub> nanowires, first a Ga<sub>2</sub>O<sub>3</sub> target was located at the center of the quartz tube, and an alumina substrate was placed downstream of the target. The quartz tube was located inside the furnace. Then, the system was evacuated by a rotary pump to create a pressure of  $\sim 3 \times 10^{-2}$  Torr. Further, carrier gas of high-purity (Ar + 5% hydrogen) was kept flowing through the tube at a rate of 50 sccm and a pressure of 350 Torr in the tube. The beam of a KrF excimer laser with a wavelength of 248 nm and a repetition rate of 10 Hz was then used to ablate the target at 800 °C temperature. The laser power was 350 mJ per pulse with pulse duration of 34 ns. The laser spot size on the target is  $\sim 1 \times 3$  mm $^2$ . The total time of the ablation was 5 h. The temperature, pressure, and the carrier gas

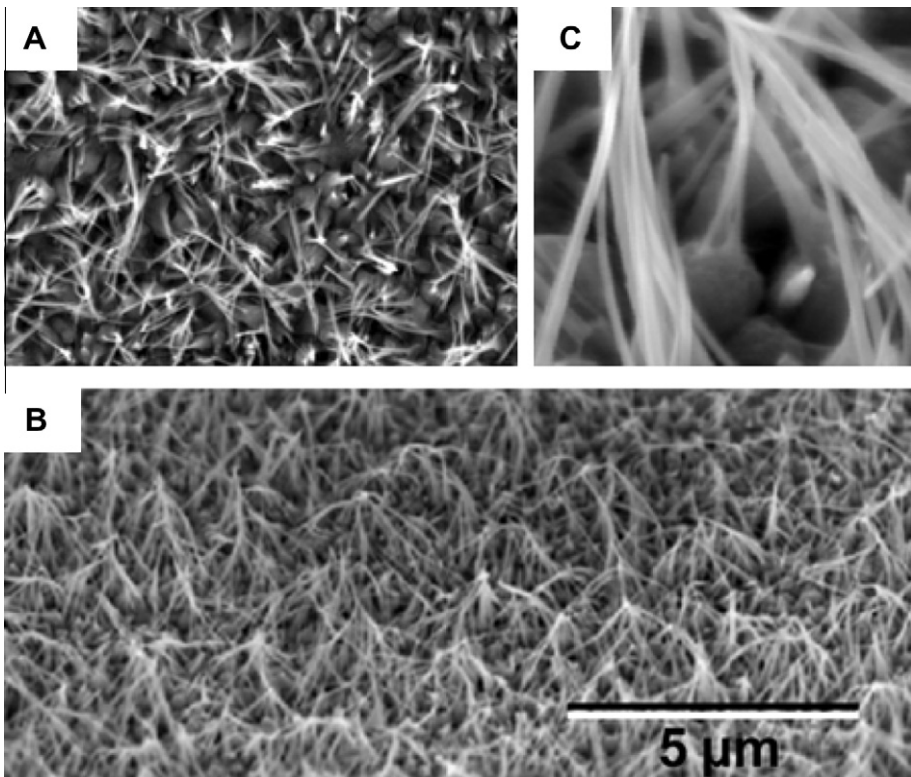


**Fig. 23.** SEM images of an interconnected ZnO nanowire: (A) plan-view, (B) at 45° rotation, and (C) high-magnification SEM picture of the nanowires bundled along their non-polar facets. Reprinted from Ref. [180] with permission of Elsevier.

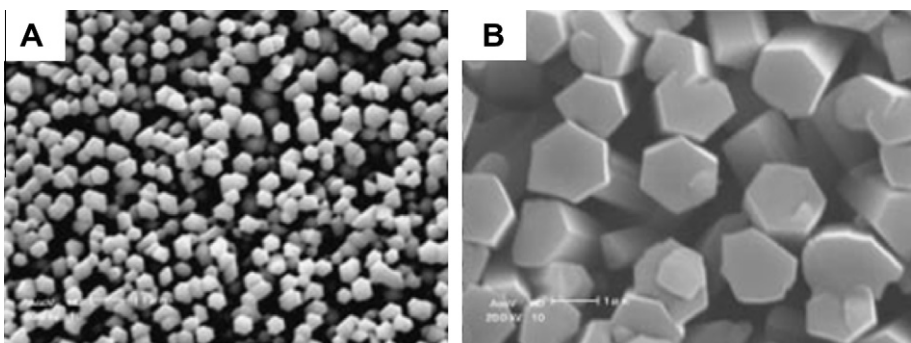


**Fig. 24.** SEM pictures of ZnO nanorods on sapphire substrate (A) and SiO<sub>2</sub> substrate (B) heated to 700 °C. O<sub>2</sub> gas pressure was ~5 Torr. Reprinted from Ref. [32] with permission of Japan Society of Applied Physics.

flow rate were kept constant during the ablation process. After ablation, the furnace was cooled to room temperature; the resulting products were collected from the alumina substrate. The as-synthesized nanowires have diameters of 15–50 nm and lengths up to several micrometers. Later Okada et al. [32] also used the pulse laser ablation to fabricate the ZnO nanorods in the presence of He and O<sub>2</sub> gas. In their typical experiment, a pure metal Zn target was ablated using a KrF excimer laser with a fluence

of  $\sim 3 \text{ J cm}^{-2}$  at a pulse frequency of 20 Hz. Large quantities of ZnO nanorods are synthesized at a higher gas pressure and temperature on a sapphire or a  $\text{SiO}_2$  substrate. Fig. 24A and B shows the SEM images of ZnO nanorods on a sapphire and  $\text{SiO}_2$  substrate. ZnO nanorods with a size in the range from 200 to 300 nm, which had a hexagonal pyramidal top surface, were grown. On the other hand, in case of  $\text{SiO}_2$  substrate, hexagonal ZnO nanorods with a size of  $\sim 1 \text{ mm}$  were grown.

The sonochemical method has been widely explored to generate 1D NSMs such as nanorods and nanotubes [184]. For example, Xiu et al. [185] fabricated the PbS nanorods via sonochemical method in the presence of PEG (polyethylene glycol-6000). For the synthesis of PbS nanorods, first 0.01 mol -lead nitrate, 0.015 mol thioacetamide and 2 g polyethylene glycol-6000 were mixed in 80 mL DI water. The sonication was then conducted without cooling so that a temperature of about 343 K was reached at the end of the reaction. The obtained products were filtered, washed several times with DI water and ethanol and subsequently vacuum dried at 80 °C for 3 h. The diameters and lengths of synthesized PbS nanorods are 20–60 nm and 1–2  $\mu\text{m}$ , respectively. They also noticed that PEG and sonication time playss a key role in the formation of PbS nanorods. Recently, Guo et al. [186] fabricated the mesoporous  $\text{TiO}_2$  nanorods via a sonochemical route. Typical synthesis of mesoporous  $\text{TiO}_2$  nanorods was carried out at normal atmospheric pressure and relatively low temperature of 70 °C. First, 0.5 g bulk Ti powder was mixed into a 250 mL beaker with 100 mL 10 M NaOH aqueous solution. After sonicating for 24 h, the precipitate was washed to neutral by DI water, and poured in 0.1 M  $\text{HNO}_3$  aqueous solution for 24 h, then washed by DI water and ethanol. Finally, the precipitate was dried in an oven at 80 °C for 12 h, further annealing at 450 °C in air for 1 h to get the final product. Fig. 25 shows the SEM and TEM images of resulting products. As shown in SEM and TEM images, the width and length of nanorods are 8–12 nm and 15–100 nm, respectively. High-resolution trans-

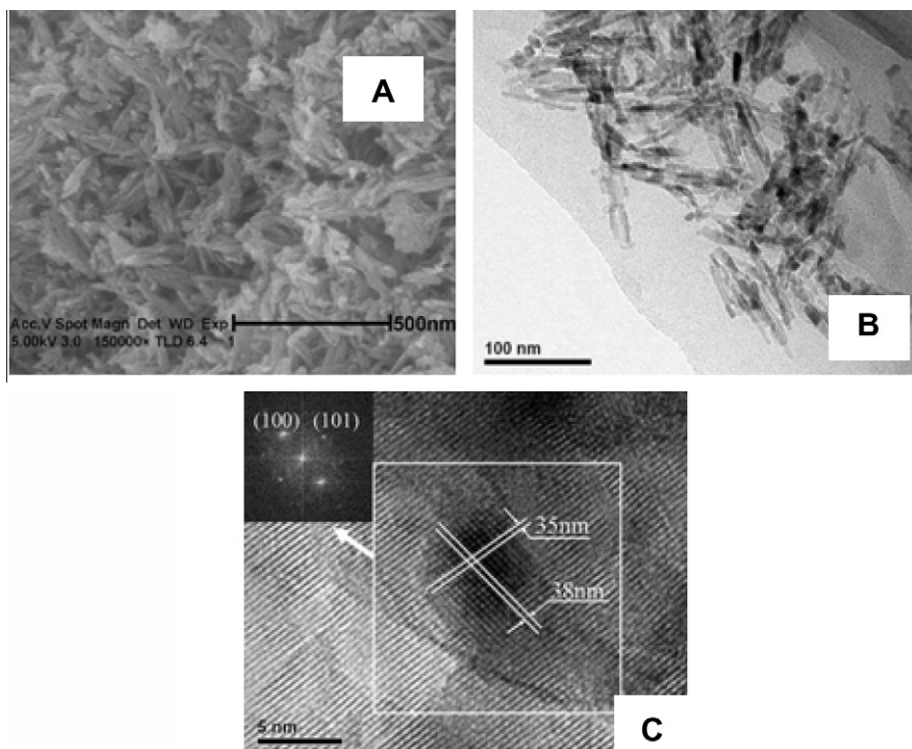


**Fig. 25.** (A) SEM image and (B) TEM image of  $\text{TiO}_2$  nanorods. (C) HRTEM image of  $\text{TiO}_2$  nanorods; inset show the FFT of the selected-area marked in the HR image. Reprinted from Ref. [186] with permission of Elsevier.

mission electron microscope (HRTEM) image suggests the development of a well-defined crystalline structure of  $\text{TiO}_2$  nanorods. The spacing of the lattice fringes is found to be  $\sim 0.35$  and  $\sim 0.38$  nm, respectively. The fast Fourier transform (FFT) pattern (inset Fig. 25C) can be indexed to the (101) and (100) diffraction planes of the hexagonal structure of anatase.

Consequently, we can say that the physical approach provides significantly more flexibility in processing to allow the preparation of 1D NSMs.

#### 4.2.2. Synthesis of 1D NSMs by chemical processes

LLC template-assisted synthesis is one of the most facile and most applied methods for the synthesis of 1D NSMs such as nanowires, nanorods, nanotubes, nanobelts, nanoribbons, and nanospindles [187–191]. For instance, Huang et al. [31] used the LLC template-electrodeposition to fabricate the  $\text{Cu}_2\text{O}$  nanowires with diameter of 25–100 nm. The two steps involved in the fabrication of the Ag nanowires. First, they prepared the reverse hexagonal liquid crystalline phase. To prepare the liquid crystal, AOT was dissolved in *p*-xylene. To this solution, 0.1 M  $\text{CuCl}_2$  aqueous solutions were added drop-wise with stirring. The mixture was stirred for 1 h to give a clear viscous liquid at room temperature. In second step, they formed the  $\text{CuO}_2$  nanowire via electrodeposition. During electrodeposition, constant potential of  $-1.1$  V was applied across the two electrodes for a period of time with a current density of  $200\text{--}400 \mu\text{A cm}^{-2}$ . After electrodeposition, the nanowire deposit on the substrate was thoroughly washed with ethanol to remove the LLC phase. The diameter and length of nanowires increases with decreasing time.

Later, Kijima et al. [191] fabricated the platinum, palladium, and silver nanotubes, with inner diameters of 3–4 nm and outer diameters of 6–7 nm, by the reduction of metal salts confined to lyotropic mixed LCs of two different sized surfactants. In a typical synthesis process, the liquid crystalline phase of hexachloroplatinic acid, nonaethylene glycol monododecyl ether, polyoxyethylene (20) sorbitan monostearate and  $\text{H}_2\text{O}$  is at a molar ratio of 1:1:1:60. Next, an excess amount of hydrazine was added to the cooled pasty material and then kept at that temperature for 24 h. The resulting product was separated, washed with DI water and ethanol prior to drying in air. Similar syntheses by using  $\text{Pd}(\text{NO}_3)_2$ , or  $\text{AgNO}_3$ , and SDS, in place of  $\text{H}_2\text{PtCl}_6$  and  $\text{C}_{12}\text{EO}_9$  were carried out to achieve palladium and silver nanotubes. It is well known that the uniform and consistently sized metal nanotubes are promising for potential applications as electrodes in batteries and fuel cells, and environmental catalysts. From above results we can say that the LLC template-assisted methods are fast, inexpensive, reproducible, and potentially versatile for the fabrication of 1D NSMs.

Electrodeposition processes have a wide range of advantages such as low cost, environmentally friendly, low energy consumption, high growth rate at relatively low temperatures and good control of the deposition thickness, shape and size. Basically, there are two ways to produce the 1D NSMs through the electrodeposition method. First is the template-assisted electrodeposition, where the 1D anisotropic growth is realized by using various templates to confine the growth space of the electrodeposits. For example, recently several groups are applying the template method pattern to fabricate the 1D NSMs such as nanotubes, nanowires and nanorods [192–195]. More recently, Xia et al. [33] fabricate the  $\text{MnO}_2$  nanotube and nanowire arrays via an electrochemical deposition technique using porous alumina templates. In a typical synthesis of  $\text{MnO}_2$  nanotube and nanowire arrays, a solution with 0.1 mole manganese sulfate and 0.1 mole sodium sulfate was used as the electrolyte. Anodic aluminum oxide (AAO) membranes were used as the templates. To prepare the working electrode, a thin layer of Pt was sputtered on one side of the alumina membrane using a sputter system. The electrochemical system is consisted of a working electrode, a carbon rod counter electrode, and an  $\text{Ag}/\text{AgCl}$  reference electrode. Electrochemical deposition of  $\text{MnO}_2$  was carried out by galvanostatic technique (current density =  $2 \text{ mA cm}^{-2}$ ). A period of 10 min and 60 min was used for synthesis of  $\text{MnO}_2$  nanotube and nanowire arrays. After electrochemical deposition, the samples were dipped in a 1 M KOH solution overnight to remove the AAO template. Fig. 26 shows the SEM pictures of  $\text{MnO}_2$  nanotube arrays and  $\text{MnO}_2$  nanowire arrays after removal of the template. The cross-sectional view of  $\text{MnO}_2$  nanotubes shows that the length of nanotube is  $\sim 2 \mu\text{m}$ , as shown in Fig. 26C. The morphology of the nanotubular nanostructure changes to a wire-like form during prolonged electrochemical deposition (Fig. 26D and E). The cross-sectional view of the  $\text{MnO}_2$  nanowire arrays show that the length

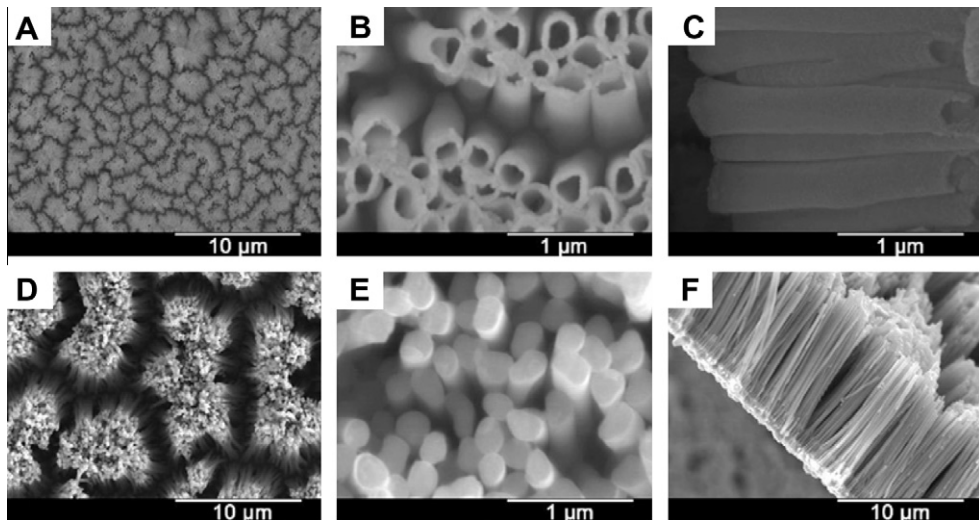


**Fig. 26.** (A and B) plan-view SEM images of MnO<sub>2</sub> nanotube arrays; (C) cross-section view of MnO<sub>2</sub> nanotube arrays; (D and E) plan-view SEM images of MnO<sub>2</sub> nanowire arrays; (F) cross-section view of MnO<sub>2</sub> nanowire arrays. Reprinted from Ref. [33] with permission of Elsevier.

of MnO<sub>2</sub> nanowire is ~10 μm (Fig. 26F). They also report that the MnO<sub>2</sub> nanotube array electrode has a superior capacitive behavior to that of the MnO<sub>2</sub> nanowire array.

The second method is by using template-free electrodeposition, where the 1D anisotropic growth is achieved by utilizing the intrinsic anisotropic crystallographic structure of a targeted material [34,196]. However, only a few 1D NSMs have been made by the template-free electrodeposition. More recently, Li et al. [34] used the electrodeposition process to fabricate the polyaniline nanobelts. In a typical synthesis of polyaniline nanobelts, first, 0.1 mole aniline was used as the electrolyte. Then the electrodeposition of polyaniline nanobelts were carried out by HDV-7C transistor potentiostatic apparatus connected to a three-electrode electrochemical cell system. The three-electrode electrochemical system contains Ti sheet as a working electrode, graphite rod as the counter electrode, and a saturated calomel electrode as the reference electrode that was connected to the cell with a double salt bridge system. The electrodeposition was carried out by galvanostatic method with cathodic

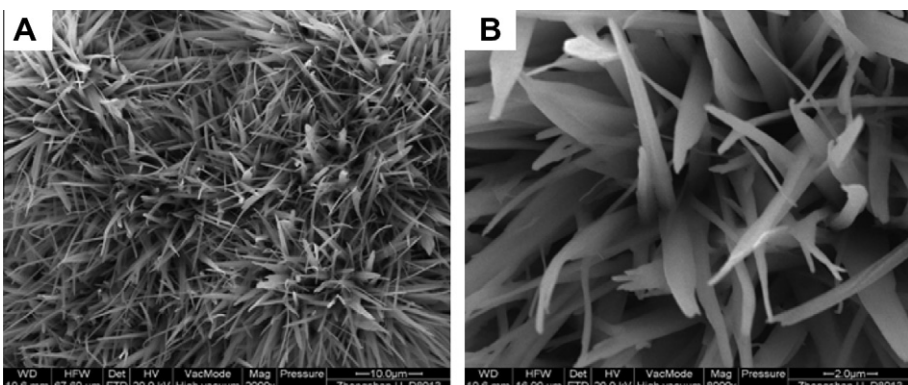


**Fig. 27.** Typical (A) low- and (B) high-magnification plan-view SEM images of polyaniline nanobelts. Reprinted from Ref. [34] with permission of ACS Publishers.

current density of  $1.0 \text{ mA cm}^{-2}$  for 12 h at  $70^\circ\text{C}$ . Fig. 27 shows the SEM images of the resulting products. The average width and thickness of polyaniline nanobelts are  $\sim 2 \mu\text{m}$  and  $\sim 50 \text{ nm}$ , respectively. The length of polyaniline nanobelts is  $\sim 20 \mu\text{m}$ . They also had shown that the polyaniline nanobelts have a high specific capacitance value of  $873 \text{ F g}^{-1}$  at  $10 \text{ mV s}^{-1}$ , which is much bigger than that of polyaniline nanospheres.

Similar to electrodeposition process, the electroless deposition technique is also used for the synthesis of the 1D NSMs [197–200]. For example, Muench et al. [199] fabricated the Au nanotubes by electroless deposition in the presence of powerful reagent. For the synthesis of Au nanotubes, 4-(dimethylamino) pyridine (DMAP) was used to adjust the electroless deposition by interfering with the auto-catalytically active Au surface. The pH value and DMAP concentration are adjusted to produce the wide range of products. Fig. 28 shows SEM images of Au nanostructures obtained after addition of various DMAP concentrations at pH 9.9 (A, 0 mM; B, 42 mM; C, 89 mM; D, 130 mM). Each inset is the magnified image of Au nanostructures. Filigree nanotubes of  $10\text{--}15 \text{ nm}$  wall thickness and  $5.0 \pm 2.1 \text{ nm}$  grain sizes were obtained. The robust and self-standing structures prove homogeneous deposition along the whole template (length of template is  $\sim 30 \mu\text{m}$ ).

Vasquez et al. [200] also used the electroless deposition method to fabricate the polygonal rings and microwires of covellite-type CuS. The kinked polygonal microwires and serpentines 250–350 nm in diameter and tens of microns in length were formed. The resulting products were hexagonal type CuS or covellite, which is confirmed by X-ray diffraction (XRD) and selected area electron diffraction (SAED). They have also given the brief mechanisms of formation of different structures. According to their mechanism, first the localized nucleation of CuS spheres take place at the tips of the pillars selectively wetted by the crystallization solution, followed by the fusion of the particles into chains connected to the micropillars. Finally, release of the chains from the posts upon growth and their reconnection with the chains emerging from the neighboring pillars. From the above results, we can say that the electroless plating is also a promising method for forming uniform 1D NSMs.

The hydrothermal technique is an efficient method for the controlled synthesis of 1D NSMs [201–204]. For instance, Tang et al. [203] prepared the Si nanowires on Si substrates by hydrothermal depo-

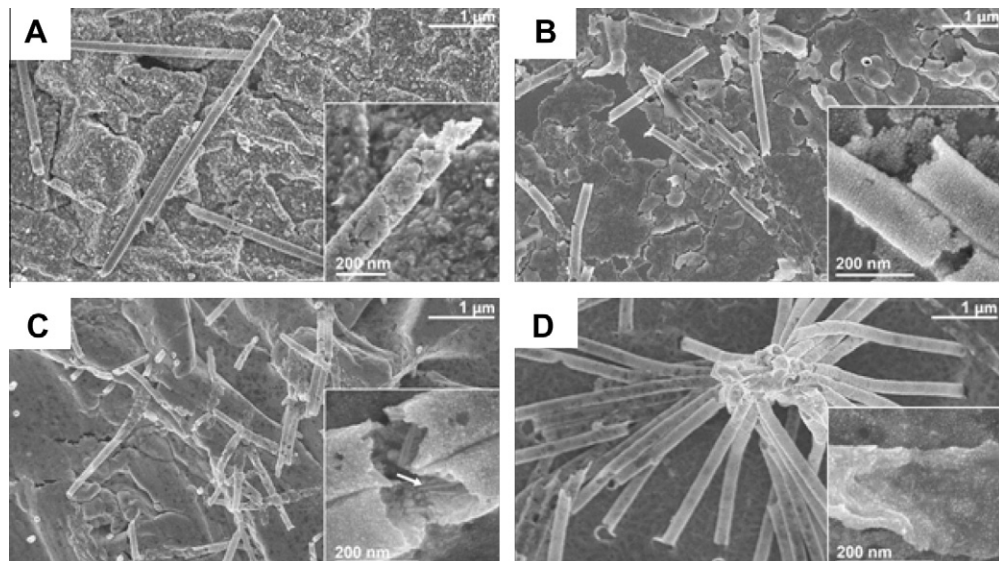


**Fig. 28.** Typical SEM images of Au nanostructures obtained after addition of various DMAP concentrations at pH 9.9 (A, 0 mM; B, 42 mM; C, 89 mM; D, 130 mM). Each inset is the magnified Au wires (A), tubes (B and C), or collapsed tubes (D). The arrow mark on the part C indicates the anisotropic crystals grown on top of the surface Au film inside broken tubes. Reprinted from Ref. [199] with permission of ACS Publishers.

sition route under low temperature and pressure. The obtained Si nanowire consists of a polycrystalline Si core and an amorphous silica sheath. The diameter and length of Si nanowires were  $\sim 170$  nm and  $\sim 10$   $\mu\text{m}$ , respectively. More recently Shim et al. [204] used the facile hydrothermal method with hydrogen titanate nanowires as the precursor to fabricate the porous  $\text{TiO}_2$  nanowires. In a typical synthesis of porous  $\text{TiO}_2$  nanowires, first, 0.1 g of anatase powder was well dispersed in a 10 mol  $\text{L}^{-1}$  NaOH solution, and then the mixed solution was transferred into a stainless steel autoclave (temperature maintained for 48 h at 200  $^{\circ}\text{C}$ ). After the hydrothermal treatment and centrifuged, a white sodium titanate precipitate was obtained. Next, the prepared precipitate was soaked in a 0.1 mol  $\text{L}^{-1}$  HCl solution for 24 h, which fully induced cation exchange between  $\text{Na}^+$  and  $\text{H}^+$  ions. Hydrogen titanate nanowires were washed with DI water several times. To obtain the pure anatase phase  $\text{TiO}_2$  nanowires, the hydrogen titanate nanowires were treated by hydrothermal method with DI water at 180  $^{\circ}\text{C}$  for 3 h along with centrifugation and washing steps. Fig. 29 shows the SEM, TEM, HRTEM images and SAED pattern of the pure anatase phase  $\text{TiO}_2$  nanowires and an anatase  $\text{TiO}_2$  nanowire. They also reported that the porous anatase  $\text{TiO}_2$  nanowires demonstrated a good cycling performance and excellent rate capabilities compared with the  $\text{H}_2\text{Ti}_3\text{O}_7$  nanowires and the anatase  $\text{TiO}_2$  nanowires.

Solvothermal reaction utilizes a solvent under elevated pressures and temperatures above its critical point to increase the solubility of a solid and to speed up reactions between precursors. In view of several advantages (high purity and good homogeneity) over other techniques, the solvothermal synthesis process has been one of the most important methods for the preparation of 1D NSMs [205–209]. Xu et al. [208] fabricated large scale  $\text{CdS}$  nanowires by a solvothermal process in a mixed solvent of dodecanethiol and ethylenediamine. In a typical synthesis of  $\text{CdS}$  nanowires, first 1 mM  $\text{Cd}(\text{OAc})_2 \cdot 2\text{H}_2\text{O}^{-2}$  and 2 mM  $\text{Na}_2\text{CNEt}_2 \cdot 3\text{H}_2\text{O}$  was poured into a mixed solvent of ethylenediamine and dodecanethiol. The resulting mixture was then transferred into a stainless autoclave. The autoclave was sealed and kept for 18 h at 180  $^{\circ}\text{C}$ . After that, autoclave was cooled to room temperature.

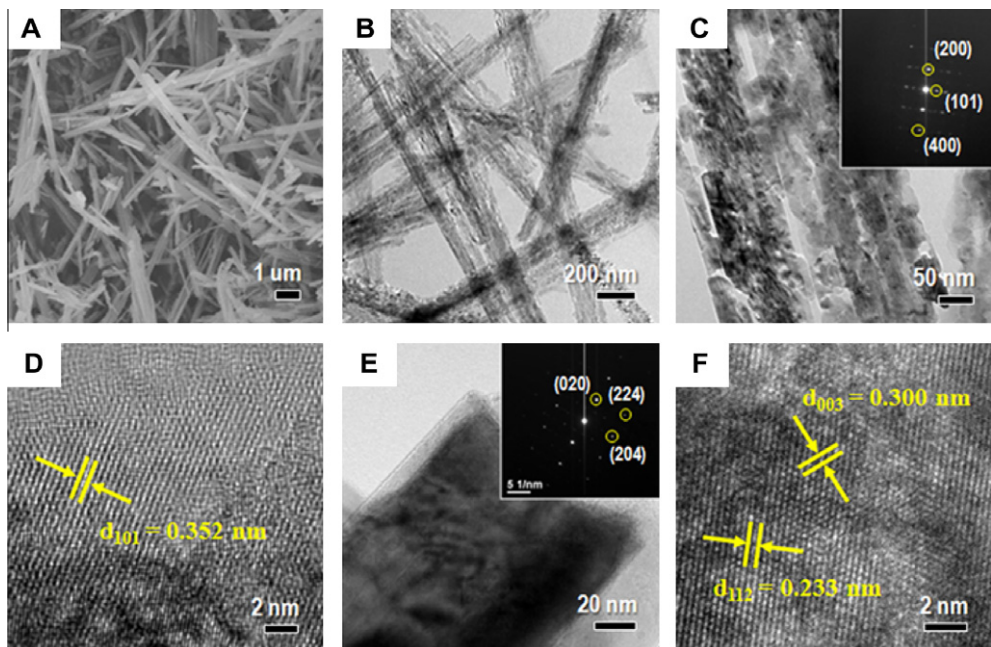


**Fig. 29.** (A) SEM and (B) TEM images of the as-made pure anatase phase  $\text{TiO}_2$  nanowires growth by hydrothermally dehydrated at 180  $^{\circ}\text{C}$ . (C) HRTEM image of the pure anatase phase  $\text{TiO}_2$  nanowires with porous nanostructures. The inset of image C shows the SAED patterns. (D) HRTEM image of a pure anatase phase  $\text{TiO}_2$  nanowire. (E) TEM image of an anatase  $\text{TiO}_2$  nanowire. The inset of image E shows the SAED patterns. (F) HRTEM image of an anatase  $\text{TiO}_2$  nanowire. Reprinted from Ref. [204] with permission of IOP Publishing Ltd.

The product was carefully washed with DI water and ethanol, and then dried in a vacuum for 4 h at 50 °C. Fig. 30 shows the SEM images of the resulting products. The resulting product is composed of uniform nanowires with an average diameter of ~25 nm and lengths of 20–40 μm.

In the same year, Sun et al. [209] also used the same method to fabricate the pure phase CeO<sub>2</sub> nanorods. In a typical synthesis of pure phase CeO<sub>2</sub> nanorods, first 0.01 M octadecylamine was dissolved into a solution containing 40 mL DI water and 40 mL ethanol. 0.01 M of hydrated cerium(III) chloride was added under magnetic stirring after the octadecylamine was completely dissolved. After 3 h stirring, the mixture was transferred into an autoclave. Then the autoclave was sealed and maintained in an electric oven at 160 °C for 72 h. After that, autoclave was cooled to room temperature. Finally, the product was washed with acetone, hot ethanol solution and DI water in sequence several times, and then separated by centrifugation. To obtain the pure phase CeO<sub>2</sub> nanorods, the product was dried in a vacuum oven and then calcined with a muffle oven at 400 °C in air. The pure phase CeO<sub>2</sub> is composed of uniform nanorods with a diameter of ~40–50 nm and lengths of 0.3–2 μm. They also reported that the solvent composition, surfactant type, cerium source precursors, temperature and reaction time played a major role in the formation and growth of CeO<sub>2</sub> nanorods. Thus, we can say that the solvothermal process is a very useful method to make the 1D NSMs.

The sol-gel technique is an attractive synthetic method due to its simplicity and flexibility which allow for optimization and production of bulk 1D NSMs [210–213]. Chaudhuri et al. [212] prepared the silicon nitride nanowires by carbothermal reduction followed by the nitridation (CTRN) of silica gel containing ultrafine excess carbon obtained by the decomposition of dextrose over the temperature range of 1200–1350 °C. Their method involves repeated evacuation followed by purging of N<sub>2</sub> gas so that the interconnected nanopores of the gel are filled with N<sub>2</sub> gas prior to heat treatment. The presence of N<sub>2</sub> gas in the nanopores of the gel starts the CTRN reaction simultaneously throughout the bulk of the gel. In results, the chemical reaction is leading to the formation of silicon nitride nanowires. The diameter and length of silicon nitride nanowires are ~500 nm and 0.2 mm, respectively. Later, Bitenc et al. [213] prepared the ZnO particles with a needle-like shape by solution-phase method in the autoclave system (oven preheated at 90 °C). In a typical synthesis of hexagonal ZnO, first water (W) and ethylene glycol (EG) with 0.001 M Zn<sup>2+</sup> + 0.005 M urea are mixed for 72 h (Sample A: volume ratio W/EG = 1/3 and Sample B: W/EG = 1/1). After 24 h the Sample C was prepared by mixture of 0.01 M Zn<sup>2+</sup> + 0.05 M urea with a volume ratio W/EG = 1/3. The resulting products were cooled to room temperature, filtered off, washed with DI water, and dried in air. By changing the ratio of W/EG, the concentration of the starting chemicals and the reaction conditions, it is possible to control the structure and morphology of ZnO particles. Fig. 31 shows SEM images of the three samples (Samples A–C). As shown in SEM images, the ZnO particles that were prepared in the autoclave had a much higher aspect ratio ( $20 \pm 5$ ) and were needle-like. Hence, the sol-gel method can be applied for the preparation of various types 1D NSMs.

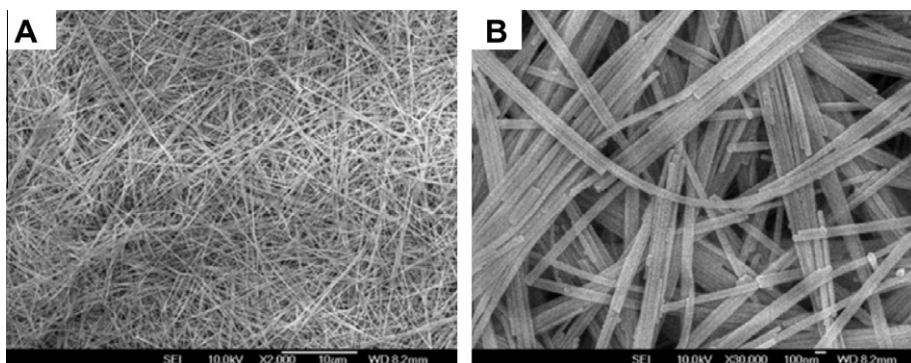


**Fig. 30.** (A) Low- and (B) high-magnification SEM pictures of the CdS nanowires. Reprinted from Ref. [208] with permission of ACS Publishers.

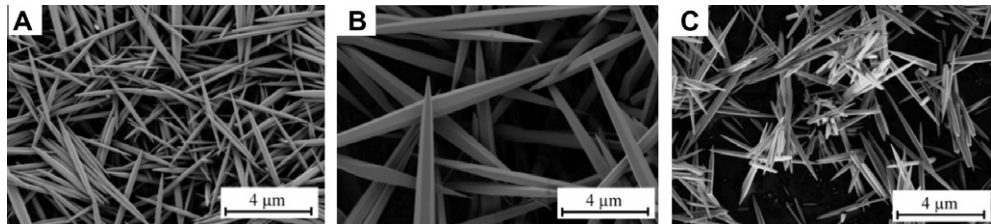


**Fig. 31.** SEM images of three samples (A–C) prepared in an autoclave at 90 °C. Reprinted from Ref. [213] with permission of ACS Publishers.

In the last few years, nanowires formation via CVD is especially attractive because of the relative ease of scaling from research to production-size systems [214–218]. Shimizu et al. [217] used the CVD to fabricate the Ge nanowires on Si substrates. In a typical synthesis of Ge nanowires, first *n*-butylgermane was used as source gas in consideration of the following properties: substantially less hazardous and less toxic compared to GeH<sub>4</sub>, facile to handle liquid with acceptable vapor pressures, and better thermal stability. Au was used as catalyst for vapor liquid solid (VLS) growth of Ge nanowires. Fig. 32 shows plan-view SEM images of Ge nanowires grown on the Si substrate. The (110) growth direction is dominant in Fig. 32A–C. The average diameter of the Ge nanowires calculated from Fig. 32C was ~20 nm. Qi et al. [218] reported a synthesis of Si nanowires by multitemperature zone chemical vapor deposition reactor. A typical synthesis of Si nanowires was carried out at temperatures as low as 290 °C. The low-temperature process is facilitated by the independent control over the precursor feeding and the nanowire growth, which leads to a balanced VLS or vapor–solid–solid (VSS)

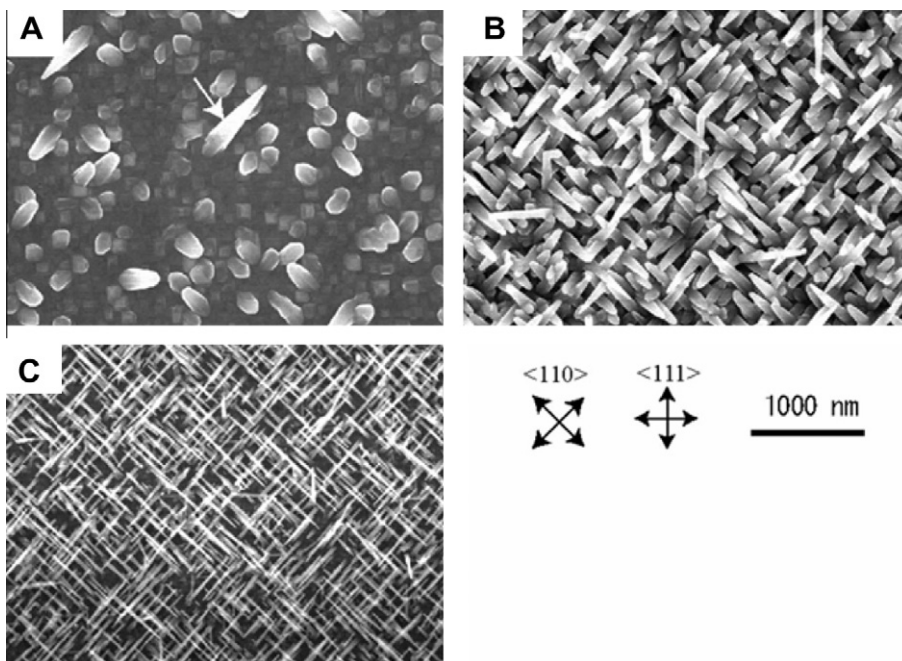


**Fig. 32.** Plan-view SEM images of Ge nanowires. The Ge nanowires were grown at various temperature (A) 450, (B) 400, and (C) 370 °C for duration of four min in *n*-butylgermane. The arrow in (A) indicates a strongly tapered wire. Crossed arrows represent crystal orientations of the Si (100) surface. Reprinted from Ref. [217] with permission of ACS Publishers.

growth. From above results, we found that the CVD is one of the best techniques to prepare high-quality 1D NSMs.

1D NSMs have also been synthesized via a LCVD [219–224]. Longtin et al. [223] reported the growth of carbon nanofibers on nickel coated alumina substrates by the LCVD. In a typical growth of carbon nanofibers, first Ni coated alumina substrate was put in a cylindrical stainless steel cold-wall reactor at an angle or perpendicularly to the laser beam. Next, ethylene was injected into the vessel at a pressure of 100 kPa. A Coherent Innova 90 continuous Ar ion laser was used to generate the laser beam. A lens located outside the vessel was used to defocus the beam to a spot size of 4.3 mm. The power density ranged from  $0.2 \times 10^5 \text{ W m}^{-2}$  to  $2.1 \times 10^5 \text{ W m}^{-2}$ . Fig. 33 indicates the change in the surface morphology of carbon nanofibers with respects to various irradiation times. Longer irradiation times produced a 1 μm thick carbon coating over most of the irradiated area, as shown in Fig. 33. In addition, they found that the quality of films can be optimized by controlling the experimental parameters such as irradiation time and power density. Later, Morjan et al. [224] also used the LCVD to fabricate the carbon nanotubes on a Si(100) substrate. There are two aspects of the large scale fabrication of carbon nanotubes. The first step is to prepare the substrate by depositing the catalyst nanomaterial. The second one is the synthesis of carbon nanotubes by LCVD. Similar to previous results, the purity and growth of carbon nanotubes are controlled by CO<sub>2</sub> laser irradiation and varying ethylene concentration in the ethylene/acetylene precursor mixture.

Laser pyrolysis is an important method for producing special 1D NSMs with different shapes and sizes [225,226]. Alexandrescu et al. [226] fabricated the rod-like shape TiO<sub>2</sub> particles by the IR laser pyrolysis technique in the presence of TiCl<sub>4</sub>, air and nitrous oxide, at lower air flows (e.g. 10 sccm

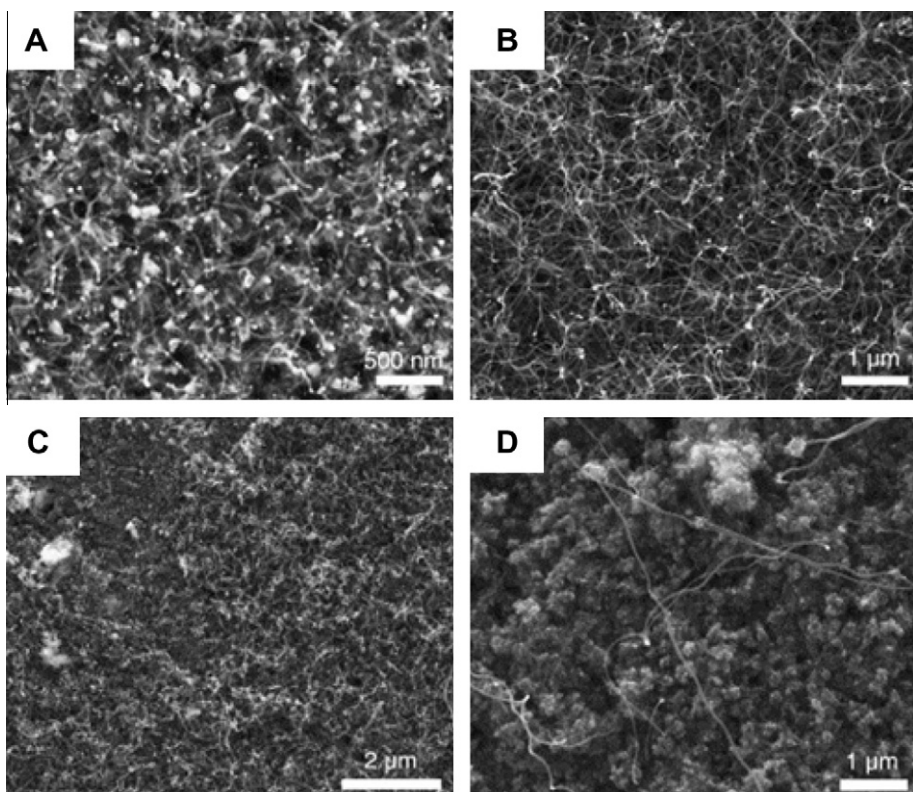


**Fig. 33.** Changes in the carbon nanofibers morphology with respect to various irradiation times: (A) 5 s; (B) 120 s; (C) 180 s; (D) 420 s. Reprinted from Ref. [223] with permission of Elsevier.

for sample S<sub>N</sub>). Fig. 34 shows the HRTEM image of an isolated S<sub>N</sub> primary nanocrystal. The length of rod-like shape TiO<sub>2</sub> particles are ~25 nm. The HRTEM image also shows the spacing of ~0.352 nm corresponding to the (101) facet. Although there are great progresses in synthesis of 1D NSMs by laser pyrolysis, there still requires a more research and development in terms of high production of 1D NSMs.

#### 4.3. Synthesis of 2D NSMs

##### 4.3.1. Synthesis of 2D NSMs by physical processes

2D NSMs such as nanoprisms, nanoplates, nanosheets, nanowalls, nanodisks, and junctions (continuous islands) are currently the focus of much attention because of their special properties, for instance small size and large surface-to-volume ratio, compared with the 1D NSMs. Physical methods have been widely used to create 2D NSMs such as nanoprisms, hierarchical, nanoplates, nanosheets, nanowalls, and nanodisks [227–233]. Dai et al. [227] fabricated the SnO nanodisks/alumina plates by thermal evaporation under controlled conditions. In a typical synthesis of SnO nanodisks, first the SnO or SnO<sub>2</sub> powders (purity of 99.9%, metals basis) were placed in an Al<sub>2</sub>O<sub>3</sub> boat located inside a quartz tube reactor as evaporation source. Alumina plates as a substrate were then placed downstream one-by-one. Next, while evacuating the alumina tube to  $\sim 2 \times 10^{-3}$  Torr, thermal evaporation was conducted at 1070 °C for SnO powders or 1350 °C for SnO<sub>2</sub> powders for 2 h under the conditions of a pressure of 500–600 Torr and an Ar carrier gas of 50 sccm. The tin oxide nanodisks were collected, where the temperature was in the range of 200–400 °C. They also obtained similar product at the same temperature zone whether the source material was SnO or SnO<sub>2</sub>. Dai et al. [228] used the same technique to fabricate the flat nanosheets of Ga<sub>2</sub>O<sub>3</sub>. The Ga<sub>2</sub>O<sub>3</sub> nanosheets have been synthesized by evaporating GaN at high temperature in the presence of oxygen. They showed that the structurally uniform, single crystalline, free from dislocations and pure Ga<sub>2</sub>O<sub>3</sub> nanosheets was synthesized. More recently, He et al. [229] fabricated the 2D arrays of gold nanoparticles through thermal evaporation of self-assembled 2D DNA nanoarrays (as a template). During this process, Au atoms/clusters (the ink material) are thermally evaporated onto self-assembled DNA nanostructures and assembled into nanoscale gold particles. The Au nanoparticles superstructure is determined by the geometry of the DNA template. In this technique, DNA molecules are not conjugated to AuNPs that have been prepared in advance; instead, they serve as inert physical substrates for *in situ* AuNP synthesis. Fig. 35 shows the TEM of tetragonal and hexagonal DNA arrays composed of symmetric four-pointed- and three-pointed-star motifs, respectively.

Normally, it is very difficult to synthesize the 2D NSMs by direct sputtering technique. Therefore, researchers fabricate 2D NSMs by an appropriate combination of lithography and sputtering technique [230,231]. Liu et al. [230] fabricated 2D ordered arrays of hollow metal nanoshells, based on a combination of nanosphere lithography and physical sputtering technique. In their experiment, first, a

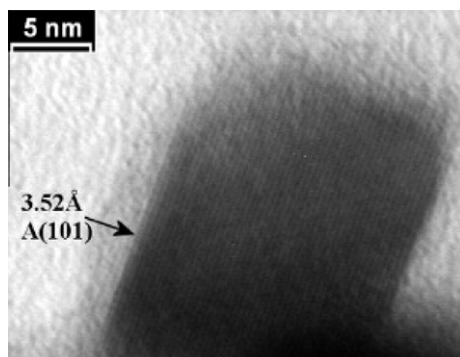


**Fig. 34.** HRTEM image of the rod-like shape TiO<sub>2</sub> particle. Reprinted from Ref. [226] with permission of Elsevier.

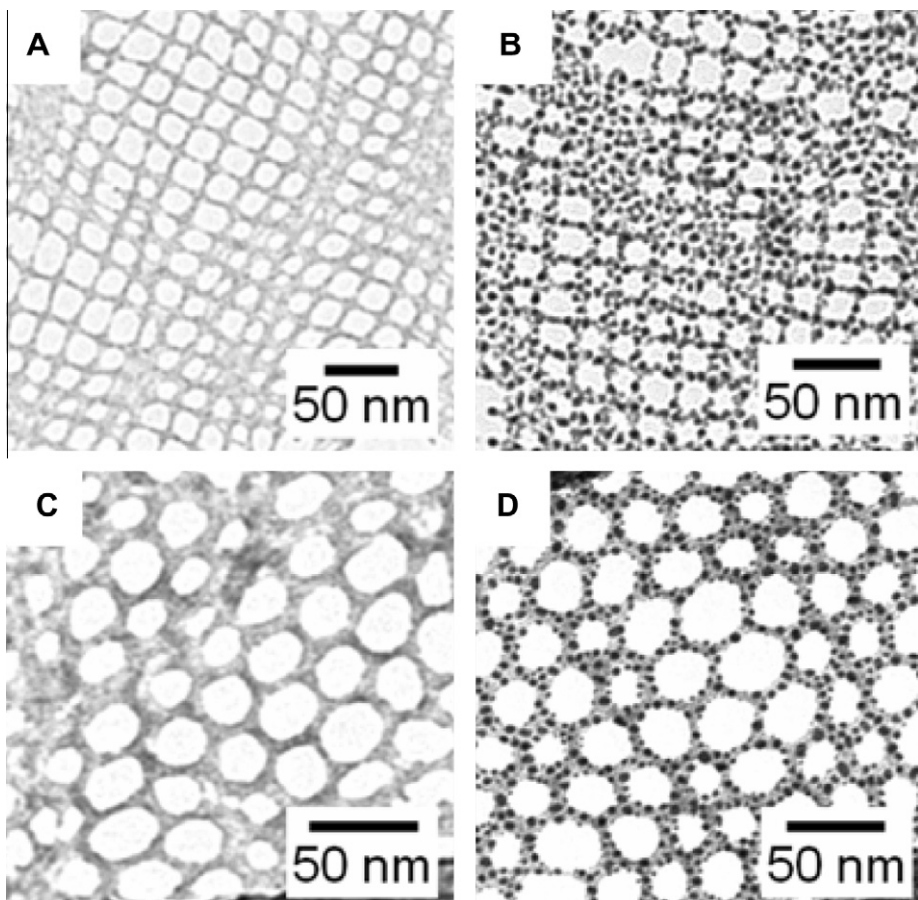


**Fig. 35.** (A and C) TEM images of uranyl acetate-stained DNA arrays. (B and D) 2D DNA arrays deposited with 8 Å of gold, irradiated under an electron beam, and visualized by TEM. Reprinted from Ref. [229] with permission of ACS Publishers.

monolayer polystyrene sphere (PS) was fabricated on a glass substrate by a micromolding technique. The number of stacking layers in the crystal can be controlled by selecting proper spacers between glass substrates forming the microchannel. Next, a metal film was sputtering-deposited onto the colloid crystal template under a controllable deposition rate. By controlling sputtering time, various morphologies of metal coating onto PS spheres can be achieved. After metal deposition, the ordered arrays of the partially deposited metal PS beads were transferred onto an adhesive tape by peeling-off a tape stripping method. At the end of experiment, the sample was dipped in a toluene solution, where the supporting dielectric particles were completely dissolved, leaving behind an ordered metallic nanostructure. Fig. 36 shows a SEM images of an ordered Au nanobowls array, which obtained by an appropriate combination of nanosphere lithography and physical sputtering technique. They also suggested that the morphology of cavity-containing metal particles depends on the coating time and number of stacking layer in colloidal crystal template.

2D ordered hollow sphere arrays synthesized via lithography processes have special geometric morphology, high surface area, enhanced capacity retention, and large diffusion and transportation channels. They could be very beneficial as both in fundamental research and in practical applications, such as surface science, catalysis, SERS, and electrochemistry. For example, Duan et al. [232] prepared 2D ordered hollow sphere arrays of conductive materials (Gold, polypyrrole, and CdS) on indium-tin-oxide (ITO-glass) by nonshadow deposition dominated colloidal lithography (NSCL). In their

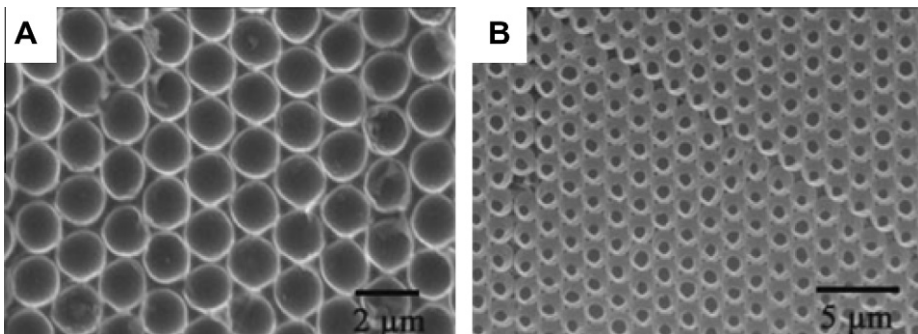


**Fig. 36.** SEM images of ordered gold nanobowls array at (A) high- and (B) low-magnification. Reprinted from Ref. [230] with permission of Japan Society of Applied Physics.

experiment, first, an ion-sputtering system is used to sputter a thin layer of gold on a PS colloidal template. A hollow sphere array can thus be obtained by further electrochemical deposition on such a template and subsequent removal of PSs. Their results suggest that the NSCL approach is flexible and easy to control the nanostructure and size of the hollow sphere array, and some other new features are as follows: (1) controllable shell of the hollow sphere from single-layer to multilayer with single or multiple compositions, (2) tunable morphology from simple structure to hierarchical nanostructure, and (3) changeable arrangement of hollow spheres from close-packing to non-close-packing. Moreover, the hollow sphere size and the shell thickness can also be controlled by changing the colloidal sphere and deposition time, respectively. Fig. 37 shows the SEM and TEM micrographs of ordered hollow sphere arrays of gold, polypyrrole, and CdS materials.

More recently, Lee et al. [233] fabricated an elliptical gold nanodisk arrays onto a clean glass substrate by the serial processes of NIL, tilted evaporation, O<sub>2</sub> plasma etching, metal deposition, and lift-off. For a typical fabrication of gold nanodisks, first, laser interference lithography was used to prepare a Si stamp with nanoscale size. Then the surface of the Si stamp was modified with chemicals for facile release of the stamp from the resin after imprinting. By using a thermal NIL system, the stamp (nano-pillar array) was pressed against curable resin. Next, the resin was diluted with its thinner at a ratio of 3:2 and spin-coated on a clean glass substrate at 3000 rpm for 30 s. The imprinting was performed under a low pressure at 180 °C for 10 min and maintained until the temperature decreased below 50 °C. A 2 nm thin layer of chromium was deposited four times in different directions via e-beam evaporator to protect a top layer of the patterned resin from plasma etching. The residual layer was removed by plasma etching. Lastly, a Ti/Au layer was coated by e-beam evaporation. A lift-off was achieved with ultrasonic agitation in the presence of acetone.

Over the past years, a hot plasma or arc plasma method has been used to synthesize a 2D NSM. For example, Nayak et al. [52] fabricated the 2D SiC dendrite structure via arc plasma method. In the synthesis of SiC dendrite, first, rice husk ash containing SiO<sub>2</sub>, C, and <2% other constituents (such as K<sub>2</sub>O, Na<sub>2</sub>O, CaO, MgO, Fe<sub>2</sub>O<sub>3</sub>, P<sub>2</sub>O<sub>5</sub>, and SO<sub>3</sub>) was mixed with graphite powder (ratio of C: SiO<sub>2</sub> is 3:1). Then, the resulting product was then charged into a graphite crucible kept inside an arc plasma furnace. Carbothermal reduction of the ash was performed under plasma condition at 2500–2550 K for 30 min in the presence of argon gas and then followed by 2 h furnace cooling to room temperature. The cooled powdery product was washed with 40% HF/HCl mixture to remove unreacted silica and mineral oxides. It was then successively washed with DI water to remove Cl<sup>-</sup> and F<sup>-</sup> ions. Free carbon from the powder was taken out by heating at 973 K for 2 h. TEM shows (Fig. 38) the occurrence of equi-spaced primary branches (~60–70 nm in length) in the dendrite consisting of nanorod bundles.

Recently, low-temperature plasma (cold plasma) can also be used to synthesize a 2D NSMs. For instance, Vizireanu et al. [234] grow the carbon nanowall/Ni/Si in a plasma beam sustained by an expanding Ar rf discharge and injected with a small amount of acetylene in the presence of hydrogen as active gas. In a typical fabrication of 2D carbon nanowalls, first a silicon wafer is sputter-coated

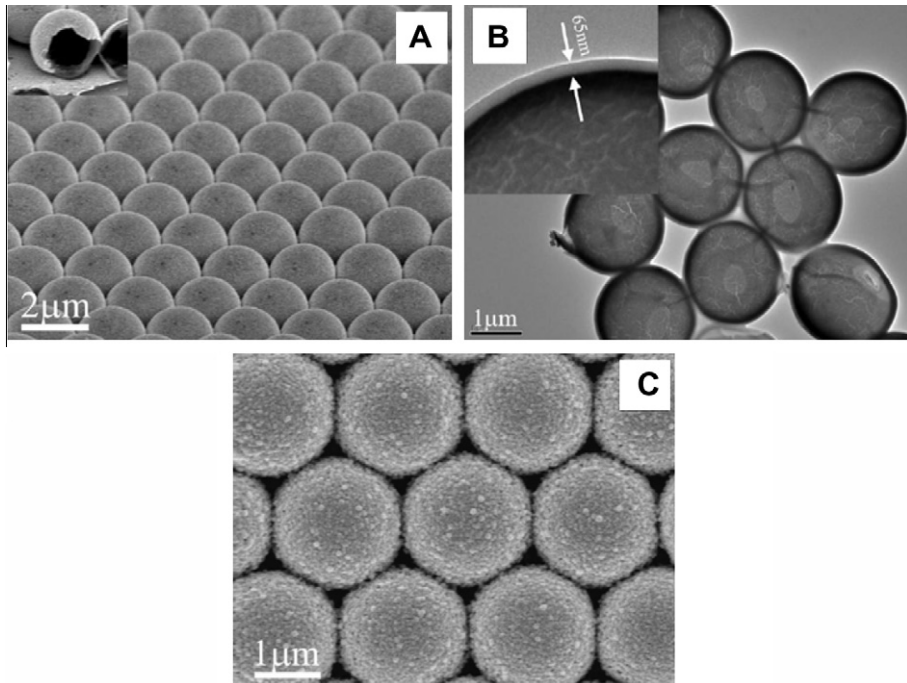


**Fig. 37.** (A) SEM image of gold hollow spheres; inset: tilted image in the edge region with broken spheres. (B) TEM images of as-prepared PPy hollow spheres; inset showed the thickness of deposited PPy. Electrochemical deposition time is 120 s. (C) SEM image of CdS hollow sphere. Electrochemical deposition time is 3 h. Reprinted from Ref. [232] with permission of ACS Publishers.

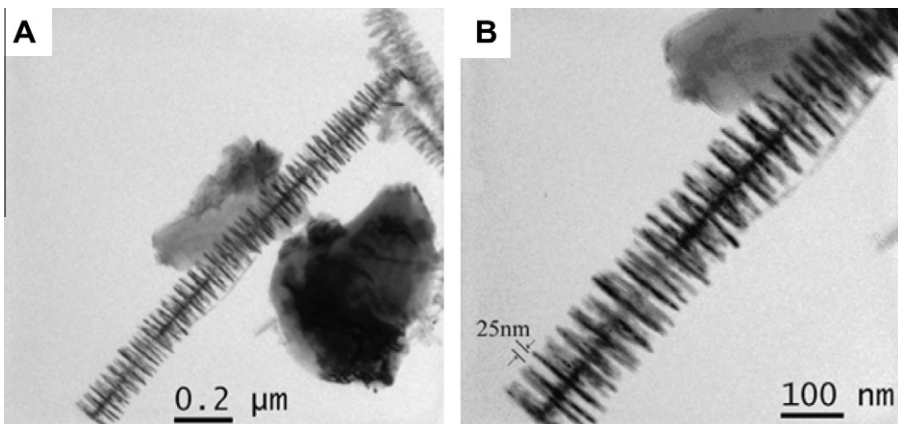


**Fig. 38.** TEM images of SiC dendrite grown by arc plasma at (A) low and (B) high magnification. Reprinted from Ref. [52] with permission of The American Ceramic Society.

with a layer of Ni catalyst and then Ni/Si is used as substrate. The Ni thin films were then transformed in particles by annealing and plasma treatment in ammonia or hydrogen. Further, acetylene and ammonia/hydrogen were introduced in the chamber through the same injection ring, situated in the nozzle proximity. The mass flow rate of the Ar gas was fixed between 100 and 1000 sccm, and

those of the other gases ( $\text{C}_2\text{H}_2$ ,  $\text{NH}_3$ , or  $\text{H}_2$ ) between 1 and 20 sccm. During the deposition, the pressure was in the range of  $10^{-1}$ –3 mbar. More recently, the same author reported a detailed study on the synthesis of 2D carbon nanowalls by an rf expanding plasma beam [56]. Fig. 39 shows SEM and TEM images of the carbon nanowalls deposited under the standard conditions. Moreover they found that the densities and morphologies of carbon nanowalls can be controlled by changing position with respect to the precursor injection point. By manipulating the experimental conditions, they obtained well separated carbon nanowalls with the largest surface area.

Spray-pyrolysis processing is a facile method for production of 2D NSMs. For example, Pingali et al. [235] synthesized a 2D Ru–Ni–S dendrite structures onto a carbon film by spray-pyrolysis method. In a typical synthesis of Ru–Ni–S dendrite structures, the starting molar ratio of Ru:Ni:S was kept at 1:1:3 and mixed with methanol at 0.05 M. Then, the following synthesis conditions are applied: atomizer power = 8 W, argon flow rate =  $120 \text{ mL min}^{-1}$ , and temperature =  $1000^\circ\text{C}$ . They found that the morphology of the Ru–Ni–S is influenced by the temperature, gas flow rate and atomizer power. More recently, Mann and Skrabalak [54] used the spray pyrolysis technique to fabricate the  $\text{Bi}_2\text{WO}_6$  nanoplates. For fabrication of  $\text{Bi}_2\text{WO}_6$  nanoplates, 15 mL of water was mixed to a vial containing 0.25 g of  $\text{Na}_2\text{WO}_4 \cdot 2\text{H}_2\text{O}$  (0.00075 mol) and 0.4726 g of  $\text{BiCl}_3$  (0.0015 mol). Then the colloidal suspension was agitated in an ultrasonic bath for 1 min. Finally, the suspension was then sparged with  $\text{N}_2$  gas at 55 sccm for 30 min, followed by nebulization. An ultrasonic transducer was used to nebulize the precursor solutions. The furnace temperature was  $600^\circ\text{C}$ . Products were obtained by centrifugation and washed with DI water. Fig. 40A and B shows a SEM and TEM pictures of  $\text{Bi}_2\text{WO}_6$  nanoplates. The inset in TEM image shows the SAED pattern of the  $\text{Bi}_2\text{WO}_6$  nanoplate. A proposed mechanism for  $\text{Bi}_2\text{WO}_6$  nanoplate's formation is schematically shown in Fig. 40C, which is confirmed by thermal analysis. They found that the metathesis reaction plays an important role in the synthesis of single-crystalline shape-controlled particles. The average diameter and thickness of  $\text{Bi}_2\text{WO}_6$  nanoplates are  $433 \pm 134 \text{ nm}$  and  $46 \pm 16 \text{ nm}$ , respectively. The SAD (Fig. 41B, inset) shows that the nanoplates are single-crystalline and bound on the top and bottom by (001) facets.

Dato et al. [236] fabricated large quantity graphene nanosheets by inert gas phase condensation technique. The synthesis of graphene sheets can be carried out using an atmospheric-pressure microwave plasma reactor. A smaller alumina tube concentrically located within the quartz tube was used to send an aerosol consisting of argon gas and ethanol droplets directly into the argon plasma. Ar plasma was generated by stream. Ethanol droplets rapidly evaporated and dissociated in the plasma, forming solid matter. After passing through the plasma, reaction products underwent fast cooling and were collected on nylon membrane. Finally, graphene sheets collected on the filters were sonicated in methanol for 5 min. Thus, we can say that the inert gas phase condensation technique is very useful for synthesis of 2D NSMs.

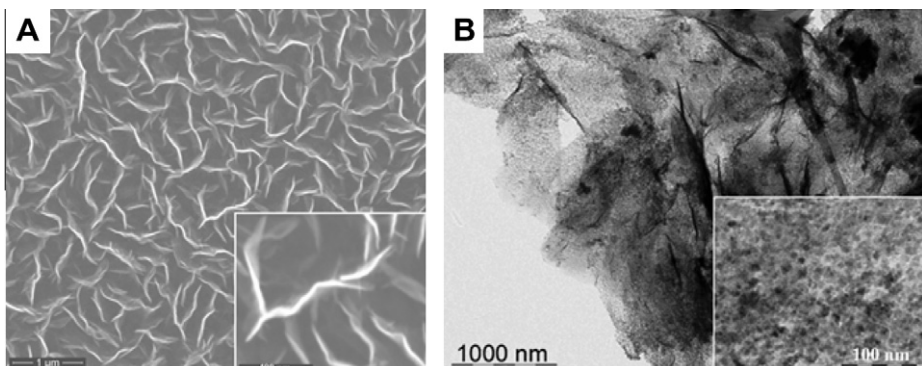


**Fig. 39.** (A) SEM and (B) TEM image of carbon nanowalls deposited under the optimized conditions. Insets of both figures show a high magnification image. Reprinted from Ref. [56] with permission of IOP Publishing Ltd.

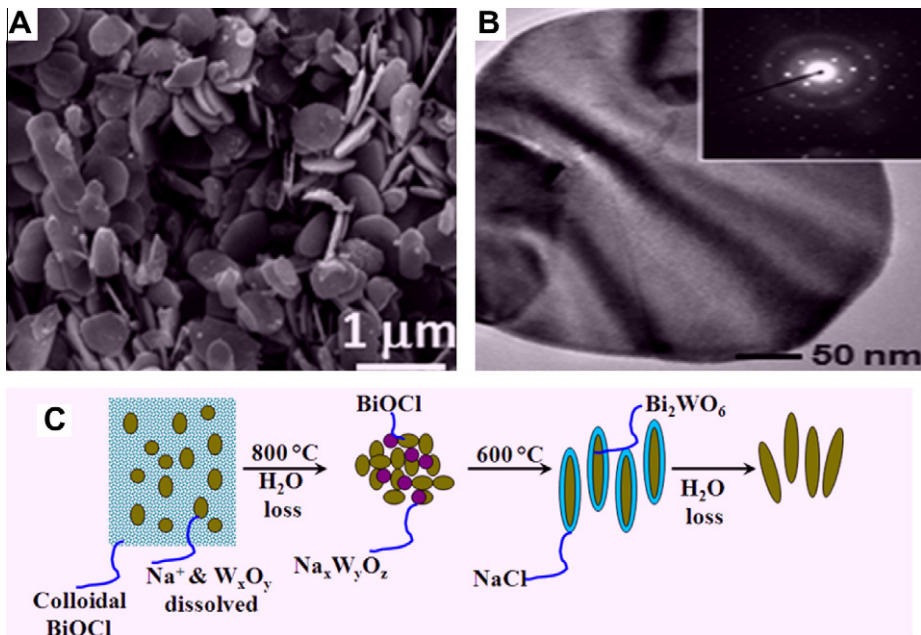


**Fig. 40.** (A) SEM image of  $\text{Bi}_2\text{WO}_6$  nanoplates and (B) TEM image of  $\text{Bi}_2\text{WO}_6$  nanoplates; inset SAED. (C) Cross-sectional representation of the physical and chemical processes occurring during the spray pyrolysis fabrication of  $\text{Bi}_2\text{WO}_6$  nanoplates (modified from Ref. [42]). Reprinted from Ref. [54] with permission of ACS Publishers.

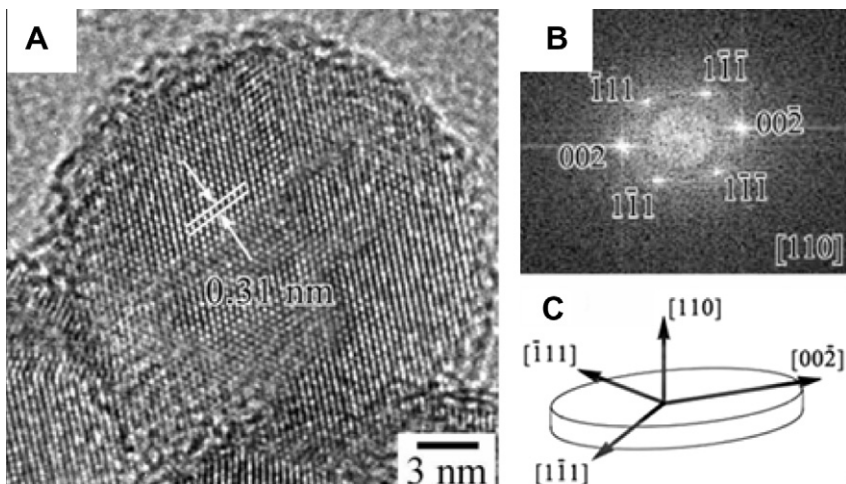


**Fig. 41.** (A) HRTEM image of Si nanodisk. (B) FFT pattern derived from the image in part A. (C) schematic drawing of the crystal structure of the nanodisk. Reprinted from Ref. [238] with permission of ACS Publishers.

Over the past decade, pulsed laser ablation has proven to be an effective method for preparation of 2D NSMs such as nanodisks and nanoleaf [237–239]. Qin et al. [238] fabricated the silicon nanodisks by the pulsed-laser-ablation-in-liquid technique. For the synthesis of silicon nanodisks, commercial  $\text{SiO}$  powder was used as a starting material. Pulsed laser was then used to irradiate a  $\text{SiO}$  suspension

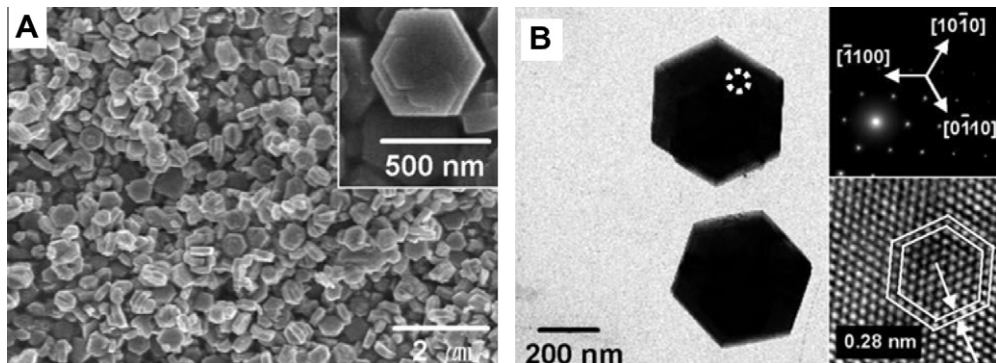


**Fig. 42.** (A) SEM and (B) TEM images of ZnO nanodisks. Reprinted from Ref. [57] with permission of ACS Publishers.

in a glass cuvette for 120 min. The synthesis conditions were wavelength = 1064 nm, frequency = 20 Hz, and 1.2 ms pulse width. The laser beam with single pulse energy of 4.895 J was focused ~5 mm below the liquid surface with a spot size of 0.2 mm. The as-prepared suspension was of dark-yellow color. Lastly, the products were filtered and then HF solution was used to remove surface SiO<sub>2</sub>. Fig. 41A shows an HRTEM image of Si nanodisk. The interplanar spacing is about 0.31 nm, which corresponds to the (111) spacing of Si. The fast Fourier transform (FFT) analysis of the nanodisk gives a (110) oriented diffraction pattern, as shown in Fig. 41B. The crystallographic directions of the nanodisk are more schematically shown in Fig. 41C, where the upper and lower disk faces are the (110) planes and possible planes at the lateral surface are expected to be (111), (002), and others perpendicular to the (110) plane. In their results indicate that the Si nanodisks gave blue light emission under ultraviolet irradiation, which can be ascribed to oxide-related defects on their surface.

Yang et al. [239] used pulsed-laser-ablation-in-liquid technique to fabricate zinc oxide nanoleaf structure at room temperature and pressure. For a typical synthesis of zinc oxide nanoleaf structure, Zn powder was compressed under pressure to form a solid target for ablation. The synthesis conditions were wavelength = 532 nm, frequency = 10 Hz, 15 ns pulse width, SDS concentrations = 0.05 M and ablation time = 5 h. The laser beam with pulse energy of 100 mJ was focused ~5 mm below the liquid surface with a spot size of 0.5 mm. Finally, the products were washed several times with DI water and ethanol, and then separated by centrifugation. After ablation time of 5 h, the ‘leaf-like’ shapes with width of  $\sim 230 \pm 30$  nm and length of  $\sim 770 \pm 90$  nm were observed. The pulsed-laser-ablation-in-liquid technique looks promising for preparing novel 2D NSMs.

A sonochemical reduction method has been recently investigated as a promising alternative technique for the fabrication of 2D NSMs. Jung et al. [57] fabricated ZnO nanodisks using the sonochemical method. In a typical synthesis of ZnO nanodisks, a triethyl citrate ( $\text{HO}(\text{COOC}_2\text{H}_5)(\text{CH}_2\text{COOC}_2\text{H}_5)_2$ ) was used to synthesize ZnO nanodisks. An aqueous solution of 100 mL, which contained zinc nitrate hexahydrate (0.01 M), HMT (0.01 M), and triethyl citrate (0.1 M), was prepared at room temperature. Then, ultrasonication was carried out at an intensity of  $39.5 \text{ W cm}^{-2}$  for 30 min. Finally, the ZnO nanodisk containing solution was filtered, and then the resulting powder particles were washed and dried. Fig. 43 shows the SEM and TEM images of ZnO nanodisks. Hexagon-shaped ZnO nanodisks, with an average diameter of 500 nm and average thickness of 140 nm, could be clearly observed in Fig. 42A. Hexagonal ZnO nanodisks are highly crystalline with a lattice spacing of about  $\sim 0.28$  nm, which corresponds to an interlayer distance of the (1010) planes in ZnO crystal lattice, as shown in Fig. 42B.

Bhattacharyya and Gedanken [240] used a sonochemical method to form porous ZnO nanodisks. For synthesis of porous ZnO nanodisks, 1 g of zinc(II) acetate was dissolved in 100 mL of 10% v/v water-*N,N*-dimethylformamide (DMF) and irradiated with an ultrasonic horn under a flow of inert gas at room temperature for 3 h. Then, resulting products were first washed thoroughly with doubly-distilled water and then with absolute ethanol in an inert glove box ( $\text{O}_2 < 1 \text{ ppm}$ ) and dried in

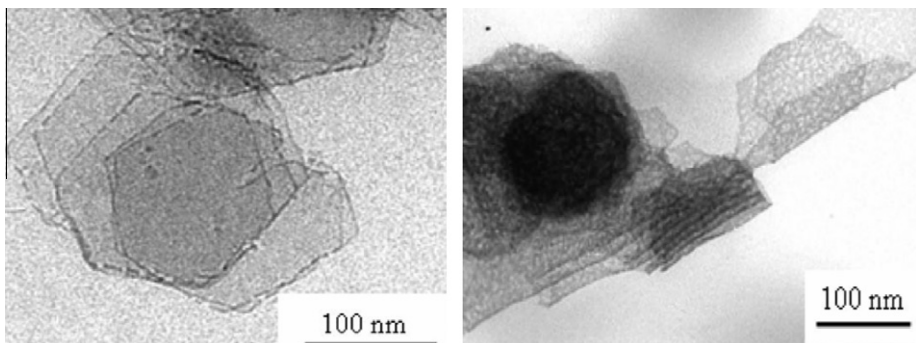


**Fig. 43.** TEM images of hexagonal Pd nanosheets after washing several times with 2-propanol under ultrasounds. Reprinted from Ref. [55] with permission of ACS Publishers.

the vacuum system. They also found that the resultant products are much more porous when the sonohydrolysis is carried out under argon than their sonication under air.

Consequently, all above results and discussion suggest that the physical method is an easy method for fabrication of 2D NSMs. The morphology, particle size, and metallic composition of the 2D NSMs can be tuned based on experimental conditions.

#### 4.3.2. Synthesis of 2D NSMs by chemical processes

Like physical methods, chemical processes have also been widely used to create 2D NSMs such as nanoprisms, hierarchical, nanoplates, nanosheets, nanowalls, nanodisks, and junctions (continuous islands). Template-based methods provide significantly more flexibility in processing to allow for the preparation of such 2D NSMs. For instance, nanosheet- and nanodisk-like structures were prepared by using cetyltrimethylammonium bromide (CTAB) micelles as a soft template method [55,241]. Siril et al. [55] synthesized the hexagonal Pd nanosheets in ternary emulsions made of water/oil/CTAB and quaternary hexagonal mesophases made of water/oil/CTAB/co-CTAB, in which CTAB was used as a surfactant. HRTEM imaging revealed that the hexagonal Pd nanosheets obtained from the CTAB based emulsions (Fig. 43). These hexagonal Pd nanosheets have shown a broad absorption band from the visible to the near infrared region.

However, Chen and Carroll [241] also used the CTBA micelles as a soft template to synthesize large quantities of truncated triangular Ag nanoplates. In a typical synthesis of truncated triangular Ag nanoplates, the Ag ions were first reduced into small Ag seeds, which then grew into truncated triangular Ag nanoplates, in the presence of ascorbic acid and highly concentrated CTBA. For separation and purification of Ag nanoparticles, mild aging and centrifugation were also applied. They also found the Ag nanoparticles with different morphologies, including rods, squares (or cubes), tetrahedra, and disks (or spheres), but their abundance is around 20% in total. The truncated triangular Ag nanoplates have an average edge size of 68 nm, thickness of 24 nm, and the degree of truncation of 0.35. Hao et al. [242] synthesized Ag nanodisks by using polystyrene mesospheres as templates in *N,N*-dimethylformamide (DMF) solution. In that work, polystyrene mesospheres with carboxyl groups absorbed Ag ions to nucleate. Then, the polystyrene mesospheres played the function of template, as they limited the metal particle growth in one direction and led to anisotropic growth. The average diameter and thickness of edge oriented Ag nanodisks are ~36 nm and ~9.0 nm, respectively. Chen and Carroll [243] obtained Ag nanodisks from truncated triangular silver nanoplates at 40 °C by using concentrated CTAB as a template. A single layer of CTAB on the basal face was suggested to account for the anisotropic growth. However, the obtained Ag nanodisks by this method had thickness of the order of 20–30 nm and a diameter ~60 nm.

Kawasaki et al. [244] synthesized single crystalline platinum (Pt) nanosheets in single or mixed surfactant LLC. In the synthesis of single-crystalline Pt nanosheets, they used a chemical reduction of a platinum salt with hydrazine at a graphite/solution interface, using polyoxyethylene (20) sorbitan

monostearate (Tween 60) based self-assembly (hemicylindrical micelle) templates. They also noticed that the thickness of Pt nanosheets is  $\sim 3.5$  nm. The Pt nanosheets are surface-smooth and continuous over relatively large length scales of micrometer sizes. Kawasaki et al. [244] suggested that the interfacially directed growth of Pt metals within the aqueous shells of the Tween 60 hemicylindrical micelles induces the thin Pt crystals as thick as the aqueous shells. In addition, growth of metal particles on the LLC, adsorbed at the solid/solution interface, would be greatly advantageous for producing unknown nanostructured metals.

Sakai et al. [245] developed a new approach to fabricate single crystalline Pt nanosheets by the chemical reduction of a Pt salt based on the interfacial directed growth of Pt metals within LLC at a graphite/solution interface. Then, the nanogroove-network-structured single-crystalline Pt nanosheets were obtained by the  $\text{NaBH}_4$  reduction of  $\text{Na}_2\text{PtCl}_6$  confined to the mixed LLCs. The nanosheets were composed of pseudo 2D irregular Pt networks, in which Pt nanoleaves were loosely interconnected with crystallographic alignment to form an irregular network of nanogrooves [245]. Fig. 44 shows the AFM images for obtained single crystalline Pt nanosheets. Atomic force microscopy (AFM) images indicated that the thickness of Pt nanosheet is about  $\sim 11.7$  nm, which is stacking of four Pt nanosheets.

Recently, Kijima et al. [246] prepared nanohole-structured single-crystalline Pt nanosheets by reduction of  $\text{Na}_2\text{PtCl}_6$  confined to the LLCs using borohydride as the reductant. Moreover, Wang et al. [247] established a novel method to prepare Au nanoplates from LLC. Further research was carried out by Wang et al. [248] to obtain products of controllable shape and size. Single-crystalline Au nanoplates with triangular or hexagonal shapes were synthesized by reducing  $\text{HAuCl}_4$  in LLC with the addition of a small amount of capping agents. Consequently, all above results suggest that the hexagonal LLCs consisting of triple-PEO-chain-based surfactant cylindrical micelles are available for the formation of 2D metal nanosheets.

Another technique widely employed to prepare 2D NSM is two- and three-electrode electrochemical cell system [51,249–252]. Liu et al. [250] used a two electrode electrochemical cell to synthesize the mesoporous hydrous manganese dioxide nanowall arrays. Mesoporous hydrous manganese dioxide nanowall arrays deposited on cathodic substrate by means of water-electrolysis induced precipitation from 0.1 M precursor solution (mixed of manganese acetate and sodium sulfate) at a voltage of  $-1.8$  V for 15 min. The following reactions are involved in the deposition of manganese dioxide nano-

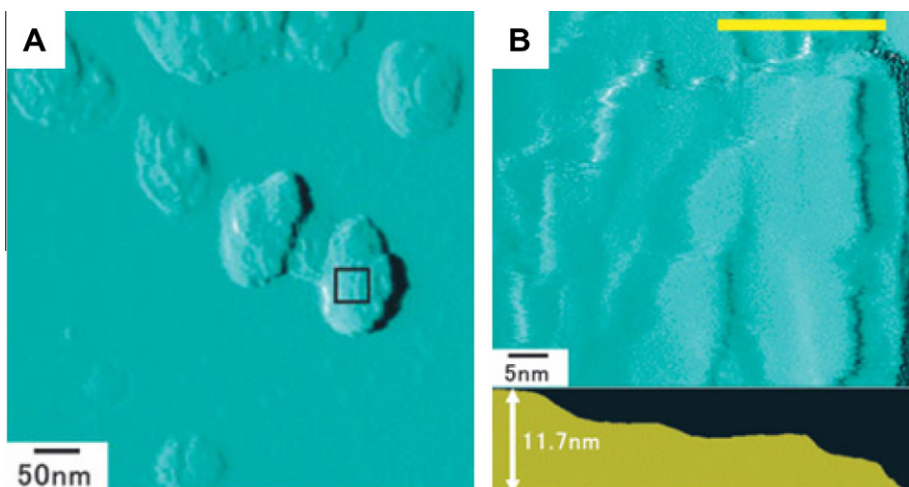


**Fig. 44.** (A) AFM image of Pt nanosheets and (B) AFM image of selected region of Pt nanosheets shown in (A). In (B), yellow line shows the scan line for measured the thickness of Pt nanosheets. Bottom of (B) shows the stacking of four nanosheets with a total thickness of  $\sim 11.7$  nm. Reprinted from Ref. [245] with permission of Wiley-VCH Verlag GmbH & Co. KGaA.

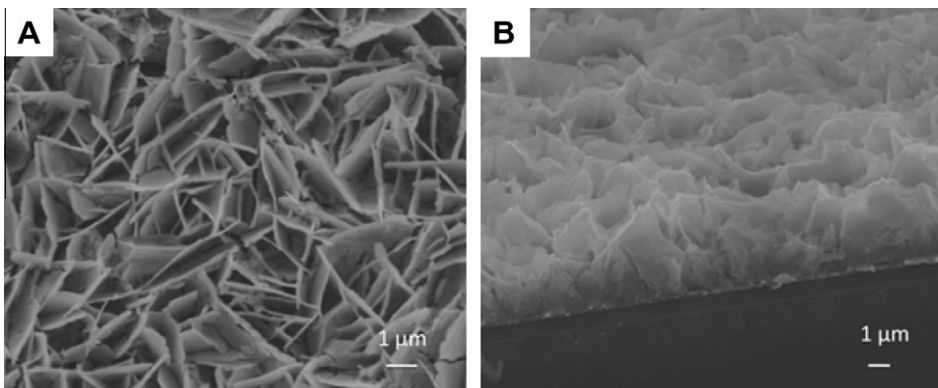
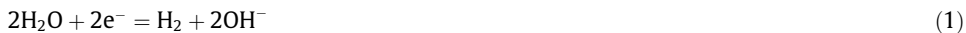


**Fig. 45.** SEM images of mesoporous hydrous manganese dioxide nanowall arrays deposited on cathodic substrate: (A) plan-view and (B) cross-section view. Reprinted from Ref. [250] with permission of Wiley-VCH Verlag GmbH & Co. KGaA.

walls. When a voltage was applied, the water electrolysis occurred at the cathode surface, generating hydrogen gas and  $\text{OH}^-$  groups:



Then, the generated  $\text{OH}^-$  groups from bonds with  $\text{Mn}^{2+}$  ions, causing nanoparticle precipitation:



**Fig. 45** shows the SEM images of manganese oxide film grown on cathodic substrate. The cross-section SEM image (**Fig. 45B**) depicts that the nanowall array was deposited with no continuous film at the interface between the Pt film and manganese oxide nanowall arrays.

He et al. [251] used a three-electrode electrochemical cell to prepare the cobalt nanowall arrays on the copper substrate. In a typical synthesis of cobalt nanowall arrays, the copper foil was treated with 0.1 M HCl aqueous solution, and then cleaned by sonication in acetone for 5 min. The electrolyte solution was prepared by dissolving 0.1 M  $\text{Li}_2\text{SO}_4 \cdot \text{H}_2\text{O}$  and 20 mM  $[\text{Co}(\text{NH}_3)_5\text{Cl}]\text{Cl}_2$ . Further, the cyclic voltammetry (CV) was conducted for 10 circles with the potential sweep between −0.4 and −1.2 V, and the constant scan rate was set as 20 mV s<sup>−1</sup>.

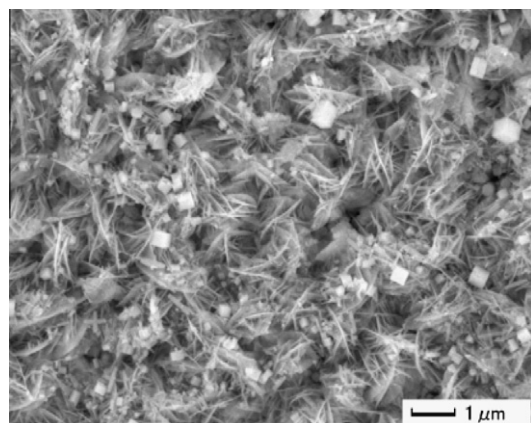


**Fig. 46.** SEM images of  $\text{In}(\text{OH})_3$  nanosheets. Reprinted from Ref. [252] with permission of ACS Publishers.

Chu et al. [252] used a standard three-electrode electrodeposition setup consisting of an Ag/AgCl reference electrode, Pt foil counter electrode, and the tin-doped indium oxide working electrode. In(OH)<sub>3</sub> nanosheets are synthesized at low In<sup>3+</sup> concentrations ([In<sup>3+</sup>] = 0.008 M) at 65 °C and –1.2 V for 1 h. The SEM images of In(OH)<sub>3</sub> nanosheets are shown in Fig. 46. They also revealed that the growth behavior of In(OH)<sub>3</sub> was mainly determined by the indium nitrate concentration and applied potential. Well-defined ellipsoids, cubes, and rods could be prepared under suitable conditions. The formation of different nanostructures can be explained by initial self-assembly of In(OH)<sub>3</sub> nanosheets and a subsequent ripening process under different conditions.

Tiwari et al. [51] prepared continuous Pt island networks using a single-step three-electrode electrodeposition process. The continuous Pt island networks were fabricated in a 1 M K<sub>2</sub>PtCl<sub>6</sub>/1 M H<sub>2</sub>SO<sub>4</sub> solution by holding the high- and low-potential pulse at (+0.08 V) and (–0.01 V), respectively. The time durations for the high- and the low-potential pulse were 3 ms and 1 ms, respectively. The Pt islands are mutually connected over the Si substrate and have size distribution from ~200 nm to ~800 nm. Consequently, all above results suggest that the two- and three-electrode electrodeposition processes are available for the formation of 2D NSMs.

Electroless deposition is a most common method for generating a variety of 2D metal nanostructures. Generally, electroless deposition processes are carried out in acidic, basic, or neutral aqueous solutions and requires a reducing agent. For example, Aherne et al. [253] synthesized Ag nanoprisms using electroless deposition. Typically, nanoprisms are prepared by mixing 35 mL of DI water, ascorbic acid (0.525 mL, 10 mM), and 3.5 mL of silver nanoparticle seed solution, followed by the addition of AgNO<sub>3</sub> solution (21 mL, 0.5 mM) at a rate of 4 mL min<sup>−1</sup> while stirring vigorously. After the reaction was completed, trisodium citrate solution (17.5 mL, 25 mM) is added. The size of the formed Ag nanoprisms is ~21 nm. The Ag nanoprisms are single crystal with their basal plane as (1 1 1) lattice plane. By reducing the volume of seed solution, it is possible to manipulate the size of Ag nanoprisms.

Jiang et al. [254] also applied the electroless process to fabricate Cu microstructures assembled with nanowalls. In their experimental procedure, 0.01 mol of CuCl and 0.01 mol of NaOH were dissolved in 20 mL of DI water; then 0.03 mol of NaH<sub>2</sub>PO<sub>2</sub>·H<sub>2</sub>O was added to the above solution under vigorous stirring for 5 min. Then, the solution was transferred into a 50 mL Teflon-lined stainless steel autoclave, which was then filled with distilled water up to 90% of the total volume. The autoclave was sealed and maintained at 200 °C for 24 h. After completion of the reaction, resulting solid products were filtered off, washed with absolute ethanol and DI water several times, and then dried in a vacuum at 60 °C for 6 h. In Fig. 47, we can see SEM images of Cu microstructures with net shape consisting of nanowalls. They also found that the morphology of Cu microstructures are controlled by adding NaOH in aqueous solution and choosing of NaH<sub>2</sub>PO<sub>2</sub>·H<sub>2</sub>O as the reducing agent.

Kamada et al. [255] synthesized 2D iron oxyhydroxide thin films on bare Pt substrate using an electroless deposition process. In their experiment, iron oxyhydroxide thin films were performed in a glass cell including a mixed aqueous solution of 0.03 M FeSO<sub>4</sub>–0.03 M CH<sub>3</sub>COOH. Then, the Pt substrate was

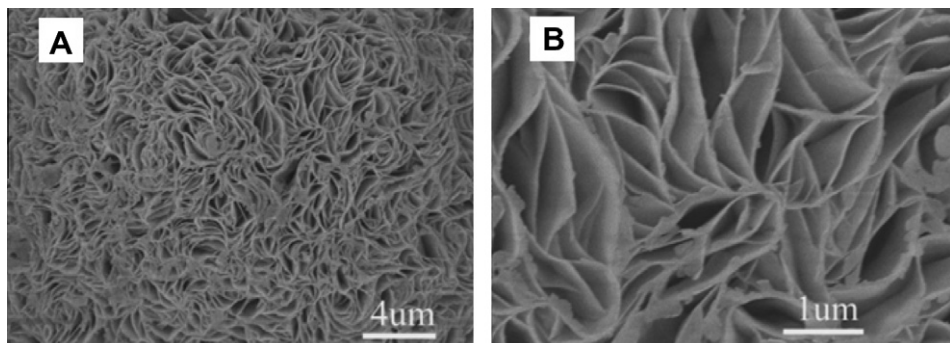


**Fig. 47.** SEM photographs at (A) low- and (B) high-magnifications showing the copper microstructures with net shape consisting of nanowalls. Reprinted from Ref. [254] with permission of ACS Publishers.

dipped in a naturally aerated solution at room temperature for various periods, where the Ti foil was also employed in a few cases. During the reaction, the substrate was exposed to the light from a 300 W Xe lamp. The open-circuit potential of the Pt substrate was monitored against the saturated Ag/AgCl reference electrode. The films obtained were cleaned by water and dried at room temperature. The amount of Fe deposited on the Pt was measured by colorimetric analysis using 1, 10-phenanthroline after dissolving a film in HCl solution, followed by neutralization and reduction treatments by addition of NH<sub>3</sub> and hydroxylamine-HCl salt solutions, respectively. The morphology and crystal structure of as-postannealed films (873 K, 1 h in air) were observed. The photoanode performance of the postannealed films was assessed by anodic polarization under intermittent illumination of visible light in 1 M CH<sub>3</sub>OH–0.1 M K<sub>2</sub>SO<sub>4</sub> using Ag/AgCl and Pt as reference and counter electrodes, respectively. The potential scan rate was 10 mV s<sup>-1</sup>. The water used in all processes was doubly DI water. Consequently, all above results suggested that the electroless deposition is a cheap and useful process for creating 2D NSMs.

Hydrothermal methods are ideally suited for rapid synthesis of large quantities of 2D metal oxide or metal nanostructures [256,257]. For example, MnO<sub>2</sub> nanostructures with different morphologies, such as hexagramlike and dendritelike hierarchical forms, were successfully synthesized via a facile hydrothermal route [256]. In a typical synthesis of 2D hexagonal starlike β-MnO<sub>2</sub> crystals, a Mn(NO<sub>3</sub>)<sub>2</sub> solution (1.2 M and 2.0 M) was transferred into a Teflon-lined stainless steel autoclave and heated at 160–180 °C for 3–72 h. For the preparation of dendritelike hierarchical β-MnO<sub>2</sub> nanostructures, stoichiometric moles of Mn(NO<sub>3</sub>)<sub>2</sub> and nitric acid were well mixed and hydrothermally treated. In both cases, the product was collected, washed, and dried. Fig. 48 shows the SEM images of the as-synthesized 2D hexagonal starlike β-MnO<sub>2</sub> and dendritelike hierarchical β-MnO<sub>2</sub> nanostructures.

Recently, Takami et al. [257] fabricated nickel oxide nanoplates in hydrothermal reaction using a flow-type reactor. In the synthesis of nickel oxide nanoplates, an aqueous mixture of Ni(NO<sub>3</sub>)<sub>2</sub> (0.01 mol L<sup>-1</sup>) and H<sub>2</sub>O<sub>2</sub> (2.57 mol L<sup>-1</sup>) was used. H<sub>2</sub>O<sub>2</sub> was added to synthesize NiO in an oxidative condition. The flows of the reactants and the heated water were mixed at a junction to raise the temperature of the Ni<sup>2+</sup> ion solution instantaneously. The temperatures of the water and the mixed flow were set to ~390 and 350 °C, respectively. After passing the isothermal region, the product was cooled very quickly to room temperature with water. Residential time in the isothermal region was 16 s. The cooled products were filtered through a 0.5 μm filter to remove accidentally produced large particles.

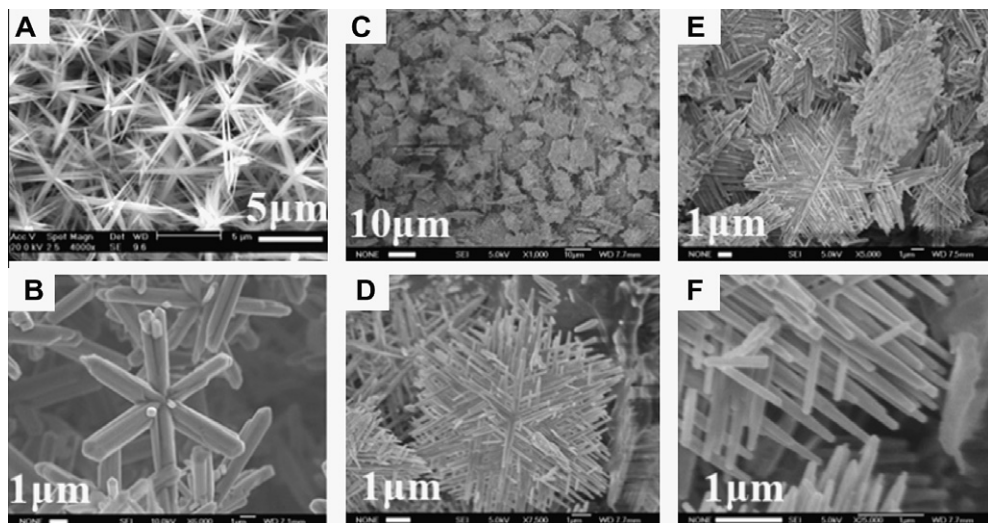


**Fig. 48.** SEM images of the hexagonal starlike β-MnO<sub>2</sub> crystals synthesized from (A) 1.2 M and (B) 2.0 M Mn(NO<sub>3</sub>)<sub>2</sub> solution. (C–F) SEM images at different magnifications of the dendritelike hierarchical β-MnO<sub>2</sub> nanostructures synthesized from Mn(NO<sub>3</sub>)<sub>2</sub>–nitric acid solution. Reprinted from Ref. [256] with permission of ACS Publishers.

The products were purified by a combination of centrifugation and decantation. The nickel oxide nanoplates had a thickness of ~10 nm and a lateral size of 100–500 nm.

The solvothermal processes are very facile routes to synthesize of 2D NSMs [258,259]. For example, silver nanosheets, and chainlike sheets have been successfully synthesized by a controlled solvothermal process in the presence of ammonia and  $\text{AgNO}_3$  [258]. For the typical synthesis of such chainlike sheets,  $\text{AgNO}_3$  (100 mg) was dissolved in ethanol (10 mL) with  $0.07 \text{ mol mL}^{-1}$ , and  $0.13 \text{ mol mL}^{-1}$  ammonia concentrations, respectively. The solution mentioned above is transferred into a stainless steel autoclave. Then, temperature was fixed at  $250^\circ\text{C}$  for 10 h. The solutions are then cooled to room temperature. The product was then washed by DI water and ethanol. They found that the morphology of Ag nanoparticles depends on concentration of ammonia, reaction temperature, and time.

Li et al. [259] also used a solvothermal method to fabricate CuS nanoplates by using copper nitrate and sulfur. For the synthesis of CuS nanoplates, 1 mmol  $\text{Cu}(\text{NO}_3)_2 \cdot 3\text{H}_2\text{O}$  was dissolved in 40 mL ethanol and then 2 mmol sulfur was added into solution under vigorous stirring for 30 min. Furhter, the solution was transferred into a 60 mL Teflon-lined stainless steel autoclave, sealed, and fixed at  $150^\circ\text{C}$  for 24 h and then cooled to room temperature. At the end of experiment, the black precipitates were centrifuged and washed with DI water and ethanol several times and dried under vacuum at  $60^\circ\text{C}$  for 4 h. To understand the role played by solvents on the growth of CuS architectures in their synthetic route, parallel experiments were also carried out in  $\text{H}_2\text{O}$ , ethylene glycol (EG) and dimethylformamide (DMF). Fig. 49 shows the SEM images of CuS architectures prepared in different solvents. According to their results, the CuS products synthesized in DMF were nanoplates and the samples prepared in ethanol were flower-like morphology composed of large numbers of nanoplates, but those synthesized in EG were CuS architectures with high symmetry made up of several nanoplates arranged in a certain mode.

The sol-gel process (or sol-gel deposition) is widely used to synthesize 2D NSMs based on the polymerization of molecular precursors via wet chemical methods [260–262]. For example, Wang et al. [261] synthesized 2D  $\text{MoO}_3$  nanoplatelets on silicon substrate using a sol-gel process. In a synthesis of 2D  $\text{MoO}_3$  nanoplatelets, a stoichiometric amount of molybdenum isopropoxide ( $\text{Mo}(\text{OC}_3\text{H}_7)_5$ ) and 1-butanol was dissolved in a distilled water to form a 0.2 M solution. After mechanically agitating for 5 min, the solution was ultrasonicated for 2 h and then aged in a closed container for 24 h. At the same time, poly(ethylene oxide) was dissolved in ethanol by continuously stirring at  $50^\circ\text{C}$  to form a viscous solution with a concentration of  $0.05 \text{ g mL}^{-1}$ . This resulting solution was mixed with the molybdenum oxide sol in the volume ratio of 1:1. Nanocomposite film was then formed on the bare Si substrate by the dip-coating method. Then the composite film was calcined at  $500^\circ\text{C}$ , to obtain crystallized molybdenum oxide. Fig. 50 shows the SEM images of 2D  $\text{MoO}_3$  nanoplatelets at different magnifications.

More recently, Azimirad et al. [262] also used the sol-gel process to prepare the 2D  $\text{W}_{17}\text{O}_{47}$  nano-thick plates with preferred orientation on glass substrate. In a typical synthesis, first 6 g of sodium tungsten dehydrate was immersed in 30 mL of nitric acid solution for 15 min to exchange the  $\text{Na}^+$  ions with  $\text{H}^+$ . Then the resulting solution was dissolved in 10 mL of  $\text{H}_2\text{O}_2$ , after which 1 mL of ethanol was added to the solution. It was then exposed to light using a commercial 100 W lamp for 2 h in order to concentrate the aqueous solution. Next, after another 24 h aging, the deposition process was performed by dipping the cleaned glass substrates into the solution for 60 s. Then the deposited films were dried at  $100^\circ\text{C}$  in air for 1 h. The thickness of the dried films was measured ~200–300 nm. The reaction for the growth of nanothick plates was performed in a horizontal quartz tube furnace at  $700^\circ\text{C}$ . They also found that the 60 min annealed sample has the maximum number of nanothick plates per unit area over the surface.

Over the past decade, CVD processes have received considerable attention for the synthesis of 2D NSMs. Barreca et al. [263] synthesized a 2D zinc oxide nanoplatelets on Si substrate by CVD starting from a second-generation  $\text{Zn}^{II}$  precursor,  $\text{Zn}(\text{hfa})_2\text{TMEDA}$  ( $\text{hfa} = 1,1,1,5,5,5\text{-hexafluoro-2,4-pentanedione}$ ; TMEDA =  $N,N,N',N'$ -tetramethylethylenediamine). The synthesis was carried out in the presence of nitrogen and wet oxygen atmosphere under optimized conditions, at temperatures between 250 and  $450^\circ\text{C}$ . According to their results, the morphology of NSMs as well as the average nanodeposit thickness could be influenced by the growth temperature. More recently, Gao et al. [264] fabricated large quantities of hexagonal boron nitride nanosheets via a chemical vapor deposition process at

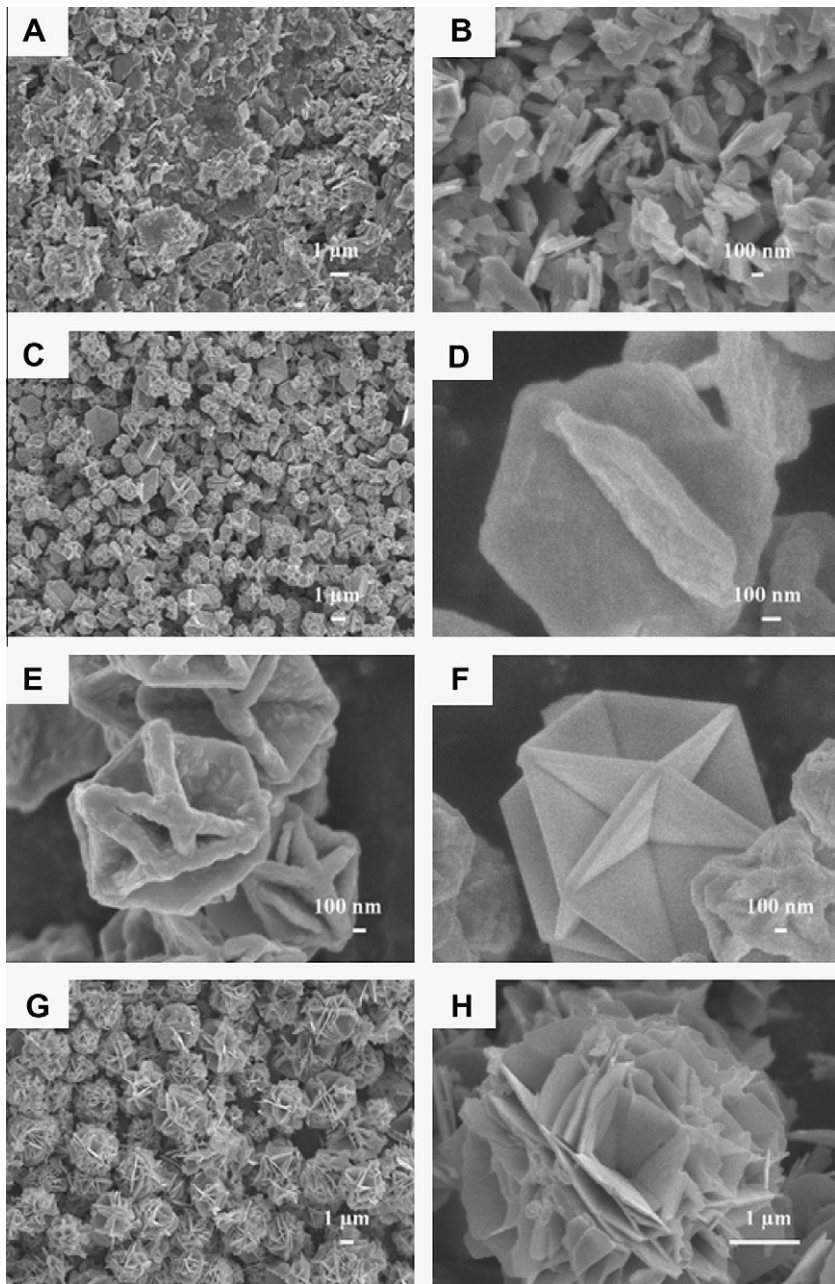


**Fig. 49.** SEM images of the CuS architectures prepared in different solvents: (A and B) ethanol, (C–F) ethylene glycol, and (G and H) dimethylformamide. Reprinted from Ref. [259] with permission of Elsevier.

1100 and 1300 °C. In a typical experimental procedure,  $B_2O_3$  and melamine were mechanically mixed, and the mixed powders as precursors were placed into a crucible. The crucible containing the precursors was placed at the middle of a high-purity graphite induction-heated cylinder. Then, evacuation of

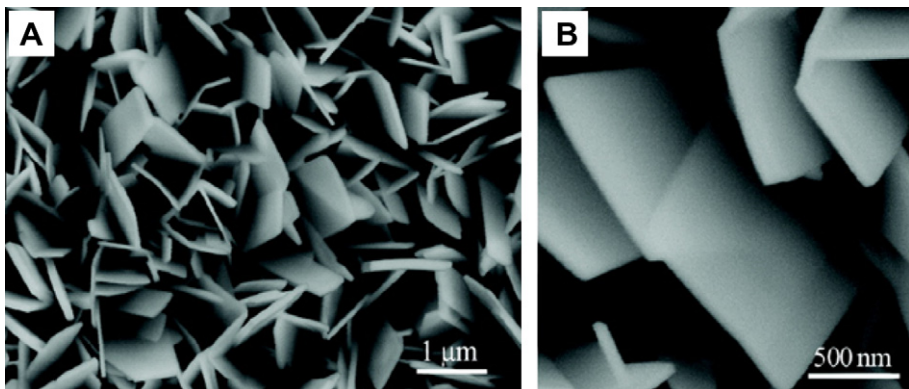


**Fig. 50.** SEM images of the 2D  $\text{MoO}_3$  nanoplatelets under (A) low- and (B) high- magnifications. Reprinted from Ref. [261] with permission of ACS Publishers.

the quartz tube to about 2–3 Torr, high-purity Ar was introduced as a carrier gas at a flow rate of 30 sccm.  $\text{N}_2$  gas was then introduced as a reaction gas with a flow rate of 25 sccm. An induction furnace was used for heating the graphite susceptor to temperatures of 1100 and 1300 °C for 1.0 h. Thus a large yield product with white color can be obtained. Fig. 51 displays the SEM images of boron nitride nanosheets grown at 1100 and 1300 °C. By controlling the synthesis and chemical reaction parameters, the thickness of the BN nanosheets can be adjusted in a range of 25–50 nm.

LCVD has been utilized to fabricate the 2D NSMs. For instance, Guan et al. [265] using a LCVD to produce 2D linear arrays of  $\text{ZnO}$  nanoparticles on a silicon substrate (Fig. 52). In a fabrication of 2D linear arrays of  $\text{ZnO}$  nanoparticles, a series of consecutive steps is involved in the synthesis and alignment of  $\text{ZnO}$  nanoparticles. First, a Lloyd's mirror arrangement was employed to produce two types of periodic nanostructure, i.e., nanoprotuberances. Then, the nanostructured substrate was laser irradiated at a fluence of  $60 \text{ mJ cm}^{-2}$  in the presence of the metall-organic precursor gas diethylzinc. The gas pressure and the number of laser pulses were  $2 \times 10^{-3}$  Torr and 10,000, respectively. The synthesis of single-crystalline 2D NSMs are much more difficult via LCVD. Therefore, little research has been done to establish the impact LCVD on synthesis of 2D NSMs.

Laser pyrolysis allows us to the easy synthesis of a 2D NSM. For example, Combemale et al. [266] fabricated the 2D zirconium carbide ( $\text{ZrC}$ ) nanosheets by laser pyrolysis. In their typical synthesis process of  $\text{ZrC}$  nanosheets, carburization of tetragonal zirconia/free carbon nanocomposites was fabricated by laser pyrolysis method using zirconium but oxide as precursor and ethylene as sensitizer gas. Then, obtained products were annealed at 1600 °C. Fig. 53 shows a TEM image of a single  $\text{ZrC}$  nanosheet. As shown in Fig. 53, the final  $\text{ZrC}$  grain size was ~35 nm, showing nanosheet  $\text{ZrC}$  nanograin oriented in the (110) direction.

Consequently, all above results suggested that the chemical process is a simple and very useful method for synthesis and fabrication of 2D NSMs. The morphology, particle size, and metallic composition of the 2D NSMs can be tuned based on the precursor solutions, substrate materials, and deposition conditions.

#### 4.4. Synthesis of 3D NSMs

##### 4.4.1. Synthesis of 3D NSMs by physical processes

In recent years, with the progress of nanotechnology, there has been increasing interest in the synthesis of 3D NSMs (for instance spring-like nanocoils, ball-like nanodendritic structures, and nano-flowers) because they are exhibit newer and/or better physical/chemical properties [267–270]. Concerning the fabrication of these nanoarchitectures, evaporation technique, sputtering technique, lithography process, hot plasma, cold plasma, spray pyrolysis, inert gas phase condensation technique,

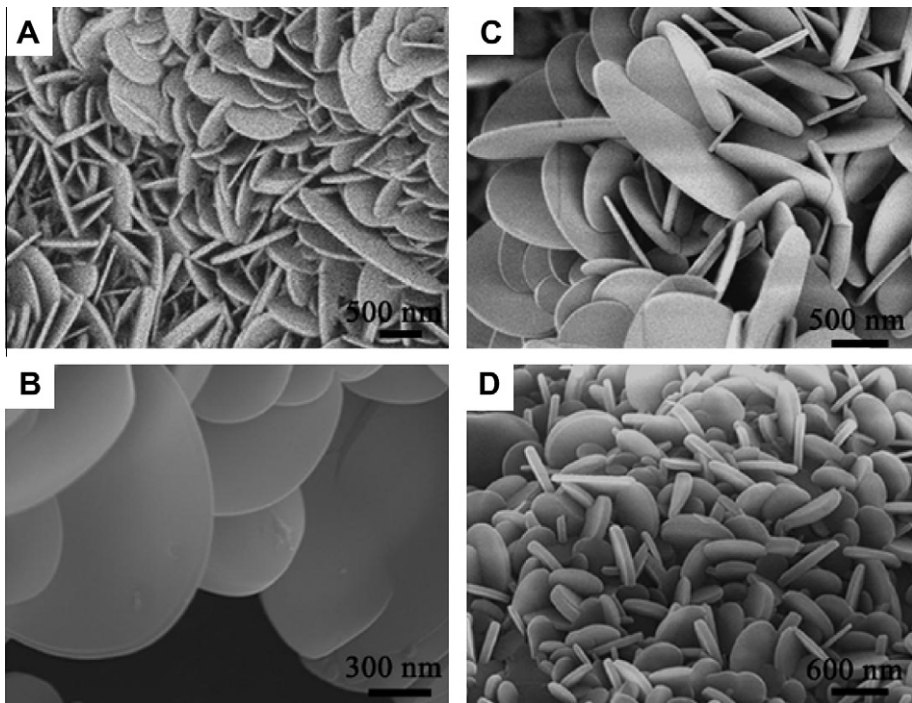


**Fig. 51.** Plan-view SEM images of 2D boron nitride nanosheets grown at (A–C) 1300 °C and (D) 1100 °C. Reprinted from Ref. [264] with permission of ACS Publishers.

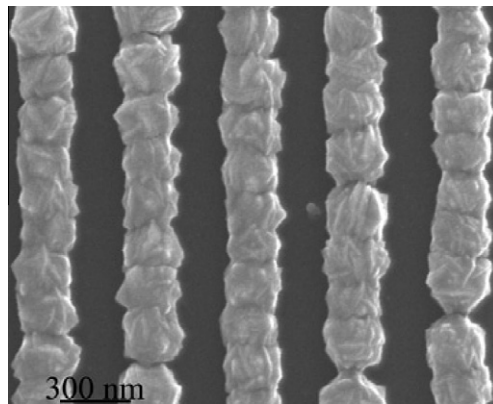


**Fig. 52.** SEM images of 2D linear arrays of ZnO nanoparticles. Reprinted from Ref. [265] with permission of IOP Publishing Ltd.

pulsed laser ablation, mechanical deformation technique, and sonochemical reduction are generally used to control their nucleation, growth and alignment. Zhang et al. [271] used a thermal evaporation technique to synthesize aligned 3D single-crystal Cr nanostructures onto a silicon substrate. A VEECO 770 thermal evaporating system was used for the synthesis. The pure Cr pellets (99.99%) were used as the source materials and an alumina crucible was used as the source holder. Tungsten filament was employed to thermally heat the source holder. The silicon sample is mounted into a movable holder

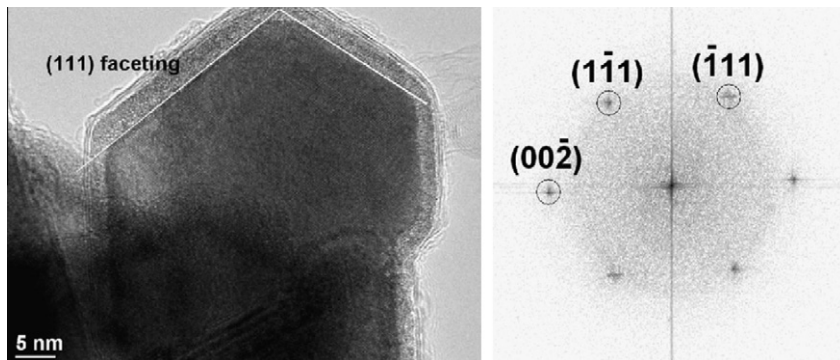


**Fig. 53.** TEM image of 2D ZrC nanosheets, together with the corresponding indexed fast Fourier transform. Reprinted from Ref. [266] with permission of Elsevier.

inside the vacuum chamber. The incident angle of Cr vapor flux with respect to the silicon sample surface was fixed at  $88^\circ$ . The gap between the sample and the source holder was  $\sim 18$  cm. Cr was evaporated by applying a constant current of  $23$  A, and a vacuum level of  $7 \times 10^{-6}$  mbar. The deposition rate was fixed at  $5 \text{ \AA s}^{-1}$ . The length of 3D Cr nanostructures is  $\sim 2 \mu\text{m}$ . They also reported that the morphology, shape and size of the resulting nanostructures could be manipulated via synthesis conditions. Abdulgafour et al. [272] also used the thermal evaporation method to synthesis 3D ZnO nano-flowers/Si. For the synthesis of 3D ZnO nano-flowers/Si, the Si sample was ultrasonically cleaned and placed at the top of an alumina boat with the polished faces toward the Zn powder. Then, the boat was inserted to a quartz tube furnace and furnace was slowly ramped from  $400^\circ\text{C}$  to  $850^\circ\text{C}$  with argon and oxygen flowing. The flow-rate of  $250 \text{ sccm}$  was maintained for 1 h.

The sputtering technique is becoming an increasingly attractive method for the synthesis of nanostructures because it allows for the precise control of surface morphology. For example, Wang et al. [273] used a magnetron sputter technique to fabricate aligned 3D Cu nanostructures onto a Si substrate. The deposition of 3D Cu nanostructures was performed in an ultrahigh vacuum glancing angle magnetron sputter deposition system with a base pressure of  $10^{-9}$  Torr. Then, sputtering was performed in  $2 \text{ mTorr}$  pure Ar using two Cu targets, placed at an angle of  $180^\circ$  with respect to each other and with their surfaces being perpendicular to the substrate surface. They also reported that the large incident angle assists the formation of Y-shaped branched structures because of atomic shadowing. In their experimental study, the average incident angle,  $\theta$ , is controlled by the relative positions of the targets, the substrate and a collimating plate, and was chosen to be  $84^\circ$ . During the deposition process, the substrate was constantly rotated with a speed of  $60 \text{ rpm}$  so that incident atoms arrive at the substrate from azimuthal angles. No external substrate heating was used. Fig. 54A shows the morphology of the as-prepared 3D Cu nanostructures with diameter of  $\sim 200 \text{ nm}$ . As shown in Fig. 54B, the obtained 3D Cu nanostructures exhibit various orientations. It can be classified into three categories: Y-shaped  $\{110\}$  nanorods, single crystal  $\{111\}$  and  $\{001\}$  nanorods, and polycrystalline nanorods.

Lithography is a simple, inexpensive, high-throughput, alternative routine for creating periodic 3D nanostructure arrays. Over the past decade, large-area 3D nanostructure arrays have been successfully fabricated by lithography approach [274–276]. Xu et al. [275] fabricated 3D free-standing, pyramidal, metallic microstructures by using a combination of conventional photolithography/soft lithography and etching techniques. The base dimensions of 3D metallic, pyramidal microstructures of  $1\text{--}2 \mu\text{m}$ , wall thicknesses of  $\sim 100\text{--}200 \text{ nm}$ , and tip-curvature radius of  $\sim 50 \text{ nm}$ . Recently, Zhang et al. [276] used a stepwise colloidal lithography to stepwise grow highly ordered multiplex quasi-three-dimensional grids of metallic one-dimensional nanostructures, e.g., nanowires and nanorods. Details about the fabrication of 3D grids of multiplex zigzag nanowires by angle-resolved colloidal lithography method are shown in Fig. 55. As shown in Fig. 55, the 3D nanostructures are successfully made by colloidal lithography method. Thus, the stepwise angle-resolved colloidal lithography method has been

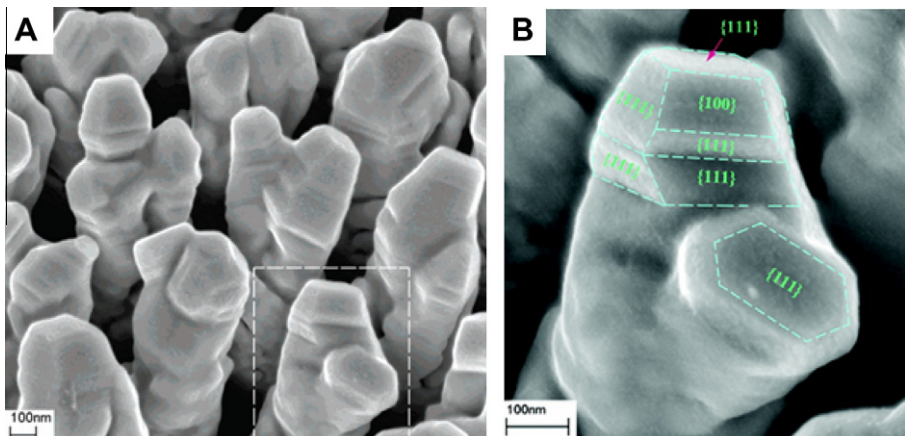


**Fig. 54.** SEM morphologies of 3D Cu nanostructures (A) and zoom-in region (B). The broken lines and labels in (B) are drawn to help visualize the facets. Reprinted from Ref. [273] with permission of ACS Publishers.

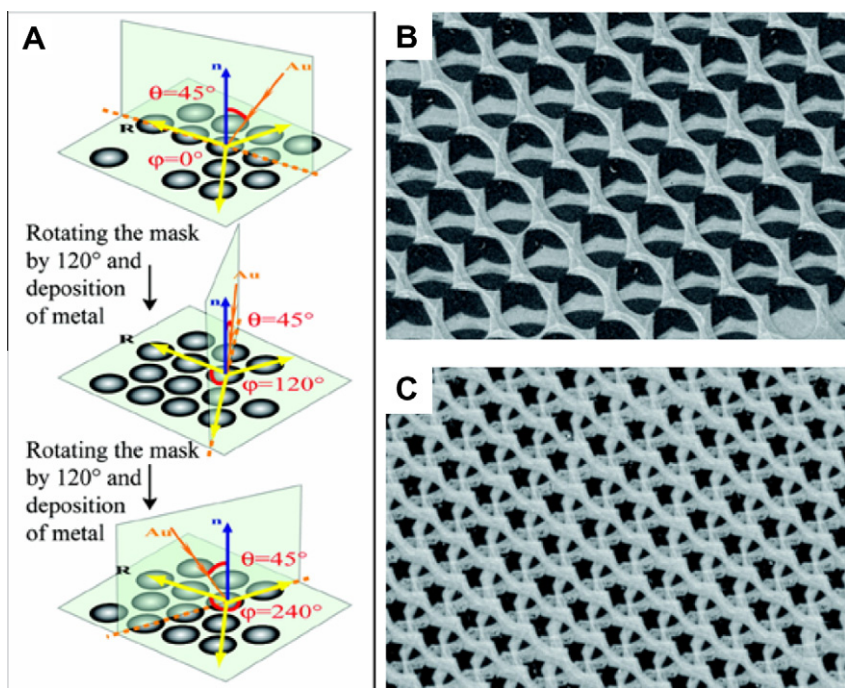


**Fig. 55.** (A) Schematic illustration of synthesizing 3D grids of multiplex zigzag nanowires via a stepwise rotation of the colloidal masks by  $120^\circ$  with respect to the reference vector ( $R$ ) between nearest-neighboring spheres over the course of metallic vapor deposition. The incidence angle between metal vapor and the reference vector ( $R$ ) is set to  $\varphi = 0^\circ$ . SEM images of 3D grids of multiplex zigzag nanowires formed via stepwise depositing gold, silver, and nickel at  $\varphi = 0^\circ$ ,  $\varphi = 120^\circ$ , and  $\varphi = 240^\circ$  using close-packed polystyrene sphere monolayers as masks are shown. The structure acquired through two and three deposition processes are displayed in (B) and (C), respectively. Reprinted from Ref. [276] with permission of ACS Publishers.

developed for fabrication of sophisticated 3D nanostructures with defined vertical and lateral heterogeneity.

Lei et al. [64] fabricated the 3D urchin-like nanostructured AlN in DC arc plasma via the direct reaction between Al vapor and N<sub>2</sub> gas. In the plasma system, the process of nitridation involves the evaporation of Al, decomposition of N<sub>2</sub>, and nucleation of AlN. The formation of 3D urchin-like nanostructured AlN is optimized by the reaction time and the pressure of N<sub>2</sub>. After growth for 100 min, the whole substrate is coated by a gray-colored crust. The synthesized 3D urchin-like nanostructured AlN (Fig. 56) is composed of many micro-daggers with sharp tips and lengths of up to several micrometers and widths of 0.5–2 μm.

Zhang et al. [277] prepared the vertically aligned single-walled carbon nanotubes (SWNTs) by a conventional 4-in. thermal CVD system with an inductively coupled rf. The Fe films coated on SiO<sub>2</sub>/Si is used as a substrate. During vertically aligned SWNTs growth, the compositions of CH<sub>4</sub>/H<sub>2</sub>/O<sub>2</sub> gases in the tube furnace are ~66%, ~12%, and ~1%. Ar gas ~21% is used as a carrier gas with a total pressure of 0.3–0.4 Torr. The gas flow rates of CH<sub>4</sub>/H<sub>2</sub>/O<sub>2</sub> are 160 sccm/30 sccm/2.4 sccm. The percentage of partial pressures of different gases followed CH<sub>4</sub>:H<sub>2</sub>:O<sub>2</sub> = 66%:12%:1% (the rest is Ar). The RF plasma was generated at a power of 60–70 W for 10–30 min for vertically aligned SWNTs growth. Hence, hot and cold plasma methods [276–279] are a simple and powerful technique to form 3D NSMs on desirable substrate (including metals and plastics) with strong interfacial adhesion.

Recently, several groups have reported the fabrication of 3D NSMs by spray pyrolysis method [62,280,281]. Zhang et al. [281] created a 3D hollow spherical architecture with single-crystal aluminum borate nanowires as building blocks, which are in situ formed in liquid droplets by a spray pyrolysis technique. The pyrolysis experiment is carried out in flowing argon at 1200 °C. Their results also suggested that it is possible to directly grow curved, hollow, and 3D-ordered assemblies built from 1D nanocrystal through spray pyrolysis method. Wang et al. [62] fabricated the highly compressed and regular coiled carbon nanotubes (CCNTs) by spray pyrolysis in the presence of cupric acetate and ethanol. The CCNTs were synthesized at a temperature of 850 °C. The obtained CCNTs products were in high quality and high yield and were composed of graphitic layers and fine regular coils (Fig. 57). In addition, the CCNTs had a uniform shape with a sharp radius of curvature and a small coil pitch

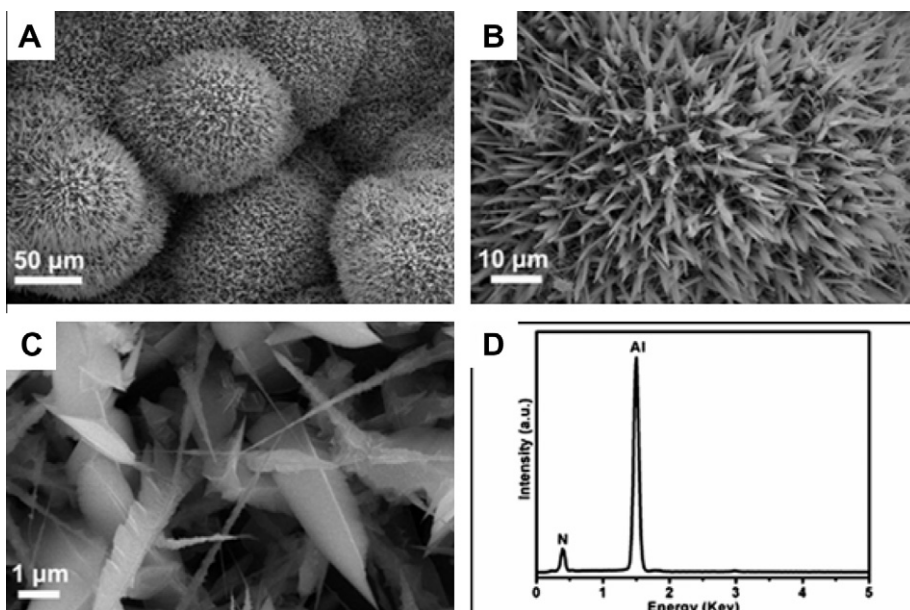


**Fig. 56.** (A) SEM image of 3D urchin-like nanostructured AlN, (B) low-magnification SEM image of 3D urchin-like nanostructured AlN, (C) high-magnification SEM image of 3D urchin-like nanostructured AlN, (D) EDX spectrum of the 3D urchin-like nanostructured AlN. EDX spectrum will display that the presence of Al and N in 3D urchin-like nanostructured AlN. Reprinted from Ref. [64] with permission of ACS Publishers.

(Fig. 57). The external diameter and the inner diameter of the CCNTs are about 30–50 nm and 10–20 nm, respectively. Thus, the spray pyrolysis method is also a powerful technique for synthesis of 3D NSMs.

Al-Sharab et al. [182] prepared the 3D  $\text{WO}_{2.9}$  nanoballs onto an un-cooled substrate by using an IGC method in the TEM. The 3D  $\text{WO}_{2.9}$  nanoballs were formed by large aggregates (2–10  $\mu\text{m}$  diameter) of faceted nanoparticles (50–200 nm diameter) when the water cooling to the substrate was turned off. The faceted nanoparticles aggregation may be attributed to the partial sintering when deposition and substrate temperatures were increased due to the absence of water cooling. The morphology of the resulting nanostructures was influenced by the substrate temperature and location from the evaporative source [182]. Consequently, the IGC method is potentially an attractive method for the production of different kinds of NSMs.

With the pulsed laser ablation method, 3D nanoporous materials are synthesized by the ablation of one or more targets illuminated by a focused pulsed-laser beam. Tavangar et al. [282] used pulsed laser ablation method to deposit 3D porous  $\text{SiO}_2$  nanostructures onto Si substrate. In typical fabrication of 3D porous  $\text{SiO}_2$  nanostructures, the silicon targets are placed behind a glass acceptor. Then, femtosecond laser pulses pass through the transparent acceptor and hit the bulk donor. Thus, a large quantity of nanoparticles ablates from the donor and then aggregates and forms a 3D porous  $\text{SiO}_2$  nanostructure on the transparent acceptor. Fig. 58 shows the energy-dispersive X-ray spectroscopy (EDX) spectrum for the pure Si and 3D porous  $\text{SiO}_2$  nanostructures. EDX spectrum shows the oxygen concentration in the porous structure which is ascribed to the oxidation of ablated material due to the presence of oxygen in an ambient atmosphere.

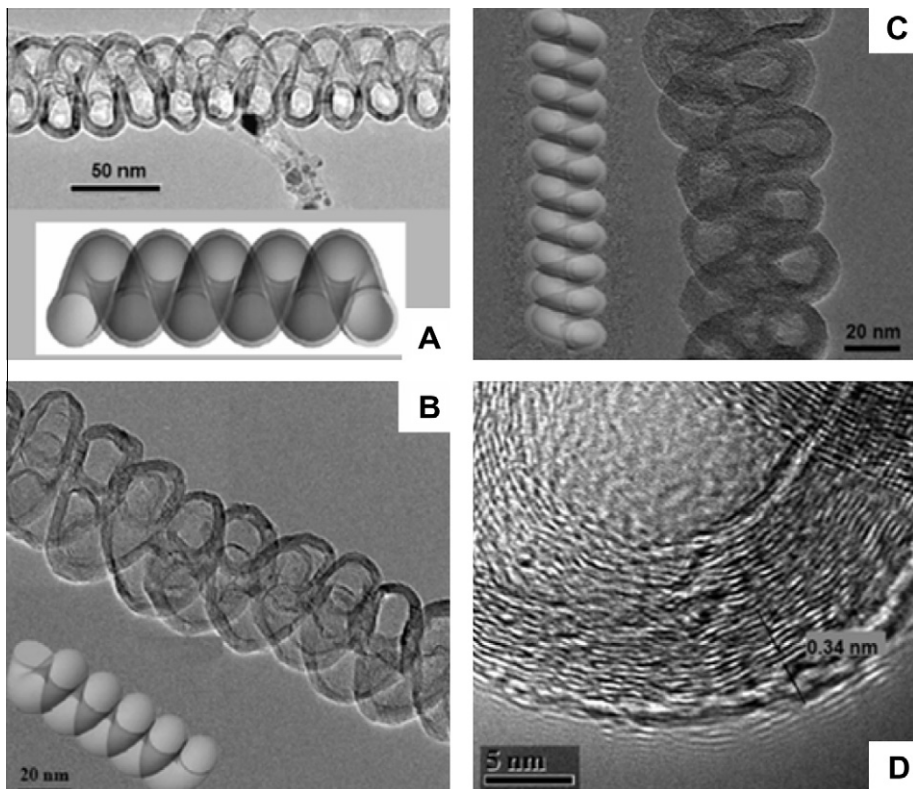


**Fig. 57.** (A–C) Typical TEM images of CCNTs and their 3D models (insets) and (D) HRTEM image of the individual tube wall. Reprinted from Ref. [62] with permission of ACS Publishers.

The sonochemical process, which is facile and operated under ambient conditions, has been proven to be a useful route for the preparation of 3D NSMs with unusual properties [283]. Zhu et al. [283] fabricated the 3D EuF<sub>3</sub> nanoflowers via sonochemical route employing the reaction of Eu(NO<sub>3</sub>)<sub>3</sub> and KBF<sub>4</sub> under ambient conditions. The sonication process not only accelerates the reaction between the raw materials but also greatly enhance the nucleation and growth activity of EuF<sub>3</sub>. Fig. 59 shows the SEM images of 3D EuF<sub>3</sub> nanoflowers at various magnifications. The 3D EuF<sub>3</sub> nanoflowers are spherical with an average diameter between ~0.9 and ~1.0 μm, and the average thickness of the petals is ~0.14 μm. The high-magnification SEM picture (Fig. 59C) represents that the surface of the flower is very smooth. EDX shows that the nanoflowers are composed of Eu and F (Fig. 59D).

More recently, Mao et al. [284] fabricated the 8-hydroxyquinoline aluminum (Alq<sub>3</sub>) nanoflowers via a facile and fast sonochemical route. The Alq<sub>3</sub> nanoflower was mainly composed of nanobelts. The thickness, average widths and length are ~50 nm, ~200 nm, and ~10 μm, respectively. Fig. 60 shows a schematic representation of the synthesis and formation mechanism of Alq<sub>3</sub> nanoflowers by the sonochemical route. The three major steps are involved in the formation of Alq<sub>3</sub> nanoflowers: first acoustic induced formation of nuclei, which led to produce primary nanoparticles. Secondly, acoustic-induced fusion of these primary nanoparticles accompanying oriented attachment to form the nanobelts. Third, the individual nanobelts were further attached side-by-side to assemble into bundles, accompanying an Ostwald ripening process [284]. On the basis of the above results, we can say that the sonochemical synthesis route is easily controllable and well reproducible and feasible to develop novel 3D NSMs.

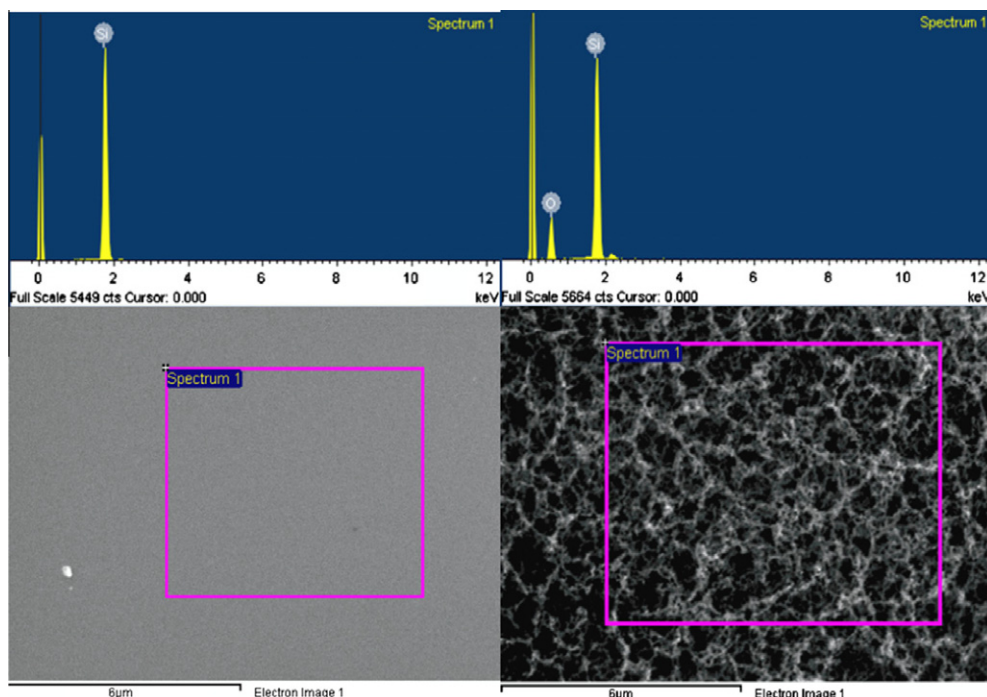


**Fig. 58.** EDX spectrum for the pure Si (left) and nanoporous SiO<sub>2</sub> deposited on a Si substrate (right). Reprinted from Ref. [282] with permission of IOP Publishing Ltd.

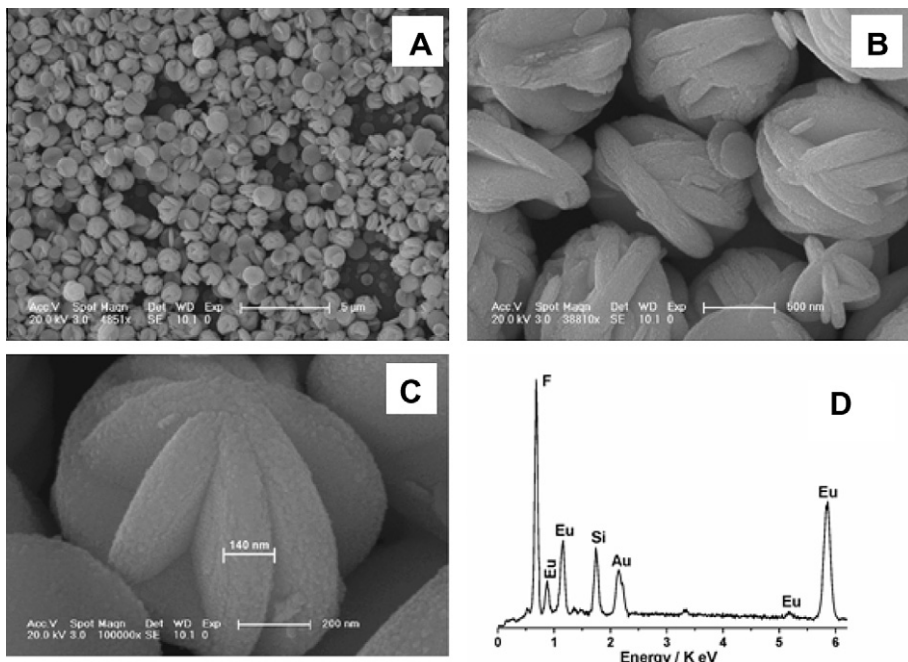


**Fig. 59.** SEM images of 3D  $\text{EuF}_3$  nanoflowers at various magnifications (A–C) and (D) EDX of the  $\text{EuF}_3$  nanoflowers. Reprinted from Ref. [283] with permission of ACS Publishers.

#### 4.4.2. Synthesis of 3D NSMs by chemical processes

Template-assisted growth methods such as porous aluminum oxide templates [285], zeolites [286], and soft templates like polymer [287,288] and organic surfactants [289], have been developed for preparing 3D NSMs. Zhong et al. [290] systematically reported that template-assisted growth process for a large scale production of  $\text{Cd}_4\text{Cl}_3(\text{OH})_5$  microflowers. In a typical synthesis of nanoroses, first the glass substrate was cleaned by using the DI water, acetone, and dried with nitrogen. Next, the cleaned glass substrates were immersed in the  $\text{CdO}$  solution and then were annealed at 100 °C for 1 h and at 200 °C for 1 h. The  $\text{CdO}$  sol coated glass was immersed in the mixed solution of  $\text{CdCl}_2$  (0.022 mol L<sup>-1</sup>) and  $\text{C}_6\text{H}_{12}\text{N}_4$  (0.033 mol L<sup>-1</sup>) in an autoclave. The autoclaves were moved to an oven at 95 °C. After the 3 h, the autoclaves were removed from the oven and cooled to room temperature. Finally, the sample is taken out of the solution, rinsed with DI water and ethanol to remove contaminants from the reaction solution, and dried with  $\text{N}_2$  gas.

Yamauchi's group used a simple approach to the rational synthesis of mesoporous Pt based on the LLC template [291–294]. The main process is formation of LLC and subsequent reduction of the plat-

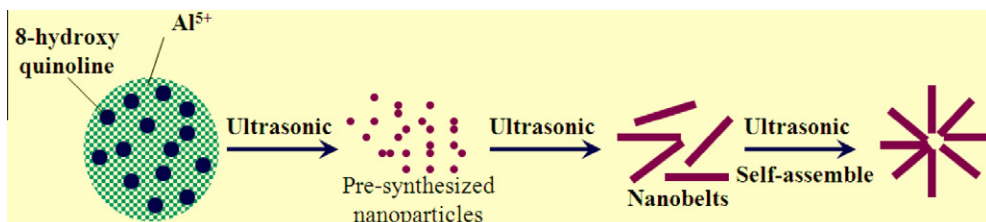


**Fig. 60.** A schematic diagram of the growth mechanism of  $\text{Alq}_3$  nanoflowers. Modified from Ref. [284].

inum complex dissolved in aqueous phases in LLC. The typical synthesis of the 3D mesoporous Pt underwent the following steps [291]. A first initiator solution was prepared by mixing DI water, hydrogen hexachloroplatinate(IV) hexahydrate, poly(styrene-*b*-ethylene oxide) block copolymer, and tetrahydrofuran as volatile solvent. Then, the initiator solution was coated onto an indium tin oxide (ITO) substrate by drop method. LLC film was formed over the entire area of the substrate via the evaporation of tetrahydrofuran. Then the Pt was deposited on the LLC-modified ITO substrate by electrochemical method. Electrochemical deposition was carried out at a fixed potential ( $-0.10$  V vs. Ag/AgCl). Finally, the deposited Pt was cleaned with tetrahydrofuran, ethanol, and DI water to extract the undeposited Pt species and the diblock copolymer. The pore sizes are controlled by using appropriately architected block copolymers. Wang et al. [61] prepared a 3D dendritic platinum nanostructures by simply mixing  $K_2PtCl_6$  aqueous solution and poly(vinyl pyrrolidone) at a constant  $30$  °C for 1 h in the presence of ascorbic acid. TEM images of 3D dendritic Pt nanostructures are shown in Fig. 61. The lower magnification image (Fig. 61 A) indicates that the Pt nanostructures were well-dispersed as individual spherical entities appeared to be 3D complex nanodendrites, and strikingly uniform in morphology. In addition, high-magnification TEM image (Fig. 61 B) shows that the well-oriented 3D dendritic Pt nanostructures with the surface packed by highly assembled dendritic feelers branching in various directions.

Electrochemical process is also considered as a real deposition method to grow the high quality 3D NSMs. One of the advantages of this technique is low cost. The instrument is very cheap and any maintenance is hardly required. More recently, one of the authors [295,296] used the facile electrochemical method to fabricate the 3D Pt nanoflowers. Under the typical bipolar pulse electrodeposition conditions, 3D Pt nanoflowers could be synthesized on the flat Si wafer and ordered Si nanocones substrate. Zhang et al. [297] fabricate the porous Pt nanoflowers with high surface areas onto a clean ITO by a facile, one-step and template-free electrodeposition method. Typical synthesis of porous Pt nanoflowers were carried out at room temperature in  $3.0$  mM  $H_2PtCl_6 + 0.5$  M  $H_2SO_4$  at  $-0.2$  V. Fig. 62 shows the SEM images of Pt nanoflowers under various conditions. These morphological changes clearly indicated that the shapes of the Pt nanoflowers are greatly affected by the times.

In recent years, electroless deposition is attracted substantial interest because of their use in facile fabrication of 3D ordered NSMs at low temperatures [298–303]. Yan et al. [301] fabricated the Cu dendritic nanostructures via electroless deposition. In a typical synthesis of Cu dendritic nanostructures, first copper chloride was mixed in a DI water/hydroperoxide solution and the pH value was fixed to 2.3 using acetic acid. Then, the cleaned zinc foil is immersed in the mixed solution and put into an autoclave. After that, the autoclave was sealed to an electric oven and the temperature was maintained at  $120$  °C for 4–18 h. The autoclave was cooled to room temperature. Finally, the resulting products were taken out, and the precipitate was collected, filtered off, and washed with water, then with absolute ethanol several times and dried in air at  $80$  °C for several hours. Gutes et al. [302] prepared the Ag dendrites on Al foil by electroless deposition (Fig. 63). The process is based on a redox process.

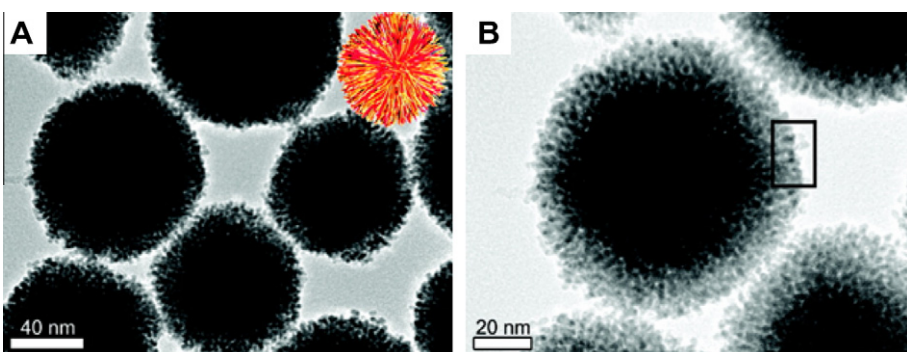


**Fig. 61.** (A) Low- and (B) high-magnification TEM images of the 3D dendritic platinum nanostructures. The inset of (A) is a picture of a Koosh ball. Reprinted from Ref. [61] with permission of ACS Publishers.

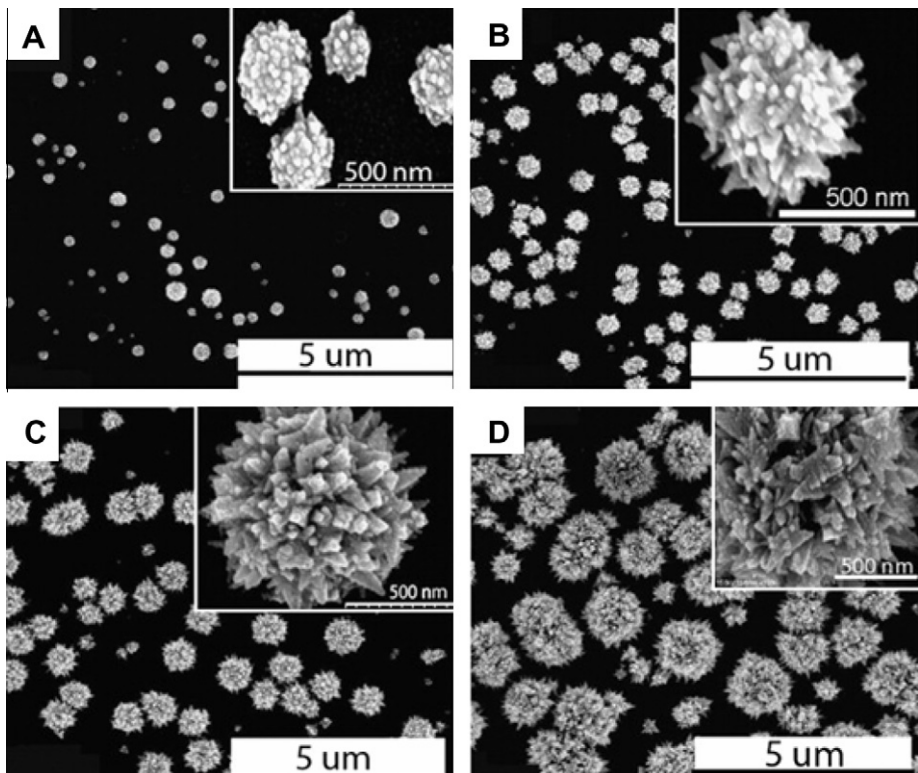


**Fig. 62.** SEM images of Pt nanostructures coated on ITO at different stages of formation: (A)  $t = 25$  s, (B)  $t = 400$  s, (C)  $t = 1000$  s, and (D)  $t = 4000$  s. Insets are the higher magnification SEM images. Reprinted from Ref. [297] with permission of Elsevier.

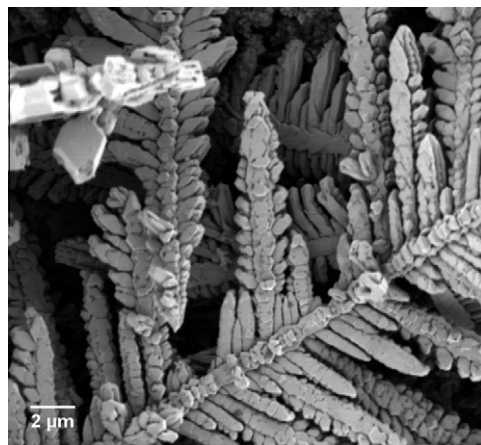


**Fig. 63.** SEM image of Ag dendrites formed on the surface of Al foil. Reprinted from Ref. [302] with permission of ACS Publishers.

In redox process the reductant transfers electrons to the oxidant. Thus in the reaction, Al is oxidized while Ag ions are reduced, yielding a final silver dendritic structure that offers a high surface area-

to-volume ratio. Wu et al. [303] reported the fabrication of vertically aligned Si rice-straw-like arrays by electroless deposition in the presence of HF-H<sub>2</sub>O<sub>2</sub> as an etching solution. Thus, the electroless deposition process is another chemical method for fabrication of 3D NSMs.

The hydrothermal technique can be used for direct synthesis of complex 3D NSMs. For example, Zhou et al. [304] prepared the nanosheet-based 3D zinc hydroxide carbonate microspheres by a hydrothermal process. For the synthesis of nanosheet-based zinc hydroxide carbonate microspheres, zinc nitrate hexahydrate and urea were used as starting materials. The average diameter of ZnO microspheres is ~15 μm, and the length of a ZnO nanosheets, which is made up of thin multilayered sheets is ~7 μm. They also found the dissociation–deposition mechanism using in situ formation of nanosheet-based 3D zinc hydroxide carbonate microspheres. Cheng et al. [305] also used the hydrothermal technique to make the ZnO nanostructures on SnO<sub>2</sub> backbone nanowires at 95 °C. The ZnO nanorods were epitaxially grown on the SnO<sub>2</sub> backbone nanowire. The hybrid SnO<sub>2</sub>–ZnO nanostructures exhibit an enhanced near-band gap emission compared to that of SnO<sub>2</sub> nanowires. Very recently, Wang et al. [306] used the hydrothermal and annealing process to fabricate the 3D crystalline anatase TiO<sub>2</sub> hierarchical nanostructures (Fig. 64). The 3D crystalline anatase TiO<sub>2</sub> hierarchical nanostructures morphologies were obtained by self-assembly of several tens of thin petals. The hierarchical nanostructures exhibited enhanced ethanol sensing properties.

The solvothermal method is very attractive due to its flexibility and efficiency for the fabrication of 3D NSMs with desired properties [307–309]. Through this process, the precursor is used up and transformed into desired nanostructures. Thongtem et al. [309] used the solvothermal process to fabricate the flower-like 3D CuS nanostructures. In a typical synthesis, CuCl<sub>2</sub>·2H<sub>2</sub>O and CH<sub>3</sub>CSNH<sub>2</sub> were mixed in ethylene glycol, and followed by the addition of NaOH to adjust the pH. Then, the reactions carried out in an acid digestion bomb. Zhao and Miyauchi [307] prepared the tungstic acid hollow spheres via a non-aqueous and solvothermal technique. This process is based on a direct reaction (WCl<sub>6</sub> + urea + ethanol) under mild conditions. They also report that the morphology and size of the resulting products can be controlled by changing the urea amount, ethanol amount, reaction temperature, reaction time, and pH value. More recently, Huang et al. [310] synthesized the mesoporous and polycrystalline flower-like SnO<sub>2</sub> nanostructures (Fig. 65) via annealing of sol–gel films. In a typical synthesis of flower-like SnO<sub>2</sub> nanostructures, flower-like SnS<sub>2</sub> is prepared by the sol–gel process. Then, the SnS<sub>2</sub> NSMs are put in a quartz boat, and placed at the center of horizontal tube. Finally, flower-like SnS<sub>2</sub> nanostructures are calcinated at 500–600 °C for 3 h.

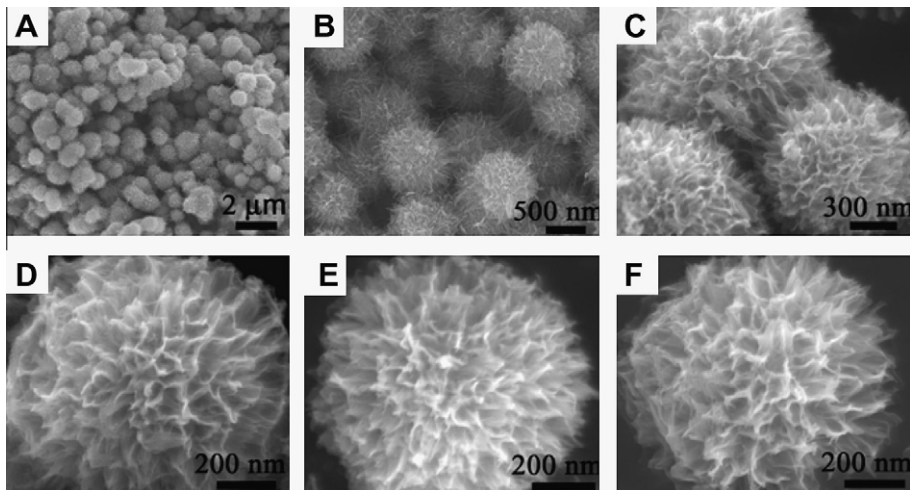


**Fig. 64.** (A and B) Low-magnification SEM images of 3D crystalline anatase TiO<sub>2</sub> hierarchical nanostructures. (C–F) High-magnification SEM images for individual hierarchical nanostructures. Reprinted from Ref. [306] with permission of ACS Publishers.

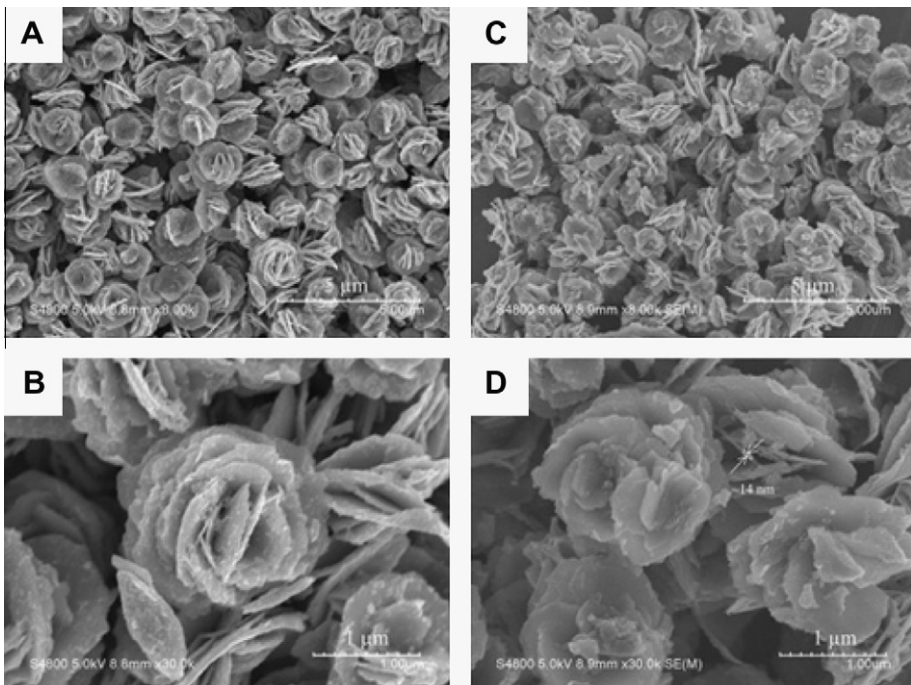


**Fig. 65.** (A) Low- and (B) high-magnification SEM images of  $\text{SnS}_2$  nanostructures. (C) low- and (D) high-magnification SEM images of  $\text{SnO}_2$  nanostructures. Reprinted from Ref. [310] with permission of Elsevier.

CVD is an economically attractive method to grow 3D NSMs such as aligned nanowalls and nanowires [311–314]. Very recently, our group has fabricated the 3D graphitic nanosheets using a facile CVD in the presence of methane gas [314]. Fig. 66 shows the SEM (A) and AFM (B) images of synthesized 3D graphitic nanosheets. The thickness of graphitic nanosheets ranged from  $\sim 1$  nm to  $\sim 5$  nm. Chan et al. also used the facile CVD process to fabricate the highly oriented, single-crystal Ni nanowire arrays onto the  $\text{SiO}_2/\text{Si}$  substrates at a temperature of  $650\text{ }^\circ\text{C}$ . The physical property of Ni nanowire confirms their excellent crystalline quality, high material purity, and represents their suitability for various wide-ranging applications. Thus, CVD is also a more powerful and effective technique for synthesis of oriented NSMs.

Generally, LCVD techniques are used for synthesis of carbon material [315–317]. Normand et al. [318] fabricated the vertically oriented CNTs onto flat  $\text{SiO}_2/\text{Si}$  substrate by a LCVD technique in the presence of 20%  $\text{C}_2\text{H}_2/\text{H}_2$  gas. The vertically oriented CNTs growth was carried out in an ultra high vacuum CVD chamber with ultra high vacuum base pressure lower than  $10^{-7}\text{ Pa}$ . The Fe particles are embedded in a protective carbon matrix and used as catalyst to grow CNTs. The electron field emission of vertically oriented CNTs/ $\text{SiO}_2/\text{Si}$  substrate exhibits an interesting behavior with a low turn-on voltage at around  $1\text{ V }\mu\text{m}^{-1}$ .

Bystrzejewski et al. [319] used the laser pyrolysis to prepare the 3D carbon nanospheres (CNSs). Anthracene is used as a starting material to make CNSs. A relatively low-power continuous  $\text{CO}_2$  laser beam is used to decompose anthracene in the presence of  $\text{N}_2$  gas. The laser beam energy partially breaks the C–H bonds in the anthracene molecules and as the newly created large radicals aggregate, CNSs are formed. The diameters of CNSs are between 100 nm and 400 nm. In addition, by changing the temperature and concentrations of the active species in the reaction zone, it is possible to control the resulting morphology of products. Thus, laser pyrolysis methods have been widely used in the fabrication of different kinds of 3D NSMs.

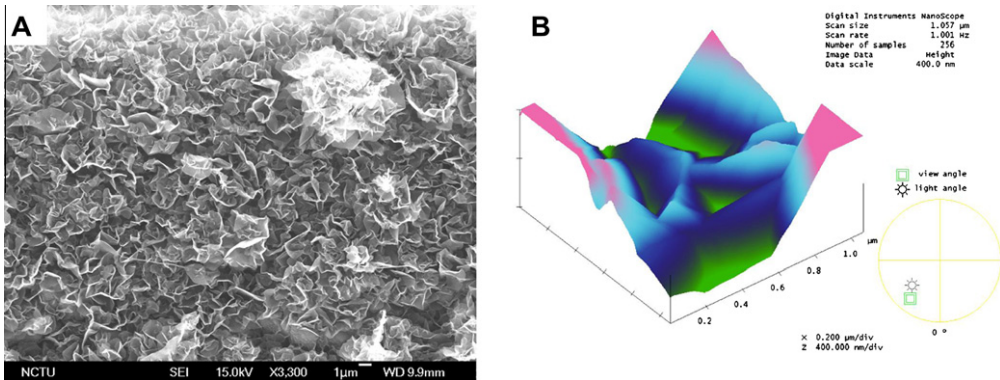


**Fig. 66.** Plan-view (A) SEM and (B) AFM images of the 3D graphitic nanosheets.

## 5. Applications of 0D, 1D, 2D and 3D NSMs

### 5.1. Fuel cells

#### 5.1.1. Introduction

Fuel cell is one of the EED which can continuously convert the chemical energy of fuels directly into electrical energy with high efficiency and low emission of pollutants, which may help to reduce the dependence from fossil fuels. The operation without combustion, can contribute to reduce environmental impacts. Their science and technology have already been extensively reported in many review papers and articles [320–324], to which the interested reader is referred for more details. In brief, a fuel cell consists of three active components. The main active components are fuel electrode (anode), oxidant electrode (cathode). The proton conducting solid membrane used as electrolyte, is sandwiched between the anode and cathode electrodes (Fig. 67).

Although the technology of such fuel cells was developed to an extent, some problems remain unclear and only their solution can result in wide-scale commercialization of fuel cells, especially as the efficient current sources for portable devices. The most important problem is the development of efficient catalysts, which would provide the long-term operation of fuel cells without sacrificing their characteristics. The CO poisoning intrinsic to Pt based cathodes pose a further barrier to fuel cell de-

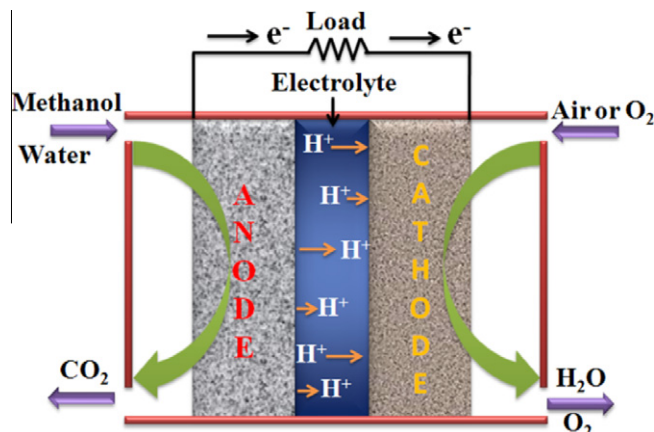


**Fig. 67.** Schematic diagram of the DMFCs.

vices. Hence it is important to open up new methods for making low cost and effective electrocatalysts. It is well known that the catalytic activity attainable depends significantly on the size of the Pt catalysts and their support. However, there are two routes to overcome this problem. First, the direct synthesis of novel 0D, 1D, 2D, and 3D NSMs (Pt or Pt alloy catalysts) with high surface area for fuel cell devices. Secondly, the synthesis of novel NSMs with high surface area as a support of Pt or Pt alloys catalysts for fuel cell devices. By considering both types of nanostructures, we will discuss these NSMs in more detail in the following sections.

### 5.1.2. 0D NSMs

During the past decade, the clusters stabilizing Pt nanoparticles have attracted a considerable interest as catalysts for low temperature fuel cell devices, such as polymer electrolyte fuel cells (PEMFCs) and direct methanol fuel cells (DMFCs). The clusters stabilizing Pt nanoparticles are formed in order to maximize the active number of surface versus the inactive number of Pt bulk atoms. However, one of the major problems associated with the clusters stabilizing Pt catalysts are their stability in the acid environment of DMFCs and PEMFCs. This is because of after only 100 h of testing the reaction rate dropped to half in such fuel cell devices. During this process the CO-ads species were continuously formed, which strongly absorbs to the clusters stabilizing Pt active sites to poison the fuel cell performance devices.

Due to these problems of the clusters stabilizing Pt nanoparticles, researchers decided to investigate the bimetallic clusters and colloids with nanometer-scale dimensions for fuel cell device applications. There are two main reasons for using the bimetallic clusters and colloids with nanometer-scale dimensions, firstly, because they may serve as models for studying the formation of different alloy catalysts. Secondly, it is possible to save precious metal, such as Pt, by optimizing the synthetic conditions so that only very thin surface layers occur [325,326]. In most cases, Pt and Pt-based alloy nanoparticles are used in the form of small nanoparticles, since small size offers high surface area which is especially crucial for catalysis and fuel cell applications [327,328].

A very recent report by Tiwari et al. [329] showing perfect Pt nanocubes had much higher electrocatalytic activity and stability for methanol and ethanol oxidation than other nanostructures such as truncated Pt nanocubes, truncated Pt (cubes + tetrahedra) and spherical Pt nanoparticles. Wang et al. [328] reported the controlled synthesis of dendritic Au@Pt core–shell nanomaterials. The CTAB and ascorbic acid had played a very important role in the synthesis of dendritic Au@Pt core–shell nanoparticles. The dendritic Au@Pt core–shell showed enhanced electrocatalytic activity for methanol oxidation in acid medium with a comparison to conventional spherical Au@Pt core–shell and monometallic Pt nanoparticles. Chen et al. [330] synthesized the Co–Pt catalyst with a hollow sphere structure via a very simple thermolytic reaction. The Co–Pt hollow sphere catalyst showed the high surface area with a comparison to the pure Pt nanoparticle catalyst and Co–Pt nanoparticles (Fig. 68). In addition, the Co–Pt hollow sphere catalyst showed enhanced electrocatalytic activity for methanol oxidation with a comparison to the pure Pt nanoparticle catalyst and Co–Pt nanoparticles at the same Pt loading (Fig. 68).

### 5.1.3. 1D NSMs

In the last few years, attention has been shifted towards the synthesis of 1D NSMs because of their fundamental importance and potential applications in fuel cells. To date, 1D NSMs (such as nanowires, nanorods, nanobelts, and nanotubes) have been most extensively studied because of their simplicity in preparation and its improved catalytic properties as compared to bulk metallic materials [331–338]. Ksar et al. [336] fabricated the Pd nanowires in a hexagonal mesophase (as soft templates) by electron beam irradiation. They also reported that the average lengths of the Pd nanowires are controlled by the amount of co-surfactant that assists the reduction/growth processes. In addition, the electrochemical studies indicated that the Pd nanowires had a very good electrocatalytic activity and stability for ethanol oxidation. Liu et al. [337] prepared the nanoporous Pt–Co alloy nanowires by dealloying electrodeposited  $\text{Pt}_1\text{Co}_{99}$  nanowires in the presence of porous AAO membrane in a mild acidic medium (Fig. 69) and examined their electrochemical properties.

Fig. 70 compares the performance of the various electrodes toward methanol oxidation. In the CV scan, the anodic peaks in the forward scan and in the reverse scan are associated with methanol ox-

dation and removal of incompletely oxidized carbonaceous species (CO-like poisoning species) on the electrocatalysts. The catalyst tolerance against CO adsorption may be calculated by the ratio of the current density of the forward anodic peak ( $I_f$ ) to that of the reverse anodic peak ( $I_b$ ), ( $I_f/I_b$ ) [51,295,296,345]. For the Pt–Co nanowires (15 h), the ( $I_f/I_b$ ) ratio is higher than that of other electrocatalysts (Fig. 70A, B), indicating that the Pt–Co nanowires (15 h) had a superior tolerance against CO poisoning. In addition, as seen in Fig. 70, nanoporous Pt–Co alloy nanowires exhibit an enhanced electrocatalytic activity toward methanol oxidation (in comparison to state-of-the art Pt/C and PtCo/C catalysts).

Lu et al. [338] synthesized the nanoneedle-covered Pd–Ag nanotubes via a galvanic displacement reaction with Ag nanorods. Then, the electrocatalytic activity of Pd–Ag nanotubes toward formic acid

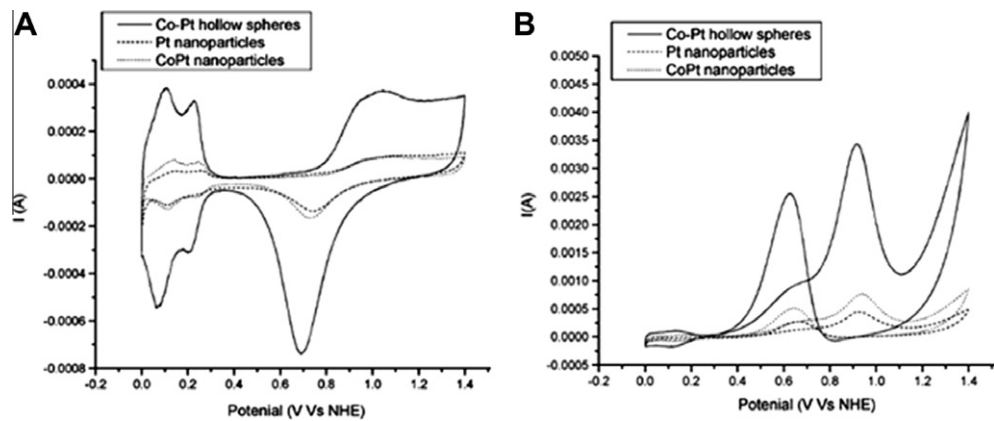


**Fig. 68.** (A) CVs of Co–Pt hollow spheres ( $\text{Co}_{32}\text{Pt}_{68}$ ),  $\text{Co}_{28}\text{Pt}_{72}$  nanoparticles, and Pt nanoparticles in a 0.5 M  $\text{H}_2\text{SO}_4$  solution; (B) CVs of Co–Pt hollow spheres ( $\text{Co}_{32}\text{Pt}_{68}$ ),  $\text{Co}_{28}\text{Pt}_{72}$  nanoparticles, and Pt nanoparticles in a 0.5 M  $\text{H}_2\text{SO}_4$  + 1 M methanol solution at a scan rate of 200 mV s<sup>-1</sup>. Reprinted from Ref. [330] with permission of ACS Publishers.

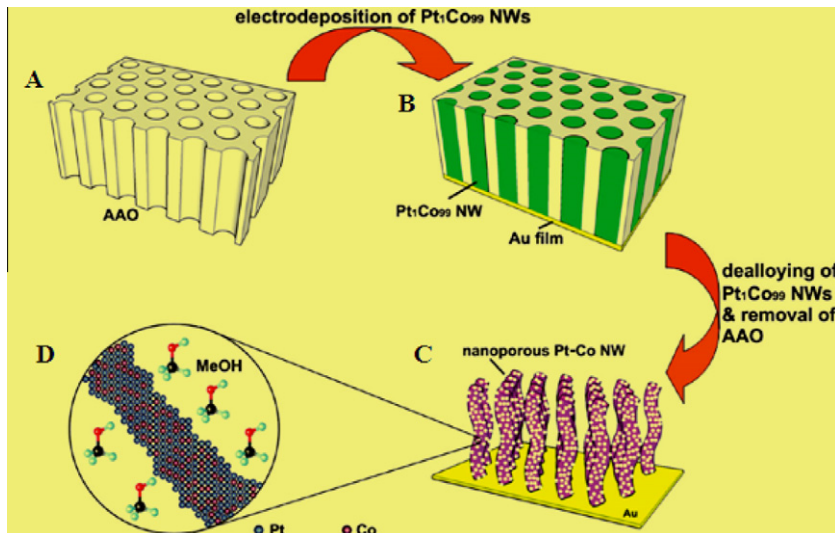


**Fig. 69.** (A–C) Schematic diagram explain the nanoporous Pt–Co nanowires fabrication process; (D) enlarged view of the ligaments. Reprinted from Ref. [337] with permission of ACS Publishers.

oxidation was studied by CV and electrochemical impedance spectroscopy (EIS). The Pd–Ag nanotubes show high electrocatalytic activity toward the formic acid oxidation in the CV and chronoamperometric studies. From EIS measurements, the charge-transfer resistance obtained on Pd–Ag nanotubes is also very good, suggesting the highly facilitated electron-transfer kinetics for formic acid oxidation at the Pd–Ag nanotubes. Much work has been done on fabrication of 1D NSMs by different groups. However, these 1D NSMs suffering from the high performance electrocatalytic activity is due to its low surface area as compared to 2D NSMs.

#### 5.1.4. 2D NSMs

2D NSMs such as junctions (continuous islands), branched structures, nanoprisms, nanoplates/nanosheets, nanowalls, and nanodisks are an especially promising form of nanoscale with a rare combination of extremely high specific surface area, exceptional thermal/electrical conductivity and stability [339,340]. The utilization of 2D NSMs as a support to anchor catalyst nanoparticles and facilitate electron transport opens up interesting new possibilities for designing and building of next generation catalysts for fuel cells. In addition, 2D NSMs can avoid aggregation and maintain high specific surface areas; these factors are important in increasing the accessibility of adsorbates to reactive sites [339,340]. Li et al. [339] fabricated the close-packed Au nanoprism thin films on the indium tin oxide coated glass substrates. Au nanoprisms are single crystalline, whose basal surfaces are atomically flat {111} planes and lateral surfaces are {110} planes. A small amount of Pt or Pd was deposited onto the Au nanoprism thin film electrodes and studies their catalytic properties. They noticed that the Pt

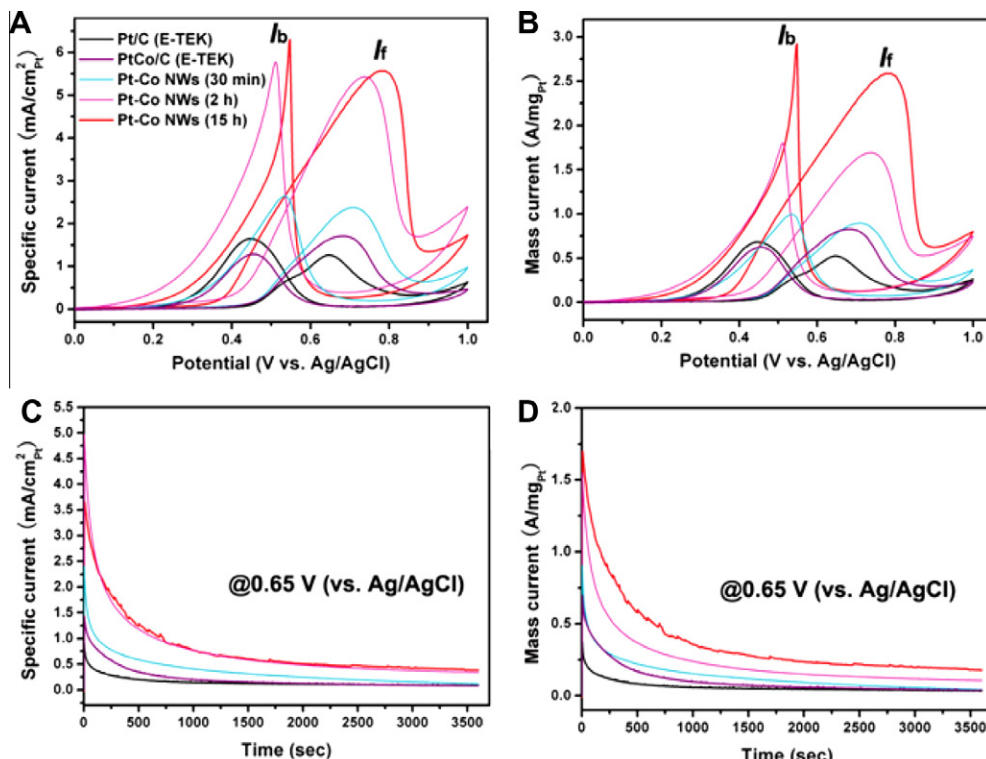


**Fig. 70.** Electrochemical performance of the nanoporous Pt–Co alloy nanowires dealloyed for 30 min, 2 h, and 15 h toward methanol oxidation. (A and B) CVs for methanol oxidation in 0.5 M  $\text{H}_2\text{SO}_4$  and 1 M  $\text{CH}_3\text{OH}$  solution at a scan rate of  $50 \text{ mV s}^{-1}$ . (C and D) CAs for methanol oxidation in 0.5 M  $\text{H}_2\text{SO}_4$  and 1 M  $\text{CH}_3\text{OH}$  solution at potential of 0.65 V. The CVs and CAs of commercial Pt/C and PtCo/C catalysts are included for comparison. Reprinted from Ref. [337] with permission of ACS Publishers.

on Au nanoprisms exhibited greatly enhanced catalytic activity toward the oxidation of methanol and much better CO poison resistance than commercial Pt-based catalysts (Fig. 71).

Wong's group [340] have synthesized Pd nanoplates array onto Au substrate by a facile electrochemical process. In this process, the Pd nanoplates array was fabricated at room temperature in a three-electrode cell containing 2 mM K<sub>2</sub>PdCl<sub>4</sub>, 100 mM NH<sub>3</sub>.H<sub>2</sub>O and 10 mM cetyltrimethyl ammonium bromide. A CV potential scan was applied to the working electrode over a range of 0.4 to -1.0 V (vs. SCE) with scan rate 100 mV s<sup>-1</sup>. The flat Pd electrode was obtained by electrodeposition at a constant potential of -0.6 V (vs. SCE) for 40 min in a solution containing 0.5 g L<sup>-1</sup> Pd(NH<sub>3</sub>)<sub>4</sub>Cl<sub>2</sub> and 0.8 g L<sup>-1</sup> Na<sub>2</sub>EDTA (pH 8.5). The current density on the Pd nanoplate's array electrode is ~68 times that on flat Pd electrode. Thus, the Pd nanoplate's array electrode shows extraordinary electro-catalytic activity towards the oxidation of methanol. Choi and Woo [341] prepared a 2D Pt-Ru nanowire network using a SBA-15 nanoreactor and showed that this nanostructured material displayed a higher performance than commercial Pt-Ru (JM) in DMFC. Recently, our group [51] used a facile electrochemical method to fabricate a 2D continuous Pt island network on a flat Si substrate. We found that this catalyst structure on the Si substrate has better electroactivity toward methanol oxidation than the blanket Pt/Si and the Ru decorated Pt film/Si electrodes. Recently many material scientists and engineers have fabricated 2D graphene nanosheets as catalyst supports for DMFCs [342,343]. Bong et al. [343] prepared graphene nanosheets by a modified Hummer's chemical method and utilized as a catalyst support of PtRu nanoparticles for methanol oxidation. The electrochemical results of methanol oxidation indicate that Pt-Ru/graphene nanosheets display excellent catalytic activity over that of Pt-Ru/Vulcan. These results indicate that graphene nanosheets could significantly increase the electrochemical active surface area resulting in better catalyst utilization.

### 5.1.5. 3D NSMs

Compared to 0D, 1D, and 2D NSMs, the 3D NSMs hold a unique morphology, which are expected to provide a larger surface area and to facilitate the transport of reactants and products effectively, so that electrochemical performance can be greatly improved. For this reason, several research groups [91,295,296,344] have fabricated 3D Pt nanoflowers as a catalyst for fuel cell applications. Tong et al. [344] prepared 3D Pt nanosheets perpendicular to a boron-doped diamond (BDD) hybrid film surface, synthesized by double template method, using a hydrogen bubble template and subsequent metallic Zn template to control the morphology of the Pt catalyst on the BDD surface. Fig. 72 illustrates

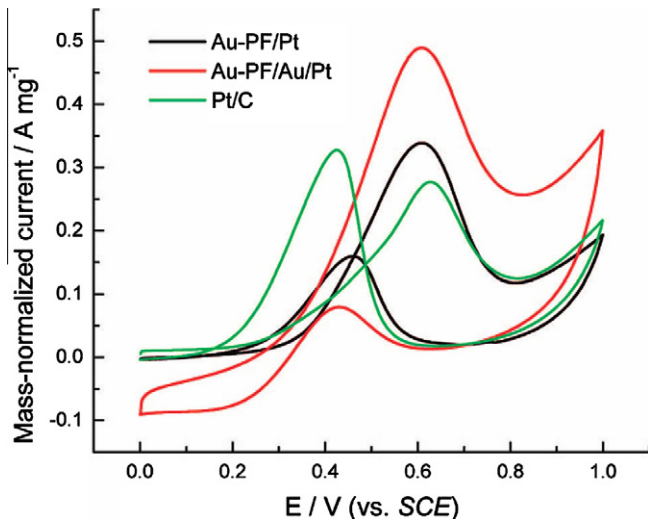


**Fig. 71.** CVs of commercial Pt/C catalyst, Au-PF/Pt and the Au-PF/Au/Pt electrodes in a 0.1 mol dm<sup>-3</sup> HClO<sub>4</sub> + 0.4 mol dm<sup>-3</sup> CH<sub>3</sub>OH solution at a scan rate of 50 mV s<sup>-1</sup>. Reprinted from Ref. [339] with permission of ACS Publishers.

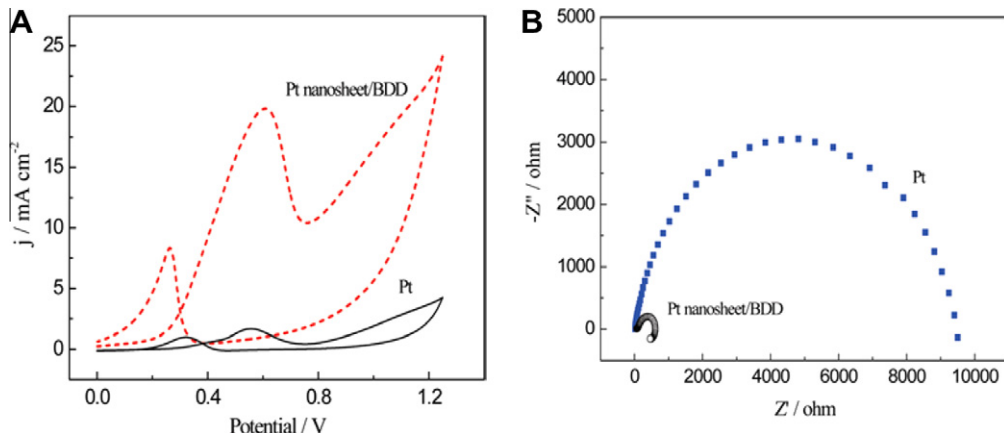


**Fig. 72.** (A) CVs of pristine Pt and the 3D Pt nanosheets/BDD in a 0.1 M  $\text{H}_2\text{SO}_4$ /1.5 M  $\text{CH}_3\text{OH}$  aqueous solution at a scan rate of 50  $\text{mV s}^{-1}$ . (B) Electrochemical impedance spectroscopy of Pt and the 3D Pt nanosheet/BDD into a 0.1 M  $\text{H}_2\text{SO}_4$ /1.5 M  $\text{CH}_3\text{OH}$  solution at potential of 0.375 V. Reprinted from Ref. [344] with permission of ACS Publishers.

the CVs and Nyquist plot of polycrystalline Pt and 3D Pt nanosheets/BDD samples. As shown in Fig. 72, electrochemical results indicated that the 3D Pt nanosheets on BDD hybrid film surface have a high electrocatalytic ability resulting from the large surface area and porous structure, which efficiently facilitates the facile transport of reactants and products, as well as a CO anti-poisoning ability due to the support activity of BDD.

Zhang et al. [91] prepared 3D Pt nanoflowers via a template-free, direct electrodeposition method. This electrochemical experiment demonstrates that Pt nanoflowers have superior performance in aspects of electrocatalytic activity and stability towards the oxidation of methanol. Recently, our group [296] reported on the synthesis of 3D Pt nanoflowers and their electrochemical properties. We found that the 3D Pt nanoflower exhibits very good catalytic activity for methanol oxidation and a high tolerance against CO poisoning. There is a growing interest in “facile” synthetic strategies to obtain 3D porous graphitic carbon nanostructures for use as electrocatalyst supports. This led our group to develop a novel and simple synthetic strategy for fabricating 3D porous graphitic carbon nanostructures [345]. 3D porous graphitic carbons can be used as catalyst supports because of their high surface area, well-defined porous structure, and the presence of various surface functional groups [345,346]. Moreover, the presence of 3D nanopores in graphitic carbon supports may also contribute to obtain higher catalytic activities by virtue of the facile transport of methanol and oxidation products through these nanopores. Since the 3D NSMs provide a large surface area and effectively facilitate the transportation of reactants and products in reaction channels, which is particularly desirable for a catalyst in various electrochemical devices, these simple and new electrodes with their unique surface structure will be very attractive in fuel cells.

## 5.2. Supercapacitors

### 5.2.1. Introduction

Supercapacitors (Fig. 73) represent an important component for energy storage devices, particularly for short-acting high power batteries. Batteries suffer from a relatively slow power delivery or uptake, faster and higher-power energy storage systems are needed in a number of applications, and this role has been given to the supercapacitors [347]. The working principle of supercapacitors has been extensively reported in many review papers and articles [348–351], to which the interested reader is referred for more details. In brief, supercapacitors are formed by two polarizable electrodes, a separator and an electrolyte. They utilize double layer capacitance where the ions of the electrolyte are adsorbed on the charged electrode, resulting in a Helmholtz layer [352,353]. The Helmholtz double

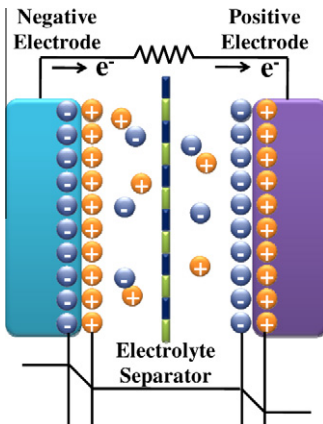


**Fig. 73.** Schematic diagram of the supercapacitor.

layer thickness is defined as half the diameter of the adsorbed solvated ions at the electrode/solution interface [352,353].

Some supercapacitors are commercially available to extend battery life in electronic equipment, but they are still in a development stage. The power density of supercapacitors is lower than that of batteries. Therefore, the development of supercapacitors aims to improve the power density and significantly reduce cost. These electrochemical devices are also known as ultracapacitors, pseudo capacitors, and double layer capacitors. They are DC energy sources and must be interfaced to the electric grid with a static power conditioner. Supercapacitors are attractive for their high power densities and their long cycle life, however they suffer from low energy densities. The highest performance supercapacitors are currently based on NSMs, given that increased electrode surface area improves the capacitance. It is the reason why so many researchers have been involved in working on different kinds of NSMs.

### 5.2.2. 0D and 1D NSMs

Initially researchers synthesized NSMs with zero-dimensional atomic clusters (quantum dots) for supercapacitors. Atomic clusters, nanoparticles, filaments and similar spatially confined molecular systems are defined as zero modulation dimensionality (0D or more correctly quasi-zero dimensional) and possess an aspect ratio from one to infinity. Atomic clusters are spherical and composed of several thousands atoms. However, the possibility of designing atomic clusters is not very promising at present. Two major problems still exist in the synthesis of atomic clusters. First, it is difficult to produce mass-selected clusters in large quantities. Secondly, to make atomic cluster materials, one has to consider other cluster-cluster interactions and make sure that this would not lead to coalescence of clusters that would change its original physical and chemical characteristics. However, well-controlled and mass-producible atomic clusters will likely increase with more advanced research and their applications in the future.

Apart from the above, many research groups [354–358] have found that electrode-active materials with nanoscale crystalline particle size usually show better discharge life due to their high specific surface areas. Additionally, nanoscale particles dramatically change surface reaction rates, causing a dramatic improvement in power density when compared to conventional capacitor. As a result, researchers have tried to develop some transition metal oxides nanoparticles, such as hydrous  $\text{IrO}_2$  [354],  $\text{SnO}_2$  [355], amorphous  $\text{RuO}_2$  [356], hydrous and anhydrous crystalline  $\text{RuO}_2$  nanoparticles [357,358], for supercapacitor applications due to their high pseudocapacitance charge-storage mechanism. The charge-storage mechanism of metal oxides ( $\text{XO}_2$  ( $\text{X} = \text{Ir}, \text{Ru}, \text{Sn}, \text{Mn}$ , etc.)) as proposed is based on the novel concept of redox (oxidation-reduction) reactions associated with the surface reac-

tion and the insertion of metallic cations, for instance,  $H^+$ ,  $Li^+$ ,  $Na^+$ ,  $K^+$  into the metal oxides. The simple reaction on charge-storage mechanism can be written as follows:



Where X and  $C^+$  represent the metal and proton or alkali metal cation, respectively. The interested reader can find details mechanism of charge-storage in the review article [359]. The supercapacitive behavior of various metal oxides, such as  $RuO_2$  [356–358],  $IrO_2$  [354],  $NiO_x$  [360],  $MnO_2$  [361]  $Ni_3(-Fe(CN)_6)_2(H_2O)$  [362] and  $SnO_2$  [363] have already been evaluated. Among these materials,  $RuO_2$  (specific capacitance  $720\text{ F g}^{-1}$ ) [15,356] and  $IrO_2$  (specific capacitance  $550\text{ F g}^{-1}$ ) [364] have been recognized as the most promising candidates for supercapacitor electrodes due to their very large specific capacitance values. The weakness of these nanoparticles are their low specific surface area; therefore one of the key-issues to address increasing their specific surface area. 1D NSMs are able to solve the problem of specific surface area and thus improve the utilization of electrode active materials. Most recently, 1D  $MnO_2$  nanorods [365],  $Co_3O_4$  nanorods [366], polyaniline nanowires [367], single- and multi-walled carbon nanotubes [368],  $Li_4Ti_5O_{12}$  with nanotubes/nanowires [369],  $MnO_2$  nanobelts [370], and  $\gamma$ - $MnO_2$  nanoneedles [371] have been used. Non-hydrous nanoporous  $RuO_2$  with a surface area of  $240\text{ m}^2\text{ g}^{-1}$  synthesized by electrochemical lithiation exhibits a distinctly better storage performance of  $350\text{ F g}^{-1}$  at  $2\text{ mV s}^{-1}$  than that previously reported for nonhydrated  $RuO_2$  [372–374]. These 0D and 1D NSMs still do not resolve the fundamental limitations of the materials for next generation electrochemical supercapacitors. In addition, high material cost limits the commercial use, so it is urgent to look for a substitute materials to replace  $RuO_2$ . Therefore, there is still need for plenty of research to improve the performance of the supercapacitors.

### 5.2.3. 2D NSMs

2D NSMs dramatically change surface reaction rates and electrical transport throughout the material, causing a dramatic improvement in specific power density when compared to conventional capacitor. Recent reports by various groups have shown that 2D NSMs (such as nanosheets, nanobelts, nanowalls, nanofibers, and nanoplates) enhance the average specific capacitance [375–382,34,383]. Wang et al. [381] direct synthesized single-crystalline  $Ni(OH)_2$  hexagonal nanoplates on lightly oxidized graphene nanosheets (Fig. 74A). The electrically conducting graphene nanosheets exhibit a high specific capacitance of  $\sim 1335\text{ F g}^{-1}$  at a charge and discharge current density of  $2.8\text{ A g}^{-1}$  and  $\sim 953\text{ F g}^{-1}$  at  $45.7\text{ A g}^{-1}$  with remarkable cycling ability (Fig. 74B).

In the same year, Song et al. [382] prepared porous assembled 2D nanosheets of alkali metal manganese oxides via exfoliation-reassembling route and used them as electrodes for supercapacitors. The porous assembled 2D nanosheets manganese oxides have a high specific capacitance value of  $\sim 140$ – $160\text{ F g}^{-1}$  and remarkable cyclability of  $\sim 93$ – $99\%$  up to the 1000th cycle. It is well known that the polyaniline (PANI) is a highly conducting polymer. In addition, it has attracted much attention during the

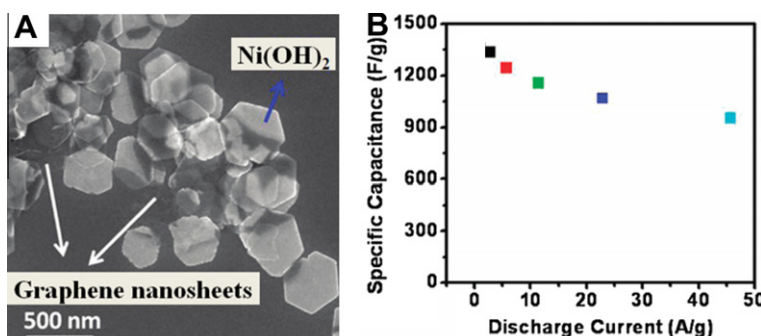


**Fig. 74.** (A) SEM image of  $Ni(OH)_2$  nanoplates/GNS and (B) average specific capacitance of  $Ni(OH)_2$  nanoplates/GNS at different discharge current densities. Reprinted from Ref. [381] with permission of ACS Publishers.

past year because it is low cost, superior electrochemical performance, distinguishable electrical properties, mechanical flexibility, and relative ease of processing. Li et al. [34] fabricated PANI nanobelts onto a conducting substrate via an electrochemical route. These PANI nanobelts on conducting substrate showed large capacitances of  $873 \text{ F g}^{-1}$  at  $10 \text{ mV s}^{-1}$  and excellent stability over 1000 cycles. Recently, Wu et al. [383] prepared composite films of chemically converted graphene (CCG) and PANI nanofibers (PANI-NFs) and applied them as electrodes for supercapacitors. They found that the conductivity of the composite film is about 10 times that of a PANI-NF film. This conductive composite film showed a large electrochemical capacitance ( $210 \text{ F g}^{-1}$ ) at a discharge rate of  $0.3 \text{ A g}^{-1}$ . Moreover, the electrochemical capacitances are much higher than those of supercapacitors based on pure CCG or PANI-NF films, mainly due to the synergic effect of both components. This means 2D NSMs exhibit high specific capacitance and remarkable rate capability as well as promise for applications in supercapacitors with both high energy and power densities. The weakness of these 2D NSMs are their low specific surface area, therefore, present research and development for these materials are focusing on increasing their specific surface area.

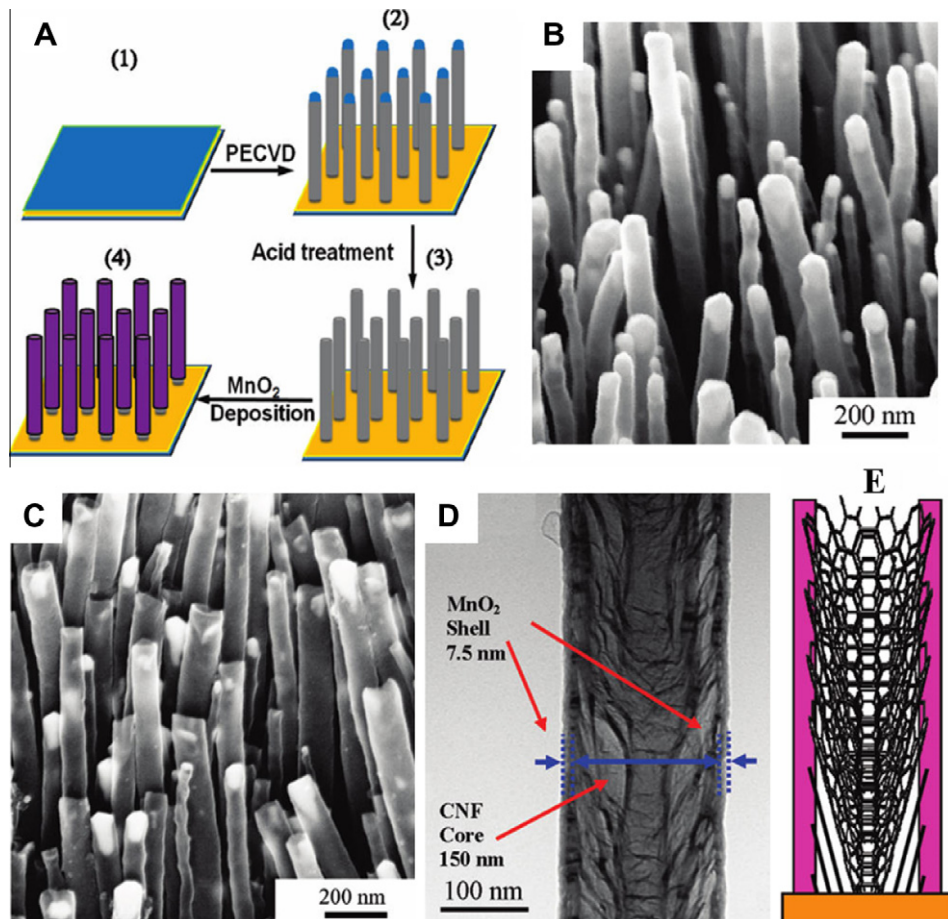


**Fig. 75.** (A) Procedure for the fabrication of manganese oxide layer/vertically aligned CNTs electrode. (B) SEM picture of a vertically aligned CNTs. (C) SEM image of a vertically aligned CNTs after 10–15 min of treatment in 1.0 M HNO<sub>3</sub> followed by manganese oxide deposition. (D) TEM image of the same sample shown in Fig. 1. (C and E) Schematic drawing of MnO<sub>2</sub> deposition onto the sidewall of the cup-stacking graphitic structure of CNTs. Reprinted from Ref. [63] with permission of ACS Publishers.

### 5.2.4. 3D NSMs

3D NSMs may not only improve surface reaction rates, chemical stability, and electrical transport, but also greatly enhance the specific surface area throughout the material, causing a dramatic improvement in storage capacity when compared with the 2D based supercapacitors [63,15,384]. Recently, Liu et al. [63] prepared hybrid supercapacitor electrodes by coaxially coating manganese oxide on a vertically aligned carbon nanofiber array (Fig. 75). These ordered core–shell nanostructures have a very large surface area, which is 10 times higher than that of the flat surface. This large surface area offers a highly conductive and robust core for reliable electrical connection to the  $\text{MnO}_2$  shell, which ensures the rapid completion of the redox reactions and offer easy electrolyte access to a large-volume of active electrode materials. The specific capacitance value of core–shell nanostructure in a 0.10 M  $\text{Na}_2\text{SO}_4$  aqueous electrolyte is  $\sim 365 \text{ F g}^{-1}$ . In 2006, Hu et al. [15] synthesized an ordered 3D hydrous  $\text{RuO}_2$  nanotubular arrayed electrodes via modified AAO template method. The ordered 3D hydrous  $\text{RuO}_2$  nanotubes have both a very high specific power and specific energy at 0.8 V and 4 kHz equal to  $4320 \text{ kW kg}^{-1}$  and  $7.5 \text{ W h kg}^{-1}$ , respectively. Based on their results, we can conclude that the ordered 3D hydrous  $\text{RuO}_2$  nanotubes structure not only reduces the diffusion resistance of electrolytes but also enhances the facility of ion transportation and maintains smooth electron pathways in very rapid charge/discharge reactions [15]. Kim et al. [384] synthesized 3D vertically aligned CNTs onto conductive carbon papers and applied them as electrodes for supercapacitors. Remarkable supercapacitor properties were obtained by using the directly integrated, naturally patterned, and vertically aligned CNTs. The specific capacitance, energy, and power density were  $\sim 200 \text{ F g}^{-1}$ ,  $\sim 20 \text{ W h kg}^{-1}$ , and  $\sim 40 \text{ kW kg}^{-1}$  respectively, (in 1 M  $\text{H}_2\text{SO}_4$  solution, current density =  $20 \text{ A g}^{-1}$ ). Hence, the 3D nanostructured electrode materials that boost high surface area exhibit good chemical stability, and have an ordered macro-porous structure increases the electrode/electrolyte interfacial area and facilitate ion transfer in the system with improved storage capacity. Moreover, we believe that 3D NSMs are able to resolve fundamental limitations of materials for next-generation scaling of advanced supercapacitors devices.

## 5.3. Li-ion batteries

### 5.3.1. Introduction

Li-ion batteries (Fig. 76) represent a further important component for energy storage. The working principle of Li-ion batteries and its practical applications have been extensively reported in many review papers and articles [385–389] to which the interested reader is referred for more details. In brief, Li-ion batteries consist of a three primary functional components. The main components of a Li-ion battery device are the positive electrode, negative electrode and the electrolyte, for which a variety of materials may be used. Generally, the most useful material for the positive electrode is one of three materials: lithium cobalt oxide, lithium iron phosphate, or a spinel such as lithium  $\text{MnO}_2$ . On the other hand, the most common materials for the negative electrode are carbon based compounds and lithium-containing alloys.

Upon charging, lithium ions are extracted from the positive electrode material and inserted into the negative electrode material. Upon discharging, the reverse process takes place. Common batteries should exhibit three characteristics: (a) high energy and power capacity, (b) high charging rate, and (c) long lifetime (cycling stability). Although Li-ion batteries are available commercially, the performance of Li-ion batteries is limited by the current electrode and electrolyte materials. For future generations of rechargeable Li-ion batteries, not only for applications in portable electronic devices but especially for clean energy storage and use in hybrid electric vehicles, further improvements of materials are essential. We need to find new, efficient and effective ways to improve the physical and chemical characteristics of the materials for use in electrochemical Li-ion batteries. One avenue that is opening up is that of NSMs for electrochemical Li-ion batteries devices. However, the selection of NSMs for use as negative electrode, positive electrode, and electrolyte, as well as their voltage, capacity, life, and safety abilities in electrochemical Li-ion battery devices can dramatically improve. Recently, great efforts have been made toward the development of improved electrolyte, negative and positive electrodes materials, therefore the focus of this review paper is on the 0D, 1D, 2D, and 3D

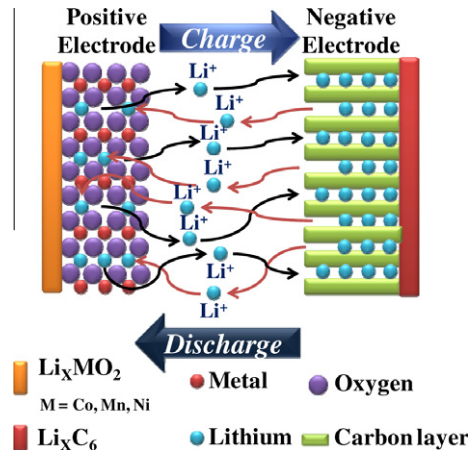


**Fig. 76.** Schematic diagram of the Li-ion battery.

NSMs for electrochemical Li-ion battery devices. These novel nanostructured electrodes have been employed to improve the reversibility of rechargeable Li-ion battery devices.

### 5.3.2. 0D and 1D NSMs

It has been demonstrated that the morphology of nanostructures can be optimized to achieve higher energy and charge densities in electrochemical Li-ion battery devices. Therefore, nanoarchitecture is another consideration that can be optimized for further improvement. In this regard, research on NSMs is expanding rapidly into the assembly of nanoparticles in 0D and 1D structures.

Recently, some research groups [390–392] have tried to synthesize 0D nanoparticles to avoid the problem of poor  $\text{Li}^+$  ion diffusivity and electron conductivity, which would eliminate either metal doping or carbon coating. This is due to the 0D nanoparticles allowing the diffusion length of  $\text{Li}^+$  ions to have a shorter path through the lattice from the core of the particles to the surface, thereby leading to excellent electrochemical performance with better capacity retention [393]. 0D nanoparticles with high-crystallinity are particularly advantageous when the aim as above mentioned is to achieve faster lithium-ion diffusion. They also display a better rate capability, which indicates its possible use in electrochemical Li-ion battery devices. However, 0D NSMs are not very stable and very difficult to make in large quantities. Various efforts have been implemented to synthesize novel 0D NSMs but have been met with very limited success in the improvement of electrochemical Li-ion battery device performance. Due to this, researchers have fabricated new 1D NSMs that will make electrochemical Li-ion battery devices more efficient due to their unique mechanical, thermal, electrical properties and structural versatility. Various efforts have been made by the scientific community to fabricate novel 1D NSMs such as nanotubes, nanorods, and nanobelts [394–396]. Fig. 77 shows the schematic diagram of a  $\text{Li}^+$  ion pathway in 1D NSMs.

Cui et al. [394] fabricated core–shell Si nanowires on stainless steel current collectors utilizing  $\text{SiH}_4$  in a CVD furnace. They reported that the core–shell Si nanowires have a high charge storage capacity ( $\sim 1000 \text{ mA h g}^{-1}$ , three times of carbon) with  $\sim 90\%$  capacity retention over 100 cycles. They also noticed good electrochemical performance at high rate charging and discharging ( $6.8 \text{ A g}^{-1}$ ,  $\sim 20$  times of carbon at 1 h rate). Core–shell Si nanowires can relax the strain and overcome the problem of pulverization, maintain direct electrical connection with the current collector, and have short diffusion distance for lithium insertion. In a later report, Cui et al. [395] used a CVD (amorphous Si (a-Si)) method to fabricate the carbon–silicon core–shell nanowires by CVD onto carbon nanofibers. Carbon–silicon core–shell nanowires have a high charge storage capacity of  $\sim 2000 \text{ mA h g}^{-1}$  and good cycling life. In addition, these nanowires have a high Coulombic efficiency of 90% for the first cycle and 98–99.6% for the following cycles. They also constructed a full cell composed of a  $\text{LiCoO}_2$  cathode and a car-

bon–silicon core–shell nanowire anode. Significantly, using these core–shell nanowires they achieved high mass loading and an area capacity of  $\sim 4 \text{ mA h cm}^{-2}$ . In the same year, Park et al. [396] reported that these Si nanotubes have an excellent reversible charge capacity of  $3247 \text{ mA h g}^{-1}$  with Coulombic efficiency of 89%, they also demonstrated the superior capacity retention even at a rate of 5C ( $= 15 \text{ A g}^{-1}$ ). Importantly, the capacity of a Li-ion full cell consisting of a cathode of  $\text{LiCoO}_2$  and anode of Si nanotubes shows a higher capacity than commercially available graphite even after 200 cycles. However, a new problem arose for 1D NSMs are low surface area and slow diffusion rates. Due to low surface area, slow diffusion rates and poor conductivity, 1D NSMs show the poor energy density and poor rate capacities. Consequently, improvement in surface area to volume ratio, diffusion rates and conductivity is necessary. We should be able to enhance the above properties via synthesis of 2D NSMs.

### 5.3.3. 2D NSMs

2D NSMs are a useful approach to improve the electrode performances in higher overall capacity, high-rate capability, and longer cycling life. 2D NSMs normally exhibit small crystalline size, high surface area, large surface-to-volume ratio, and favorable structural stability over 1D, and 0D NSMs. The development of a 2D nanostructure gives the right structure necessary for a fast mass transport, for instance. On this nanostructure, a secondary guest nanoscale structure is built in order to take advantage of the properties of nanometer-sized building blocks. Fig. 78 shows the schematic diagram of a  $\text{Li}^+$  ion pathway in 2D NSMs. Thus, 2D NSMs such as nanodisks, nanonets, nanoplatelets, nanobelts, and nanosheets have been synthesized by many research groups to further enhance the electrochemical Li-ion battery devices performance [398–406].

Recently, Zhou et al. [404] synthesized a  $\text{Si/TiSi}_2$  heteronanostructure on Ti foil in a CVD chamber with  $\text{TiCl}_4$ ,  $\text{SiH}_4$  and  $\text{H}_2$  as precursors. The  $\text{Si/TiSi}_2$  heteronanostructure was used as an anode material for  $\text{Li}^+$  batteries. Fig. 79A–D shows the morphology of typical as-made  $\text{Si/TiSi}_2$  nanostructures. In this heteronanostructure, Si nanoparticles acts as an active component to store and release  $\text{Li}^+$  while  $\text{TiSi}_2$  serves as the inactive component to support Si and to facilitate charge transport. The  $\text{Si/TiSi}_2$  heteronanostructures show fast and superior charge/discharge capacities. Fig. 79E shows the charge capacity and Coulombic efficiency for the  $\text{Si/TiSi}_2$  heteronanostructure. A fast charge–discharge rate of  $8400 \text{ mA g}^{-1}$ , high capacity retention of >99% per cycle at the level of  $1000 \text{ mA h g}^{-1}$  were achieved after 100 smoothing cycles.

Recently, Hassoun et al. [405] used a high capacity Sn–C nanostructure as an anode and high rate, high voltage  $\text{Li}[\text{Ni}_{0.45}\text{Co}_{0.1}\text{Mn}_{1.45}]\text{O}_4$  spinel as a cathode to fabricate a Li-ion battery. This Li-ion battery offers superior performances in terms of cycling life, i.e.,  $\sim 100$  high rate cycles, for rate capability, operating at 5C and still keeping more than 85% of the initial capacity, and an energy density, expected to be of the order of  $170 \text{ W h kg}^{-1}$ . Although the 1D NSMs show high discharge capacity and good cycling performance at low rate, the initial Coulombic efficiency and cycling stability at high rate are still disappointing. In addition, 2D NSMs are limited in the amount of energy that they can store. In 3D NSMs, we use the third dimension to increase the electrochemically active area in the Li-ion battery. This means we should be able to greatly improve the efficiency (higher capacity, high-rate capability, and cycling life) of advanced Li-ion battery devices.

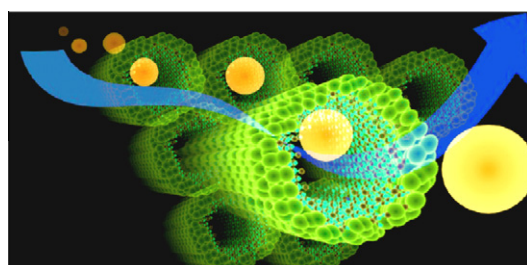


**Fig. 77.** Schematic illustration of Li-ion pathway in 1D nanotubes. Reprinted from Ref. [396] with permission of ACS Publishers.

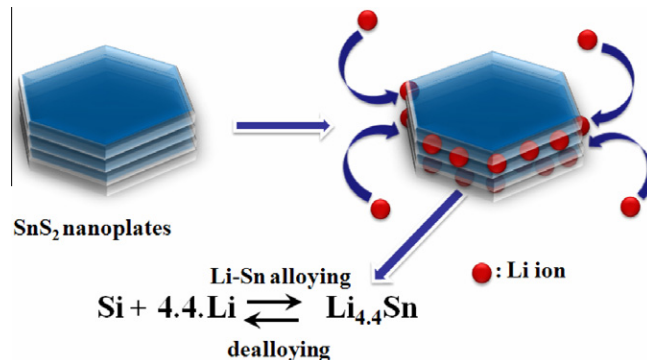


**Fig. 78.** Schematic illustration of Li-ion pathway in 2D  $\text{SnS}_2$  nanoplates (modified after Ref. [397]).

#### 5.3.4. 3D NSMs

In order to further achieve higher energy and charge densities in electrochemical Li-ion battery devices, 3D nanostructured electrodes may be needed. As 3D NSMs electrode have a higher surface area, large surface-to-volume ratio, and more favorable structural stability over 2D, 1D, and 0D NSMs. The 3D NSMs can be flooded with electrolyte, ensuring a high specific surface area in contact with the electrode and hence a high flux of  $\text{Li}^+$  ion across the interface. Fig. 80 shows the schematic diagram of a Li-ion pathway in 3D NSMs. The nanowalls between the NSMs, of equal dimensions throughout, ensure very short diffusion paths for Li ions on intercalation and deintercalation, and hence homogeneous rates of transports.

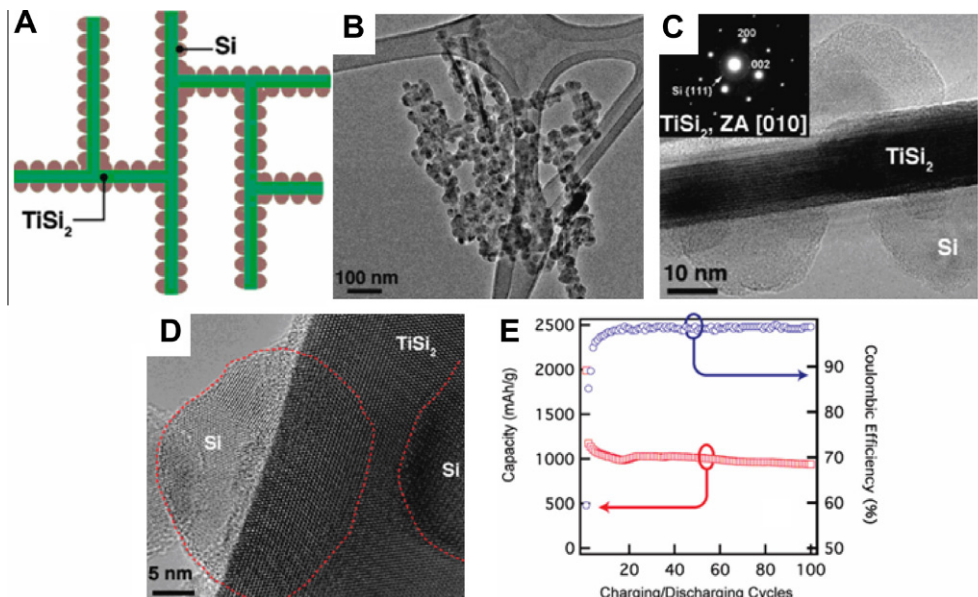


**Fig. 79.** (A) A schematic drawing of the  $\text{Si}/\text{TiSi}_2$  structure. (B) TEM image of the  $\text{Si}$  coating on  $\text{TiSi}_2$  nanonets. (C) HRTEM image and the SAED pattern reveal the crystallinity of the  $\text{TiSi}_2$  core and the particulate  $\text{Si}$  coating. (D) The crystallinity of  $\text{TiSi}_2$  and  $\text{Si}$  (marked by the dotted red line) is shown in this lattice-resolved TEM picture. (E) Charge capacity and Coulombic efficiency performed between 0.150 and 3.00 V. Reprinted from Ref. [404] with permission of ACS Publishers.

We believe that the concept of hierarchically NSMs, template technique in preparing and assembling materials will be a useful approach to reach the above objectives [406–410]. Reddy et al. [410] used vacuum filtration and CVD techniques to prepare coaxial  $\text{MnO}_2$ /carbon nanotube arrays using AAO templates. The coaxial  $\text{MnO}_2$ /carbon nanotube arrays were used as cathodes in a LIB. Fig. 81A shows SEM image and schematic drawing of single  $\text{MnO}_2$ /CNT hybrid nanostructures. Fig. 81B represents the charge–discharge voltage curves for these  $\text{MnO}_2$ /CNT nanotube arrays. The first discharge capacity and reversible capacity (after 15 cycles) of the  $\text{MnO}_2$ /CNT hybrid coaxial nanotubes are  $\sim 2170$  and  $\sim 500 \text{ mA h g}^{-1}$ , respectively. An excellent reversible capacity was obtained for these  $\text{MnO}_2$ /CNT nanotube array electrodes. The coaxial  $\text{MnO}_2$ /carbon nanotube arrays offer the following advantages: (a) presence of carbon nanotube improves the electrical conductivity, (b) homogeneous electrochemical accessibility and better ionic conductivity is achieved by avoiding agglomerative binders and other additives, (c) well-directed coaxial alignment provides a better conductive path, and (d)  $\text{MnO}_2$ /CNT hybrid nanostructures offer a unique dual-binding mechanism of lithium storage (insertion–deinsertion in the case of carbon nanotubes and formation and decomposition of  $\text{Li}_2\text{O}$  in the case of  $\text{MnO}_2$  nanotubes).

Moreover, 3D NSMs such as nanoflowers also exhibit higher initial Coulombic efficiency, higher reversible capacity, and better cycling performance [411–413]. Kim et al. [413] fabricated a hierarchical nanostructure composed of  $\text{FeF}_3$  nanoparticles and carbon nanotubes (CNTs). The hierarchical nanostructure synthesized by functionalizing CNT has a unique surface structure with nanosized features, which has the appearance of  $\text{FeF}_3$  nanoflowers on CNT branches (FNCB). The specific capacity of

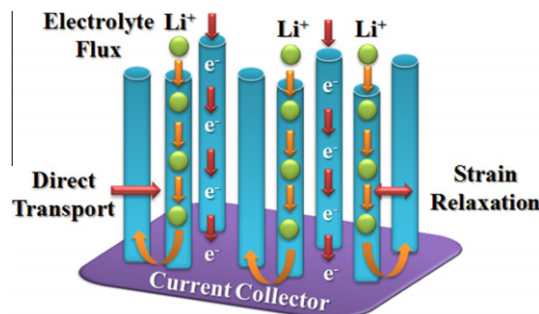


**Fig. 80.** Schematic illustration of Li-ion pathway in ordered 3D nanostructures.

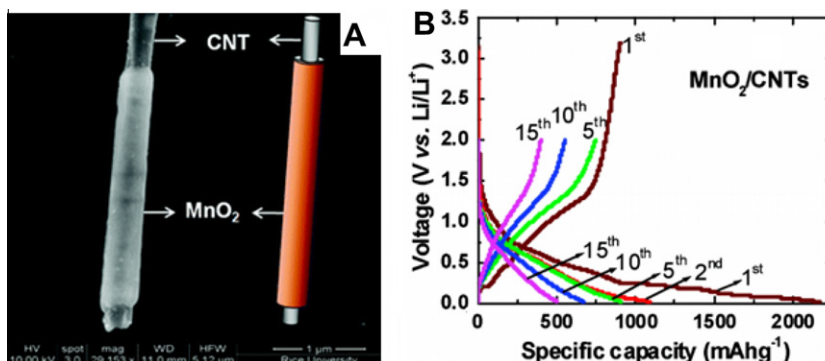


**Fig. 81.** (A) SEM image and a schematic drawing of an individual coaxial  $\text{MnO}_2$ /CNT nanotube. (B) Voltage versus specific capacity curves were obtained from the  $\text{MnO}_2$ /CNT nanotube array electrodes at a scan rate of  $50 \text{ mA g}^{-1}$  between 3.2 and  $0.02 \text{ V}$  vs.  $\text{Li}/\text{Li}^+$ . Reprinted from Ref. [410] with permission of ACS Publishers.

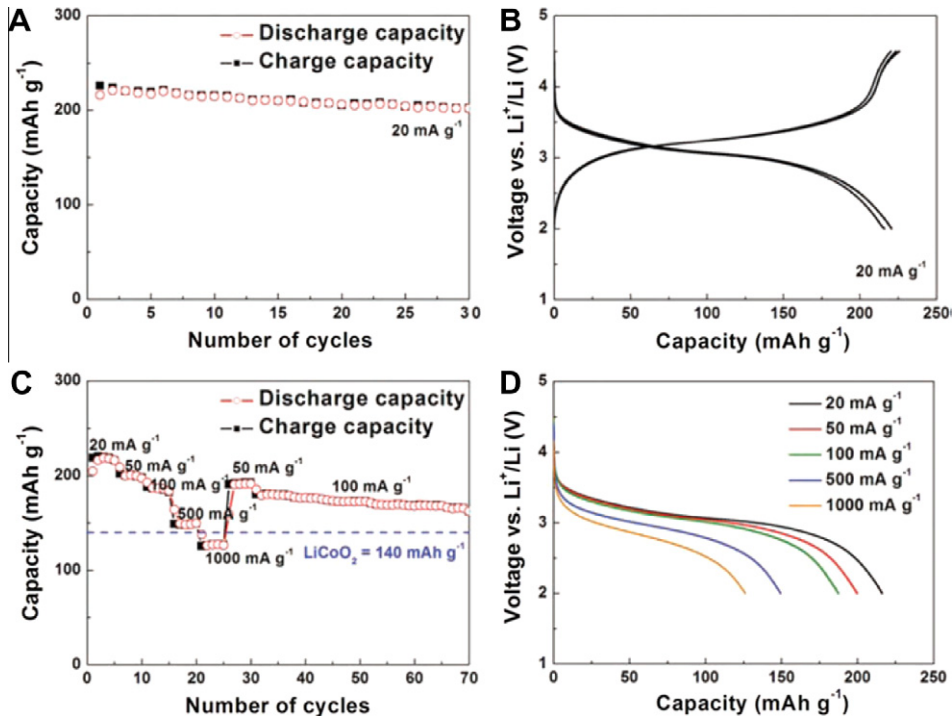


**Fig. 82.** (A) Specific capacity of FNCB as a function of cycle numbers (voltage range, 2.0–4.5 V; current rate, 20 mA g<sup>-1</sup>) over one precycle at a voltage range of 1.5–4.5 V, and (B) initial charge/discharge curves of a three cycles. (C) Specific capacity of FNCB with various current densities from 20 to 1000 mA g<sup>-1</sup> (voltage range, 2.0–4.5 V) over the precycle, and (D) corresponding discharge curves at each current density. The horizontal blue dashed line in (C) represents the practical capacity of the LiCoO<sub>2</sub> cathode. Reprinted from Ref. [413] with permission of Wiley-VCH Verlag GmbH & Co. KGaA.

FNCB was  $\sim 210$  mA h g<sup>-1</sup> at a current rate of 20 mA g<sup>-1</sup>. In addition, FNCB gives excellent cycling performance in the voltage range of 2.0–4.5 V at the current rate of 20 and 1000 mA g<sup>-1</sup> over 30 cycles (Fig. 82A–C). FNCB delivers more than 180 mA h g<sup>-1</sup> at a constant current density of 100 mA g<sup>-1</sup>. Even at a current density of 500 mA g<sup>-1</sup>, the specific capacity of FNCB was  $\sim 150$  mA h g<sup>-1</sup>. The FNCB delivers a higher capacity than that of LiCoO<sub>2</sub> at the same current density. Fig. 82D shows the corresponding discharge curves for FNCB at different current densities. The FNCB electrode indicated only a small polarization with a discharge potential  $\sim 2.8$  V even at current densities as high as 1000 mA g<sup>-1</sup>.

The use of 3D NSMs is increasing rapidly in the field of Li-ion battery devices because of their substantial advantages in terms of mass transport. Transport in 3D NSMs typically encompasses shorter transport length for Li<sup>+</sup> ions and electrons, better electrode–electrolyte contact area, and great merits to permit reproducible Li<sup>+</sup> insertion and extraction. This verifies their promising application as electrode materials for Li-ion batteries.

## 6. Conclusions and future outlook

This article reviewed the recent advancement in synthesis and fabrication of nanostructures materials (NSMs). Knowing that nanostructure material exhibits chemical and physical property that are significantly different from those of bulk and microsize materials. A detailed account on the parameter that can be optimized to enhance the novel properties of these NSMs have been covered in this review. In addition, potential application of NSMs in technological applications for instance electrochemical energy devices (EEDs) has been discussed. The article has been systematically structured to give clear

and detailed insight. In the first section we reviewed recent paper and classified the NSMs into four categories according to their dimensions: zero-dimensional (0D), one-dimensional (1D), two-dimensional (2D) and three-dimensional (3D) nanostructures. In the second section of the article, we discussed recent approaches for the synthesis and fabrication of 0D, 1D, 2D and 3D NSMs. In addition, we have also described the most common (physical and chemical) routes for fabricating or synthesizing 0D, 1D, 2D and 3D NSMs. Finally, electrochemical efficiency of EEDs associated with the use of 0D, 1D, 2D and 3D NSMs has been discussed. However, challenges remain using such NSMs to achieve highly efficient catalysis for EEDs. In particular, the synthesis methods, shapes, and selective catalysts of the NSMs need to be optimized to overcome the specific factors that limit the EEDs performance. Consequently, there remains a greater need for intelligent surface structure designs to achieve durable and highly efficient EEDs. Therefore, intensive research efforts are ongoing to develop active NSMs for EEDs.

With great progress being made in the synthesis of NSMs, there are fascinating new opportunities for materials scientists. While considerable attention is devoted to nanostructure aspects (for instance 0D, 1D, 2D, and 3D nanomaterials) future progress will hinge on a better understanding of how synthesis techniques, composition, size, and morphology affect the catalytic activity of 0D-, 1D-, 2D- and 3D-based nanomaterials. The development of simple, new and efficient synthesis and fabrication processes that allow precise control over size and morphology of resulting products and improve the performance of 0D, 1D, 2D and 3D NSMs in applications such as fuel cells, lithium ion batteries, and supercapacitios. In addition, as greater knowledge is acquired about the physical and chemical properties of 0D-, 1D-, 2D- and 3D-based nanomaterials, there will be more opportunities to exploit individual characteristics in magnetic, electric and optical based applications. Moreover, the development of 0D-, 1D-, 2D- and 3D-based nanomaterials will help to improve our old technologies, and further research will produce more impressive results that will benefit industries and society.

## Acknowledgments

The authors gratefully acknowledge corresponding publishers for the kind permissions to reproduce their materials, especially figures, used in this review article. This work was supported by NRF (National Honor Scientist Program: 2010-0020414, WCU: R32-2008-000-10180-0).

## References

- [1] Ren X, Zelenay P, Thomas S, Davey J, Gottesfeld S. *J Power Sources* 2000;86:111.
- [2] de Oliveira EC, Pires CTGVM, Pastore HO. *J Braz Chem Soc* 2006;17:16.
- [3] Hu LB, Choi JW, Yang Y, Jeong S, La Mantia F, Cui LF, et al. *Proc Natl Acad Sci USA* 2009;106:21490.
- [4] Kamarudin SK, Achmad F, Daud WRW. *Int J Hydrogen Energy* 2009;34:6902.
- [5] Chen H, Cong TN, Yang W, Tan C, Li Y, Ding Y. *Prog Nat Sci* 2009;19:291.
- [6] Arico AS, Bruce P, Scrosati B, Tarascon JM, Van Schalkwijk W. *Nature Mater* 2005;4:366.
- [7] Ferreira-Aparicio P, Folgado MA, Daza L. *J Power Sources* 2009;192:57.
- [8] Li HQ, Wang YG, Wang CX, Xia YY. *J Power Sources* 2008;185:1557.
- [9] Jin YH, Lee SH, Shim HW, Ko KH, Kim WD. *Electrochim Acta* 2010;55:7315.
- [10] Dong Z, Kennedy SJ, Wu Y. *J Power Sources* 2011;196:4886.
- [11] Mastragostino M, Soavi F. *J Power Sources* 2007;174:89.
- [12] Winter M, Brodd RJ. *Chem Rev* 2004;104:4245.
- [13] Armand M, Tarascon JM. *Nature* 2008;451:652.
- [14] Simon P, Gogotsi Y. *Nature Mater* 2008;7:845.
- [15] Hu CC, Chang KH, Lin MC, Wu YT. *Nano Lett* 2006;6:2690.
- [16] Gleiter H. *Acta Mater* 2000;48:1.
- [17] Skorokhod V, Ragulya A, Uvarova I. Physico-chemical kinetics in nanostructured systems. Kyiv: Academperiodica; 2001. p. 180.
- [18] Pokropivny VV, Skorokhod VV. *Mater Sci Eng C* 2007;27:990.
- [19] Fang M, Zeisberg WM, Condon C, Ogryzko V, Danchin A, Mechold U. *Nucl Acids Res* 2009;37:5114.
- [20] Kim YT, Han JH, Hong BH, Kwon YU. *Adv Mater* 2010;22:515.
- [21] Zhang G, Wang D. *J Am Chem Soc* 2008;130:5616.
- [22] Wang J, Lin M, Yan Y, Wang Z, Ho PC, Loh KP. *J Am Chem Soc* 2009;131:11300.
- [23] Gautam UK, Vivekchand SRC, Govindaraj A, Kulkarni GU, Selvi NR, Rao CNR. *J Am Chem Soc* 2005;127:3658.
- [24] Lee JY, Hong BH, Kim WY, Min SK, Kim Y, Jouravlev MV, et al. *Nature* 2009;460:498.
- [25] Stouwdam JW, Janssen RAJ. *J Mater Chem* 2008;18:1889.
- [26] Lee W, Kang SH, Kim JY, Kolekar GB, Sung YE, Han SH. *Nanotechnology* 2009;20:335706.

- [27] Mokerov VG, Fedorov YV, Velikovski LE, Scherbakova MY. Nanotechnology 2001;12:552.
- [28] Ustinov VM et al. Nanotechnology 2000;11:397.
- [29] Iijima S. Nature 1991;354:56.
- [30] Kuchibhatla SVNT, Karakoti AS, Bera D, Seal S. Prog Mater Sci 2007;52:699.
- [31] Huang L, Wang H, Wang Z, Mitra A, Zhao D, Yan Y. Chem Mater 2002;14:876.
- [32] Okada T, Kawashima K, Nakata Y, Ning X. Jpn J Appl Phys 2005;44:688.
- [33] Xia H, Feng J, Wang H, Lai MO, Lu L. J Power Sources 2010;195:4410.
- [34] Li GR, Feng ZP, Zhong JH, Wang ZL, Tong YX. Macromolecules 2010;43:2178.
- [35] Park JM, Nalwa KS, Leung W, Constant K, Chaudhary S, Ho KM. Nanotechnology 2010;21:215301.
- [36] Cao LM, Tian H, Zhang Z, Zhang XY, Gao CX, Wang WK. Nanotechnology 2004;15:139.
- [37] Yoon SM, Hwang IC, Kim KS, Choi HC. Angew Chem Int Ed 2009;48:2506.
- [38] Wang Y, Lee JY, Kim JS, Kim GH, Kim KS. Chem Mater 2007;19:3912.
- [39] Wang YW, Hong BH, Lee JY, Kim JS, Kim GH, Kim KS. J Phys Chem B 2004;108:16723.
- [40] Hong BH, Bae SC, Lee CW, Jeong S, Kim KS. Science 2001;294:348.
- [41] Hong BH, Lee JY, Lee CW, Kim JC, Bae SC, Kim KS. J Am Chem Soc 2001;123:10748.
- [42] Hong BH et al. Proc Natl Acad Sci USA 2005;102:14155.
- [43] Hong BH, Lee JY, Beetz T, Zhu Y, Kim P, Kim KS. J Am Chem Soc 2005;127:15336.
- [44] Hwang IC et al. J Phys Chem B 2010;114:7216.
- [45] Kim KS et al. J Am Chem Soc 2002;124:14268.
- [46] Kim WY, Choi YC, Kim KS. J Mater Chem 2008;18:4510.
- [47] Jun JW, Seo JW, Oh SJ, Cheon J. Coord Chem Rev 2005;249:1766.
- [48] Kim KS et al. Nature 2009;457:706.
- [49] Bae S et al. Nature Nanotechnol 2010;5:574.
- [50] Pradhan D, Leung KT. J Phys Chem C 2008;112:1357.
- [51] Tiwari JN, Pan FM, Tiwari RN, Nandi SK. Chem Commun 2008;6516.
- [52] Nayak BB, Behera D, Mishra BK. J Am Ceram Soc 2010;93:3080.
- [53] Dong X, Ji X, Jing J, Li M, Li J, Yang W. J Phys Chem C 2010;114:2070.
- [54] Mann AKP, Skrabalak SE. Chem Mater 2011;23:1017.
- [55] Siril PF, Ramos L, Beaunier P, Archirel P, Etcheberry A, Remita H. Chem Mater 2009;21:5170.
- [56] Vizireanu S, Stoica SD, Luculescu C, Nistor LC, Mitu B, Dinescu G. Plasma Sources Sci Technol 2010;19:034016.
- [57] Jung SH, Oh E, Lee KH, Yang Y, Park CG, Park W, et al. Cryst Growth Des 2008;8:265.
- [58] Shen Q, Jiang L, Zhang H, Min Q, Hou W, Zhu JJ. J Phys Chem C 2008;112:16385.
- [59] Teng XW, Liang XY, Maksimuk S, Yang H. Small 2006;2:249.
- [60] Lee H, Habas SE, Kweskin S, Butcher D, Somorjai GA, Yang PD. Angew Chem Int Ed 2006;45:7824.
- [61] Wang L, Yamauchi Y. Chem Mater 2009;21:3562.
- [62] Wang JN, Su LF, Wu ZP. Cryst Growth Des 2008;8:1741.
- [63] Liu J, Essner J, Li J. Chem Mater 2010;22:5022.
- [64] Lei W, Liu D, Zhang J, Zhu P, Cui Q, Zou G. Cryst Growth Des 2009;9:1489.
- [65] Hwang IC et al. Nanotechnology 2009;20:245605.
- [66] Nalwa HS. Nanostructured materials and nanotechnology, vol. 1, no. 1. USA: Academic Press; 2000. p. 2.
- [67] Siegel RW, Ramasamy S, Hahn H, Zongquan L, Ting L, Gronskey R. J Mater Res 1988;3:1367.
- [68] Stewart ME, Mack NH, Malyarchuk V, Soares JANT, Lee TW, Gray SK, et al. Proc Natl Acad Sci USA 2006;103:17143.
- [69] Stewart ME, Yao J, Maria J, Gray SK, Rogers JA, Nuzzo RG. Anal Chem 2009;81:5980.
- [70] Haes AJ, Van Duyne RP. J Am Chem Soc 2002;124:10596.
- [71] Haes A, Chang L, Klein W, Van Duyne R. J Am Chem Soc 2005;127:2264.
- [72] Zheng Y, Juluri B, Mao X, Walker T, Huang T. J Appl Phys 2008;103:014308.
- [73] Lucas B, Kim J, Chin C, Guo L. Adv Mater 2008;20:1129.
- [74] Marinakos S, Chen S, Chilkoti A. Anal Chem 2007;79:5278.
- [75] Lee S, Mayer KM, Hafner JH. Anal Chem 2009;81:4450.
- [76] Schwartzman M, Mathur A, Hone J, Jahnnes C, Wind SJ. Appl Phys Lett 2008;93:153105.
- [77] Zheng J, Song X, Li X, Pu Y. J Phys Chem C 2008;112:27.
- [78] Montavon G, Sampath S, Berndt CC, Herman H, Coddet C. Surf Coat Technol 1997;91:107.
- [79] Senthilnathan V, Ganesan S. J Renew Sustain Energy 2010;2:063102.
- [80] Perednis D, Wilhelm O, Pratsinis SE, Gauckler LJ. Thin Solid Films 2005;474:84.
- [81] Gleiter H. Prog Mater Sci 1989;33:223.
- [82] Siegel RW. Ann Rev Mater Sci 1991;21:559.
- [83] Anderton DJ, Sale FR. Powder Metall 1979;1:8.
- [84] Dahl JA, Maddux BL, Hutchison JE. Chem Rev 2007;107:2228.
- [85] Sievens-Figueroa L, Guymon CA. Polymer 2008;49:2260.
- [86] Hentze HP, Krämer E, Berton B, Förster S, Antonietti M. Macromolecules 1999;32:5803.
- [87] Karanikolos GN, Alexandridis P, Mallory R, Petrou A, Mountzaris TJ. Nanotechnology 2005;16:2372.
- [88] Tang S, Tang Y, Gao F, Liu Z, Meng X. Nanotechnology 2007;18:295607.
- [89] She G, Mu L, Shi W. Recent Pat Nanotechnol 2009;3:182.
- [90] Boonsalee S, Gudavarthy RV, Bohannan EW, Switzer JA. Chem Mater 2008;20:5737.
- [91] Zhang H, Zhou W, Du Y, Yang P, Wang C. Electrochim Commun 2010;12:882.
- [92] Kung HH, Ko EI. Chem Eng J 1996;64:203.
- [93] Kyriparidou-Leodidou T, Caseri W, Suter V. J Phys Chem 1994;98:8992.
- [94] Wang CC, Zhang Z, Ying JY. Nanostruct Mater 1997;9:583.
- [95] Gacoin T, Mailer L, Boilot JP. Chem Mater 1997;9:1502.
- [96] Sankaran V, Yue J, Cahen RE, Schrock RR, Silbey RJ. Chem Mater 1993;5:1133.

- [97] Yuan Y, Fendler J, Cabasso I. *Chem Mater* 1992;4:312.
- [98] Majetich SA, Canter AC. *J Phys Chem* 1993;97:8727.
- [99] Justus BL, Tonucci RJ, Berry AD. *Appl Phys Lett* 1992;61:3151.
- [100] Schmid H. *J Non-Cryst Solids* 1988;100:51.
- [101] Wang H, Lu YF. *J Appl Phys* 2008;103:013113.
- [102] Barth M, Hess P, Mollekopf G, Stafast H. *Thin Solid Films* 1994;241:61.
- [103] Chang X, Sun S, Han J. *Mater Lett* 2011;65:552.
- [104] Shen G, Bando Y, Golberg D. *J Nanosci Nanotechnol* 2009;9:572.
- [105] Torimoto T, Okazaki K, Kiyama T, Hirahara K, Tanaka N, Kuwabata S. *Appl Phys Lett* 2006;89:243117.
- [106] Okazaki K, Kiyama T, Hirahara K, Tanaka N, Kuwabata S, Torimoto T. *Chem Commun* 2008;691.
- [107] Suzuki T, Okazaki K, Kiyama T, Kuwabata S, Torimoto T. *Electrochemistry* 2009;77:638.
- [108] Tsuda T, Kurihara T, Hoshino Y, Kiyama T, Okazaki K, Torimoto T, et al. *Electrochemistry* 2009;77:693.
- [109] Suzuki T, Okazaki K, Suzuki S, Shibayama T, Kuwabata S, Torimoto T. *Chem Mater* 2010;22:5209.
- [110] Balasubramanian B, Kraemer KL, Reding NA, Skomski R, Ducharme S, Sellmyer DJ. *ACS Nano* 2010;4:1893.
- [111] Bullen HA, Garrett SJ. *Nano Lett* 2002;2:739.
- [112] Hulteen JC, Trichel DA, Smith MT, Duval ML, Jensen TR, Van Duyne RP. *J Phys Chem B* 1999;103:3854.
- [113] Tao L, Zhao XM, Gao JM, Hu W. *Nanotechnology* 2010;21:095301.
- [114] Hung AM, Micheal CM, Bozano LD, Osterbur LW, Wallraff GM, Cha JN. *Nat Nanotechnol* 2010;5:121.
- [115] Watanabe T, Soyama M, Kanazawa A, Takeuchi A, Koike M. *Thin Solid Films* 1999;345:161.
- [116] Li XG, Takahashi T, Watanabe K, Kikuchi Y, Koishi M. *Nano Lett* 2001;1:475.
- [117] Li XG, Chiba A, Sato M, Takahashi S. *Acta Mater* 2003;51:5593.
- [118] Xie L, Liu Y, Wang YT, Zheng J, Li XG. *Acta Mater* 2007;55:4585.
- [119] Xie L, Zheng J, Liu Y, Li Y, Li XG. *Chem Mater* 2008;20:282.
- [120] Chen J, Lu G, Zhu L, Flagan R. *J Nanopart Res* 2007;9:203.
- [121] Ohno S, Okuyama H, Honma K, Sakka Y. *Jpn Inst Met* 1996;60:318.
- [122] Ohno S, Uda M. *Jpn Inst Met* 1989;53:1062.
- [123] Ohno S, Uda M. *Jpn Inst Chem* 1984;11:924.
- [124] Li XG, Chiba A, Takahashi S, Sato M. *J Appl Phys* 1998;83:3871.
- [125] Li XG, Murai T, Chiba A, Takahashi S. *J Appl Phys* 1999;86:1867.
- [126] Li XG, Takahashi S. *J Magn Magn Mater* 2000;214:195.
- [127] Li X, Liu T, Sato M, Takahashi S. *Powder Technol* 2006;163:183.
- [128] Sakka Y, Okuyama H, Uchikoshi T, Ohno S. *J Alloy Compd* 2002;346:285.
- [129] Addamo M, Bellardita M, Carrizo D, Paola A, Milioto S, Palmisano L, et al. *Appl Catal B: Environ* 2008;84:742.
- [130] Irzh A, Genish I, Klein L, Solovyov LA, Gedanken A. *Langmuir* 2010;26:5976.
- [131] Feczkó T, Muskotál A, Gál L, Szépvölgyi J, Sebestyén A, Vonderviszt F. *J Nanopart Res* 2008;10:227.
- [132] Huang Y, Ai Z, Ho W, Chen M, Lee S. *J Phys Chem C* 2010;114:6342.
- [133] Hai NH, Lemoine R, Remboldt S, Strand M, Shield JE, Schmittner D, et al. *J Magn Magn Mater* 2005;293:75.
- [134] Song X, Zhang J, Yue M, Li E, Zeng H, Lu N, et al. *Adv Mater* 2006;18:1210.
- [135] Liu B, Hu Z, Che Y, Chen Y, Pan X. *Appl Phys Lett* 2007;90:044103.
- [136] Irissou E, Laplante F, Garbarino S, Chaker Mm Guay D. *J Phys Chem C* 2010;114:2192.
- [137] Zeng H, Li Z, Cai W, Cao B, Liu P, Yang S. *J Phys Chem B* 2007;111:14311.
- [138] Umezawa I, Nakayama Y, Sugimura A. *J Appl Phys* 2010;107:094318.
- [139] Mizukoshi Y, Takagi E, Okuno H, Oshima R, Maeda Y, Nagata Y. *Ultrason Sonochem* 2001;8:1.
- [140] Li K, Liu X, Wang H, Yan H. *Mater Lett* 2006;60:3038.
- [141] Wu Y, Wang L, Xiao M, Huang X. *J Non-Cryst Solids* 2008;354:2993.
- [142] Atobe M, Okamoto M, Fuchigami T, Park JE. *Ultrason Sonochem* 2010;17:26.
- [143] Kumar PSS, Manivel A, Anandan S, Zhou M, Grieser F, Ashokkumar M. *Colloids Surf A: Physicochem Eng Aspects* 2010;356:140.
- [144] Basnayake R, Li Z, Katar S, Zhou W, Rivera H, Smotkin ES, et al. *Langmuir* 2006;22:10446.
- [145] Nash MA, Lai JJ, Hoffman AS, Yager P, Stayton PS. *Nano Lett* 2010;10:85.
- [146] Li Z, Lai X, Wang H, Mao D, Xing C, Wang D. *J Phys Chem C* 2009;113:2792.
- [147] Ding JH, Gin DL. *Chem Mater* 2000;12:22.
- [148] Yamauchi Y, Momma T, Yokoshima T, Kuroda K, Osaka T. *J Mater Chem* 2005;15:1987.
- [149] Saez V, Gonzalez-Garcia J, Kulandainathan MA, Marken F. *Electrochim Commun* 2007;9:1127.
- [150] Day TM, Unwin PR, Macpherson JV. *Nano Lett* 2007;7:51.
- [151] Tang SC, Tang YF, Gao F, Liu ZG, Meng XK. *Nanotechnology* 2007;18:295607.
- [152] Dryfe RAW, Simm AO, Kralj B. *J Am Chem Soc* 2003;125:13014.
- [153] Chang MK, Chen CH, Chen BH. *Ind Eng Chem Res* 2008;47:3021.
- [154] Vu XH, Ly THA, Khuc OT, Dang DV, Nguyen DC. *Adv Nat Sci: Nanosci Nanotechnol* 2010;1:025014.
- [155] Outokeesh M, Hosseinpour M, Ahmadi SJ, Mousavand T, Sadjadi S, Soltanian W. *Ind Eng Chem Res* 2011;50:3540.
- [156] Fuentes S, Zárate RA, Chávez E, Muñoz P, Ayala M, Espinoza-González R, et al. *J Alloys Compds* 2010;505:568.
- [157] Rosemary MJ, Pradeep T. *J Colloid Interface Sci* 2003;268:81.
- [158] Mukherjee B, Ravishankar N. *Nanotechnology* 2007;18:025603.
- [159] Zawadzk M. *J Alloys Compds* 2008;454:347.
- [160] Hosokawa S, Jeon HJ, Iwamoto S, Inoue M. *J Am Ceram Soc* 2009;92:2847.
- [161] Yamauchi T, Tsukahara Y, Yamada K, Sakata T, Wada Y. *Chem Mater* 2011;23:75.
- [162] Palgrave RG, Parkin IP. *J Am Chem Soc* 2006;128:1587.
- [163] Zhang Z, Wei BQ, Ajayan PM. *Appl Phys Lett* 2001;79:4207.
- [164] Seipenbusch M, Binder A. *J Phys Chem C* 2009;113:20606.
- [165] Boyd DA, Greengard L, Brongersma M, El-Naggar MY, Goodwin DG. *Nano Lett* 2006;6:2592.

- [166] Elihn K, Landström L, Alm O, Boman M, Heszler P. *J Appl Phys* 2007;101:034311.
- [167] Domingo C, Resta V, Sanchez-Cortes S, Garcia-Ramos JV, Gonzalo J. *J Phys Chem C* 2007;111:8149.
- [168] Dumitracă F, Morjan I, Alexandrescu R, Ciupina V, Prodan G, Voicu I, et al. *Appl Surf Sci* 2005;247:25.
- [169] Maskrot H, Leconte Y, Herlin-Boime N, Reynaud C, Guelou E, Pinard L, et al. *Catal Today* 2006;116:6.
- [170] Jäger C, Huisken F, Mutschke H, Henning T, Poppitz W, Voicu I. *Carbon* 2007;45:2981.
- [171] Pignon B, Maskrot H, Ferreol VG, Leconte Y, Coste S, Gervais M, et al. *Eur J Inorg Chem* 2008;883.
- [172] Pan AL, Yao L, Qin Y, Yang Y, Kim DS, Yu R, et al. *Nano Lett* 2008;8:3413.
- [173] Sen S, Kanitkar P, Sharma A, Muthe KP, Rath A, Deshpande SK, et al. *Sens Actuat B – Chem* 2010;147:453.
- [174] Fan XY, Wu ZG, Yan PX, Geng BS, Li HJ, Li C, et al. *Mater Lett* 2008;62:1805.
- [175] Yan XM, Kwon S, Contreras AM, Bokor J, Somorjai GA. *Nano Lett* 2005;5:745.
- [176] Liu QF, Ren WC, Li F, Cong HT, Cheng HM. *J Phys Chem C* 2007;111:5006.
- [177] Ha B, Shin DH, Park J, Lee CJ. *J Phys Chem C* 2008;112:430.
- [178] Peng H, Fangli Y, Liuyang B, Jinlin L, Yunfa C. *J Phys Chem C* 2007;111:194.
- [179] Kamalakaran R, Terrones M, Seeger T, Kohler-Redlich P, Ruhle M, Kim YA, et al. *Appl Phys Lett* 2000;77:3385.
- [180] Breedon M, Rahmani MB, Keshmiri SH, Włodarski W, Kalantar-Zadeh K. *Mater Lett* 2010;64:291.
- [181] Vayssières L. *Adv Mater* 2003;15:464.
- [182] Al-Sharab JF, Sadangi RK, Shukla V, Tse SD, Kear BH. *Cryst Growth Des* 2009;9:4680.
- [183] Hu JQ, Li Q, Meng XM, Lee CS, Lee ST. *J Phys Chem B* 2002;106:9536.
- [184] Wang SF, Gu F, Lu MK, Zhou GJ, Zhang YY. *J Cryst Growth* 2006;289:621.
- [185] Xiu Z, Liu S, Yu J, Xu F, Yu W, Feng G. *J Alloy Compd* 2008;457:L9.
- [186] Guo S, Wu ZB, Wang HQ, Dong F. *Catal Commun* 2009;10:1766.
- [187] Huang LM, Wang HT, Wang ZB, Mitra A, Bozhilov KN, Yan YS. *Adv Mater* 2002;14:61.
- [188] Huang LM, Wang HT, Wang ZB, Mitra AP, Zhao D, Yan YS. *Chem Mater* 2002;14:876.
- [189] Kijima T, Ikeda T, Yada M, Machida M. *Langmuir* 2002;18:6453.
- [190] Murali S, Xu T, Marshall BD, Kayatin MJ, Pizarro K, Radhakrishnan VK, et al. *Langmuir* 2010;26:11176.
- [191] Kijima T, Yoshimura T, Uota M, Ikeda T, Fujikawa D, Mouri S, et al. *Angew Chem Int Ed* 2004;43:228.
- [192] Cheng FL, Wang H, Sun ZH, Ning MX, Cai ZQ, Zhang M. *Electrochim Commun* 2008;10:798.
- [193] Zhang XY, Dong DH, Li D, Williams T, Wang HT, Webley PA. *Electrochim Commun* 2009;11:190.
- [194] Baber S, Zhou M, Lin QL, Naalla M, Jia QX, Lu Y, et al. *Nanotechnology* 2010;21:165603.
- [195] Xia H, Feng JK, Wang HL, Lai MO, Lu L. *J Power Sources* 2010;195:4410.
- [196] Li Q, Walter EC, van der Veer WE, Murray BJ, Newberg JT, Bohannan EW, et al. *J Phys Chem B* 2005;109:3169.
- [197] Han CC, Bai MY, Lee JT. *Chem Mater* 2001;13:4260.
- [198] Tokuda N, Sasaki N, Watanabe H, Miki K, Yamasaki S, Hasunuma R, et al. *J Phys Chem B* 2005;109:12655.
- [199] Muench F, Kunz U, Neetzel C, Lauterbach S, Kleebe HJ, Ensinger W. *Langmuir* 2011;27:430.
- [200] Vasquez Y, Fenton EM, Chernow VF, Aizenberg J. *CrystEngComm* 2011;13:1077.
- [201] Zhao YN, Jin J, Yang XQ. *Mater Lett* 2007;61:384.
- [202] Sparta M, Børve KJ, Jensen VR. *J Phys Chem B* 2006;110:11711.
- [203] Tang YH, Pei LZ, Lin LW, Li XX. *J Appl Phys* 2009;105:044301.
- [204] Shim HW, Lee DK, Cho IS, Hong KS, Kim DW. *Nanotechnology* 2010;21:255706.
- [205] Tang K, Qian Y, Zeng J, Yang X. *Adv Mater* 2003;15:448.
- [206] Wang WZ, Poudel B, Wang DZ, Ren ZF. *Adv Mater* 2005;17:2110.
- [207] Kar S, Chaudhuri S. *Mater Lett* 2005;59:289.
- [208] Xu D, Liu ZP, Liang JB, Qian YT. *J Phys Chem B* 2005;109:14344.
- [209] Sun CW, Li H, Zhang HR, Wang ZX, Chen LQ. *Nanotechnology* 2005;16:1454.
- [210] Nath M, Parkinson BA. *Adv Mater* 2006;18:1865.
- [211] Zhou Z, Deng Y. *J Phys Chem C* 2009;113:19853.
- [212] Chaudhuri MG, Dey R, Mitra MK, Das GC, Mukherjee S. *Sci Technol Adv Mater* 2008;9:015002.
- [213] Bitenc M, Drazic G, Orel ZC. *Cryst Growth Des* 2010;10:830.
- [214] Schmitt AL, Zhu L, Schmeisser D, Himpsel FJ, Jin S. *J Phys Chem B* 2006;110:18142.
- [215] Guo JZ, Zuo Y, Li ZJ, Gao WD, Zhang JL. *Physica E* 2007;39:262.
- [216] Kamins TI, Li X, Williams RS. *Nano Lett* 2004;4:503.
- [217] Shimizu T, Zhang Z, Shingubara S, Senz S, Gosele U. *Nano Lett* 2009;9:1523.
- [218] Qi PF, Wong WS, Zhao HZ, Wang DW. *Appl Phys Lett* 2008;93:163101.
- [219] Bondi SN, Lackey WJ, Johnson RW, Wang X, Wang ZL. *Carbon* 2006;44:1393.
- [220] Duan XF, Lieber CM. *Adv Mater* 2000;12:298.
- [221] Liu Z, Styers-Barnett DJ, Puretzky AA, Rouleau CM, Yuan D, Ivanov IN, et al. *Appl Phys A* 2008;93:987.
- [222] Bachmatuk A, Borowiak-Palen E, Rummeli MH, Kramberger C, Hubers HW, Gemming T, et al. *Nanotechnology* 2007;18:275610.
- [223] Longtin R, Fauteux C, Goduguchinta R, Pegna J. *Thin Solid Films* 2007;515:2958.
- [224] Morjan I, et al. *Infrared Phys Technol* 2008;51:186.
- [225] Alexandrescu R, et al. *Infrared Phys Technol* 2010;53:94.
- [226] Alexandrescu R, et al. *Thin Solid Films* 2007;515:8438.
- [227] Dai ZR, Pan ZW, Wang ZL. *J Am Chem Soc* 2002;124:8673.
- [228] Dai ZR, Pan ZW, Wang ZL. *J Phys Chem B* 2002;106:902.
- [229] He Y, Ye T, Ribbe AE, Mao C. *J Am Chem Soc* 2011;133:1742.
- [230] Liu JB, Dong H, Li YM, Zhan P, Zhu MW, Wang ZL. *Jpn J Appl Phys* 2006;45:L582.
- [231] Ulmeanu M, Filipescu M, Medianu RV. *Phys Status Solidi C* 2008;5:3584.
- [232] Duan GT, Lv FJ, Cai WP, Luo YY, Li Y, Liu GQ. *Langmuir* 2010;26:6295.
- [233] Lee SW, Lee KS, Ahn J, Lee JJ, Kim MG, Shin YB. *ACS Nano* 2011;5:897.
- [234] Vizireanu S, Nistor L, Haupt M, Katzenmaier V, Oehr C, Dinescu G. *Plasma Process Polym* 2008;5:263.

- [235] Pingali KC, Deng SG, Rockstraw DA. *Curr Nanosci* 2007;3:215.
- [236] Dato A, Radmilovic V, Lee ZH, Phillips J, Frenklach M. *Nano Lett* 2008;8:2012.
- [237] Simakin AV, Voronov VV, Shafeev GA, Brayner R, Bozon-Verduraz F. *Chem Phys Lett* 2001;348:182.
- [238] Qin WJ, Yang XB, Lu YW, Sun J, Kulinich SA, Du XW. *Chem Mater* 2008;20:3892.
- [239] Yang L, May PW, Yin L, Scott TB. *Nanotechnology* 2007;18:215602.
- [240] Bhattacharyya S, Gedanken A. *Microporous Mesoporous Mater* 2008;110:553.
- [241] Chen S, Carroll DL. *Nano Lett* 2002;2:1003.
- [242] Hao EC, Kelly KL, Hupp JT, Schatz GC. *J Am Chem Soc* 2002;124:15182.
- [243] Chen S, Fan Z, Carroll DL. *J Phys Chem B* 2002;106:10777.
- [244] Kawasaki H, Uota M, Yoshimura T, Fujikawa D, Sakai G, Annaka M, et al. *Langmuir* 2005;21:11468.
- [245] Sakai G et al. *Adv Mater* 2007;19:237.
- [246] Kijima T et al. *Adv Funct Mater* 2009;19:545.
- [247] Wang L, Chen X, Zhan J, Sui ZM, Zhao JK, Sun ZW. *Chem Lett* 2004;33:720.
- [248] Wang L, Chen X, Zhan J, Chai Y, Yang C, Xu L, et al. *J Phys Chem B* 2005;109:3189.
- [249] Eliaz N, Sridhar TM. *Cryst Growth Des* 2008;8:3965.
- [250] Liu DW et al. *Adv Funct Mater* 2009;19:1015.
- [251] He W, Gao P, Chu L, Yin L, Xie Y. *Nanotechnology* 2006;17:3512.
- [252] Chu D, Masuda Y, Ohji T, Kato K. *Langmuir* 2010;26:14814.
- [253] Ahern D, Charles DE, Brennan-Fournet ME, Kelly JM, Gun'ko YK. *Langmuir* 2009;25:10165.
- [254] Jiang CL, Zhang WQ, Liu YK, Qian YT. *Cryst Growth Des* 2006;6:2603.
- [255] Kamada K, Hyodo T, Shimizu Y. *J Phys Chem C* 2010;114:3707.
- [256] Cheng F, Zhao J, Song W, Li C, Ma H, Chen J, et al. *Inorg Chem* 2006;45:2038.
- [257] Takami S, Hayakawa R, Wakayama Y, Chikyow T. *Nanotechnology* 2010;21:134009.
- [258] Du J, Han B, Liu Z, Liu Y, Kang D. *Cryst Growth Des* 2007;7:900.
- [259] Li F, Kong T, Bi WT, Li DC, Li Z, Huang XT. *Appl Surf Sci* 2009;255:6285.
- [260] Cheng JP, Ma R, Shi D, Liu F, Zhang XB. *Ultrasound Sonochem* 2011. doi:[10.1016/j.ultsonch.2010.12.00](https://doi.org/10.1016/j.ultsonch.2010.12.00).
- [261] Wang G, Ji Y, Zhang L, Zhu Y, Gouma PI, Dudley M. *Chem Mater* 2007;19:979.
- [262] Azimirad R, Khosravi P, Moshfegh AZ. *Surf Interface Anal* 2011. doi:[10.1002/sia.373](https://doi.org/10.1002/sia.373).
- [263] Barreca D, Ferrucci AP, Gasparotto A, Maccato C, Maragno C, Tondello E. *Chem Vapor Depos* 2007;13:618.
- [264] Gao R, Yin L, Wang C, Qi Y, Lun N, Zhang L, et al. *J Phys Chem C* 2009;113:15160.
- [265] Guan YF, Pedraza AJ. *Nanotechnology* 2008;19:045609.
- [266] Combemale L, Leconte Y, Portier X, Herlin-Boime N, Reynaud C. *J Alloy Compd* 2009;483:468.
- [267] Fang XS, Ye CH, Zhang LD, Zhang JX, Zhao JW, Yan P. *Small* 2005;4:422.
- [268] Zhang YJ, Zhang Y, Wang ZH, Li D, Cui TY, Liu W, et al. *Eur J Inorg Chem* 2008;17:2733.
- [269] Luo YS, Li SQ, Ren QF, Liu JP, Xing LL, Wang Y, et al. *Cryst Growth Des* 2007;7:87.
- [270] Luo YS, Zhang WD, Dai XJ, Yang Y, Fu SY. *J Phys Chem C* 2009;113:4856.
- [271] Zhang K, Tenailleau C, Alphonse P, Chane-Ching JY. *Appl Phys A* 2010;100:1049.
- [272] Abdulgafour HI, Hassan Z, Al-Hardan N, Yam FK. *Physica B* 2010;405:2570.
- [273] Wang J, Huang HC, Kesapragada SV, Gall D. *Nano Lett* 2005;5:2505.
- [274] Kuo CW, Shiu JY, Chen P. *Chem Mater* 2003;15:2917.
- [275] Xu Q, Tonks I, Fuerstman MJ, Christopher Love J, Whitesides GM. *Nano Lett* 2004;4:2509.
- [276] Zhang G, Wang D, Möhwald H. *Nano Lett* 2007;7:3410.
- [277] Zhang GY et al. *Proc Natl Acad Sci USA* 2005;102:16141.
- [278] Yang SL, Gao RS, Niu PL, Zou ZY, Yu RH. *Nanoscale Res Lett* 2011;6:12.
- [279] Lei WW, Liu D, Zhang J, Zhu PW, Cui QL, Zou GT. *Cryst Growth Des* 2009;9:1489.
- [280] Suh WH, Suslick KS. *J Am Chem Soc* 2005;127:12007.
- [281] Zhang J et al. *Cryst Growth Des* 2007;7:2764.
- [282] Tavangar A, Tan B, Venkatakrishnan KJ. *Micromech Microeng* 2010;20:055002.
- [283] Zhu L, Liu X, Meng J, Cao X. *Cryst Growth Des* 2007;7:2505.
- [284] Mao CJ, Wang DC, Pan HC, Zhu JJ. *Ultrasound Sonochem* 2011;18:473.
- [285] Li Y, Xu DS, Zhang QM, Chen DP, Huang FZ, Xu YJ, et al. *Chem Mater* 1999;11:3433.
- [286] Edmondson MJ, Zhou WZ, Sieber SA, Jones IP, Gameson I, Anderson PA, et al. *Adv Mater* 2001;13:1608.
- [287] Yu SH, Colfen H, Tauer K, Antonietti M. *Nat Mater* 2005;4:51.
- [288] Yu SH, Antonietti M, Colfen H, Hartmann J. *Nano Lett* 2003;3:379.
- [289] Chen D, Shen GZ, Tang KB, Liang ZH, Zheng HG. *J Phys Chem B* 2004;108:11280.
- [290] Zhong HZ, Li YC, Zhou Y, Yang CH, Li YF. *Nanotechnology* 2006;17:772.
- [291] Yamauchi Y, Sugiyama A, Morimoto R, Takai A, Kuroda K. *Angew Chem Int Ed* 2008;47:5371.
- [292] Yamauchi Y, Takai A, Komatsu M, Sawada M, Ohsuna T, Kuroda K. *Chem Mater* 2008;20:1004.
- [293] Yamauchi Y, Momma T, Fuziwara M, Nair SS, Ohsuna T, Terasaki O, et al. *Chem Mater* 2005;17:6342.
- [294] Yamauchi Y, Kuroda K. *Chem Asian J* 2008;3:664.
- [295] Tiwari JN, Pan FM, Lin KL. *New J Chem* 2009;33:1482.
- [296] Tiwari JN, Tiwari RN, Lin KL. *ACS Appl Mater Interfaces* 2010;2:2231.
- [297] Zhang HM, Zhou WQ, Du YK, Yang P, Wang CY. *Electrochim Commun* 2010;12:882.
- [298] Xu P, Mack NH, Jeon SH, Doorn SK, Han X, Wang HL. *Langmuir* 2010;26:8882.
- [299] Bechelany M, Brodard P, Elias J, Brioude A, Michler J, Philippe L. *Langmuir* 2010;26:14364.
- [300] Drozdowicz-Tomska K, Xie F, Goldys EM. *J Phys Chem C* 2010;114:1562.
- [301] Yan C, Xue D. *Cryst Growth Des* 2008;8:1849.
- [302] Gutes A, Carraro C, Maboudian R. *J Am Chem Soc* 2010;132:1476.
- [303] Wu HC, Tsai HY, Chiu HT, Lee CY. *ACS Appl Mater Interfaces* 2010;2:3285.
- [304] Zhou XF, Hu ZL, Fan YQ, Chen S, Ding WP, Xu NP. *J Phys Chem C* 2008;112:11722.

- [305] Cheng CW et al. *ACS Nano* 2009;3:3069.
- [306] Wang CX, Yin LW, Zhang LY, Qi YX, Lun N, Liu NN. *Langmuir* 2010;26:12841.
- [307] Zhao ZG, Miyauchi M. *J Phys Chem C* 2009;113:6539.
- [308] Cheng H, Chiu W, Lee C, Tsai S, Hsieh W. *J Phys Chem C* 2008;112:16359.
- [309] Thongtem T, Phuruangrat A, Thongtem S. *Curr Appl Phys* 2009;9:195.
- [310] Huang JR, Yu K, Gu CP, Zhai MH, Wu YJ, Yang M, et al. *Sens Actuat B* 2010;147:467.
- [311] Chuang ATH, Robertson J, Boskovic BO, Koziol KKJ. *Appl Phys Lett* 2007;90:123107.
- [312] Liu X, Baronian KHR, Downard AJ. *Anal Chem* 2008;80:8835.
- [313] Chan KT, Kan JJ, Doran C, Lu OY, Smith DJ, Fullerton EE. *Nano Lett* 2010;10:5070.
- [314] Tiwari JN, Tiwari RN, Singh G, Lin KL. *Plasmonics* 2011;6:67.
- [315] Heszl P, Landström L, Granqvist CG. *Appl Surf Sci* 2007;253:8292.
- [316] Goto T, Kimura T. *Thin Solid Films* 2006;515:46.
- [317] Maxwell JL, Boman M, Springer RW, Narayan J, Gnanavelu S. *J Am Chem Soc* 2006;128:4405.
- [318] Le Normand F et al. *Appl Surf Sci* 2007;254:1058.
- [319] Bystrzejewski M et al. *J Solid State Chem* 2008;181:2796.
- [320] Manthiram A, Murugan AV, Sarkar A, Muraliganth T. *Energy Environ Sci* 2008;1:621.
- [321] Yu EH, Krewer U, Scott K. *Energies* 2010;3:1499.
- [322] Vigier F, Rousseau S, Coutanceau C, Leger JM, Lamy C. *Top Catal* 2006;40:111.
- [323] Nguyen NT, Chan SH. *J Micromech Microeng* 2006;16:R1.
- [324] Kua J, Goddard WA. *J Am Chem Soc* 1999;121:10928.
- [325] Raoof JB, Ojani R, Rashid-Nadimi S. *J Electroanal Chem* 2010;641:71.
- [326] Jin Y, Shen Y, Dong S. *J Phys Chem B* 2004;108:8142.
- [327] Kim P, Joo JB, Kim W, Kim J, Song IK, Yi J. *J Power Sources* 2006;160:987.
- [328] Wang S, Kristian N, Jiang S, Wang X. *Nanotechnology* 2009;20:025605.
- [329] Tiwari JN, Tiwari RN, Lin KL. *Nano Res* 2011;4:541.
- [330] Chen G, Dingguo X, Nie Z, Wang Z, Wang L, Zhang L, et al. *Chem Mater* 2007;19:1840.
- [331] Zhong Y, Xu CL, Kong LB, Li HL. *Appl Surf Sci* 2008;255:3388.
- [332] Zhao GY, Xu CL, Guo DJ, Li H, Li HL. *J Power Sources* 2006;162:492.
- [333] Qi J et al. *Chin J Catal* 2006;27:708.
- [334] Huang T, Meng F, Qi LM. *Langmuir* 2010;26:7582.
- [335] Lin ZH, Lin MH, Chang HT. *Chem Eur J* 2009;15:4656.
- [336] Ksar F et al. *Chem Mater* 2009;21:1612.
- [337] Liu LF, Pippel E, Scholz R, Gosele U. *Nano Lett* 2009;9:4352.
- [338] Lu Y, Chen W. *J Phys Chem C* 2010;114:21190.
- [339] Li W, Ma H, Zhang J, Liu X, Feng X. *J Phys Chem C* 2009;113:1738.
- [340] Jia FL, Wong KW, Du RX. *Electrochim Commun* 2009;11:519.
- [341] Choi WC, Woo SI. *J Power Sources* 2003;124:420.
- [342] Sharma S, Gunguly A, Papakonstantinou P, Miao X, Li M, Hutchison JL, et al. *J Phys Chem C* 2010;114:19459.
- [343] Bong S et al. *Electrochim Commun* 2010;12:129.
- [344] Tong XL, Zhao GH, Liu MC, Cao TC, Liu L, Li PQ. *J Phys Chem C* 2009;113:13787.
- [345] Tiwari JN, Tiwari RN, Chang YM, Lin KL. *ChemSusChem* 2010;3:460.
- [346] Tiwari JN, Pan FM, Chen TM, Tiwari RN, Lin KL. *J Power Sources* 2010;195:729.
- [347] Miller JR, Simon P. *Science* 2008;321:651.
- [348] Zhang LL, Zhao XS. *Chem Soc Rev* 2009;38:2520.
- [349] Hall PJ et al. *Energy Environ Sci* 2010;3:1238.
- [350] Simon P, Gogotsi Y. *Nat Mater* 2008;7:845.
- [351] Frackowiak E, Beguin F. *Carbon* 2001;39:937.
- [352] Diederich L et al. *Appl Phys Lett* 1999;75:2662.
- [353] Emmenegger C, Mauron P, Sudan P, Wenger P, Hermann V, Gallay R, et al. *J Power Sources* 2003;124:321.
- [354] Elzanowska H, Miaselski E, Birss V. *Electrochim Acta* 2008;53:2706.
- [355] Mu J et al. *J Colloid Interface Sci* 2011;356:706.
- [356] Gujari TP, Shinde VR, Lokhande CD, Kim WY, Jung KD, Joo OS. *Electrochim Commun* 2007;9:504.
- [357] Devadas A, Baranton S, Napporn TW, Coutanceau C. *J Power Sources* 2011;196:4044.
- [358] Sugimoto W, Kizaki T, Yokoshima K, Murakami Y, Takasu Y. *Electrochim Acta* 2004;49:313.
- [359] Zhang Y et al. *Int J Hydrog Energy* 2009;34:4889.
- [360] Nam KW, Yoon WS, Kim KB. *Electrochim Acta* 2002;47:3201.
- [361] Ni WB, Wang DC, Huang ZJ, Zhao JW, Cui GE. *Mater Chem Phys* 2010;124:1151.
- [362] Chen J, Huang KL, Liu SQ, Hu X. *J Power Sources* 2009;186:565.
- [363] Penny MW, Brown MR, Maffeis TGG, Rees P, Wilks SP, Ferkel HS. *Appl Phys Lett* 2007;91:163108.
- [364] Grupioni AAF, Arashiro E, Lassali TAF. *Electrochim Acta* 2002;48:407.
- [365] Rajeswari J, Kishore PS, Viswanathan B, Varadarajan TK. *Electrochim Commun* 2009;11:572.
- [366] Cui L, Li J, Zhang XG. *J Appl Electrochem* 2009;39:1871.
- [367] Gupta V, Miura N. *Mater Lett* 2006;60:1466.
- [368] Zhao X et al. *Nanotechnology* 2009;20:065605.
- [369] Li JR, Tang ZL, Zhang ZT. *Electrochim Commun* 2005;7:894.
- [370] Yu P, Zhang X, Chen Y, Ma YW, Qi ZP. *Mater Chem Phys* 2009;118:303.
- [371] Chou SL, Cheng FY, Chen J. *J Power Sources* 2006;162:727.
- [372] Hu YS, Guo YG, Sigle W, Hore S, Balaya P, Maier J. *Nat Mater* 2006;5:713.
- [373] Long JW, Swider KE, Merzbacher CI, Rolison DR. *Langmuir* 1999;15:780.
- [374] Subramanian V, Hall SC, Smith PH, Rambabu B. *Solid State Ion* 2004;175:511.

- [375] Prasad KR, Koga K, Miura N. *Chem Mater* 2004;16:1845.
- [376] Malak-Polaczyk A, Vix-Guterl C, Frackowiak E. *Energy Fuels* 2010;24:3346.
- [377] Zhang K, Zhang LL, Zhao XS, Wu J. *Chem Mater* 2010;22:1392.
- [378] Sassin MB, Mansour AN, Pettigrew KA, Rolison DR, Long JW. *ACS Nano* 2010;4:4505.
- [379] Xu JJ, Wang K, Zu SZ, Han BH, Wei ZX. *ACS Nano* 2010;4:5019.
- [380] Kim TY et al. *ACS Nano* 2011;5:436.
- [381] Wang H, Sanchez Casalongue H, Liang Y, Dai H. *J Am Chem Soc* 2010;132:7472.
- [382] Song MS et al. *J Phys Chem C* 2010;114:22134.
- [383] Wu Q, Xu YX, Yao ZY, Liu AR, Shi GQ. *ACS Nano* 2010;4:1963.
- [384] Kim B, Chung H, Kim W. *J Phys Chem C* 2010;114:15223.
- [385] Palacni MR. *Chem Soc Rev* 2009;38:2565.
- [386] Chen J, Cheng FY. *Acc Chem Res* 2009;42:713.
- [387] Balaya P. *Energy Environ Sci* 2008;1:645.
- [388] Nam KT, Kim DW, Yoo PJ, Chiang CY, Meethong N, Hammond PT, et al. *Science* 2006;312:885.
- [389] Shukla AK, Kumar TP. *Curr Sci* 2008;94:314.
- [390] Chen G, Song S, Richardson T. *J Electrochem Solid State Lett* 2006;9:A295.
- [391] Srinivasan V, Newman J. *J Electrochem Soc* 2004;151:A1517.
- [392] Delacourt C, Poizot P, Levasseur S, Masquelier C. *J Electrochem Solid State Lett* 2006;9:A352.
- [393] Kim DH, Ahn YS, Kim J. *Electrochim Commun* 2005;7:1340.
- [394] Cui LF, Ruffo R, Chan CK, Peng HL, Cui Y. *Nano Lett* 2009;9:491.
- [395] Cui LF, Yang Y, Hsu CM, Cui Y. *Nano Lett* 2009;9:3370.
- [396] Park MH et al. *Nano Lett* 2009;9:3844.
- [397] Seo JW, Jang JT, Park SW, Kim CJ, Park BW, Cheon JW. *Adv Mater* 2008;20:4269.
- [398] Chen JS et al. *ACS Appl Mater Interfaces* 2010;2:3628.
- [399] Zhou LA, Yang LC, Yuan P, Zou J, Wu YP, Yu CZ. *J Phys Chem C* 2010;114:21868.
- [400] Hassan MF, Guo ZP, Chen Z, Liu HK. *J Power Sources* 2010;195:2372.
- [401] Zhan FM, Geng BY, Guo YJ. *Chem Eur J* 2009;15:6169.
- [402] Wang GX, Shen XP, Yao J, Park J. *Carbon* 2009;47:2049.
- [403] Wang JQ et al. *Electrochim Acta* 2010;55:4805.
- [404] Zhou S, Liu XH, Wang DW. *Nano Lett* 2010;10:860.
- [405] Hassoun J, Lee KS, Sun YK, Scrosati B. *J Am Chem Soc* 2011;133:3139.
- [406] Needham SA, Wang GX, Liu HK. *J Power Sources* 2006;159:254.
- [407] Fang HT et al. *Nanotechnology* 2009;20:225701.
- [408] Bazin L et al. *J Power Sources* 2009;188:578.
- [409] Taberna L, Mitra S, Poizot P, Simon P, Tarascon JM. *Nat Mater* 2006;5:567.
- [410] Reddy ALM, Shajumon MM, Gowda SR, Ajayan PM. *Nano Lett* 2009;9:1002.
- [411] Xiang JY, Tu JP, Yuan YF, Wang XL, Huang XH, Zeng ZY. *Electrochim Acta* 2009;54:1160.
- [412] Ning J et al. *Langmuir* 2009;25:1818.
- [413] Kim SW, Seo DH, Gwon H, Kim J, Kang K. *Adv Mater* 2010;22:5260.